The Daresbury Photon Microprobe

by

Frans van Langevelde

A thesis submitted for the degree of

Doctor of Philosophy

of the

University of Warwick

July 1991

Knowledge
is
fundamentally
dangerous

Maurice
Blanchot

Abstract

In many branches of science it is important to be able to measure elemental distributions on the micrometre level. Therefore a Synchrotron X-ray Fluorescence microbeam has been built at the SRS, Daresbury. The synchrotron microprobe technique for trace element analysis (micro-SXRF) is the subject of this study.

This thesis begins with an overview of different microprobe techniques for trace element analysis. Features and capabilities are presented which are used to compare these methods and to make clear the relation between micro-SXRF and the other microprobes. This is followed by a review of relevant literature, which is related to X-ray focussing in general and the application of synchrotron radiation for trace element analysis, as well as the design and development of synchrotron microbeams.

Tools are presented to calculate and judge the quality of optical shapes and configurations for the design of X-ray optics. Aberration theory is used to derive the necessary focus conditions as well as the main aberration terms and ray-tracing to design the optical components of the microprobe. The conclusion of the calculations is that in the case of the single crystal option the ellipsoid has the best X-ray optical features.

Criteria have been formulated in order to design a microprobe for trace element analysis. Finally an ellipsoidally shaped concave bent Si(111) crystal has been constructed as the basic element of the microprobe. The results are presented in terms of beam profiles and flux densities to demonstrate the focussing action of the bent crystal and in terms of detection limits and sensitivities to demonstrate the analytical features, which are consistent with calculations. A final resolution of 10x15 μm^2 is obtained and a flux density of about 10^4 ph/(s.mA.μm^2) is measured for 15 keV quasi-monochromatic radiation, which is able to detect femtogram levels in favourable cases.

The last part of this study is devoted to the design of X-ray optics for the ESRF (Grenoble). Comparisons are made for what can be expected if the ESRF source parameters are used rather than the SRS source parameters for the same type of optics. A planar-ellipsoid combination seems to be a good option for focussing as well as managing the high intensity of the incident white beam.

Acknowledgements

Firstly, I like to thank Prof. Keith Bowen and Dr. Ronald Vis. Without their co-oporation this work could not have been realised. By their agreement I was able to do the work necessary for the completion of this thesis. I would also like to thank Dr. Charles Thomas for being a very critical supervisor, who showed me the rules and demands for finishing an English Ph. D. thesis, and actively joined the experimental runs.

Very special thanks to Ronald with whom I spent many many hours and not only working hours over the last 10 years. We went through many stages of development of the use of synchrotron X-ray beams and proton beams too for Trace Element Analysis. Many thanks for all the discussions, reading and correction of the manuscript, and the ups and downs during, before and after the experiments.

I am grateful to my former colleague Dr. Willem Lenglet, who introduced me at Daresbury in 1985 and by whom I became acquainted with the different aspects of Synchrotron radiation at the SRS for Trace Element Analysis. We spent lots of hours together travelling to Daresbury, working at the laboratory and resting at the Ring O' Bells.

During the years many people assisted the experiments. In the first instance, when the Eindhoven University of Technology was involved, Ir. Maarten Prins and Ir. Wim Dries actively participated. Maarten initiated the use of curved crystals and Wim developed the execution program for Trace Element Analysis which is still in use. At a later stage students and collegues from the Vrije Universiteit became involved, in particular Gerald Tros, who helped setting up the experiment from scratch many times, Ronald Overwater, Cor Stoof and Knud Wiederspahn. Because of a lack of manpower in the summer of 1986 my colleague and close friend Kees Hagen supported the experiments. Also Dr. Graham Fisher showed active interest in the work by attending some of the experiments. They are all acknowledged.

I am also very grateful to the Philips Research Laboratories for their interest and support and for manufacturing of the different types of silicon curved crystals. I am particular grateful to Dr. M.P.A. Viegers, Mr. A. Huizing and Dr. D.K.G. de Boer. Without their efforts to produce the doubly bent crystals the concept of a microprobe described in this thesis could not have been realised.

I am grateful to Ir. T.J.J.M. Jennekens for the computer code SIMUL, which I used as a basis for further development to simulate different types of curved crystals.

I would like to thank the Daresbury staff, who are responsible for the high degree of efficiency of operation of the Synchrotron source. During the last four years only two periods of a week were lost. I am grateful to Dr. Graham Clark who was the station master of the topography stations 7.6 and 9.4. Special thanks to the technician Mr. Alf Neild who often gave a welcome break to show the comic side of our work and life in general.

I would also like to thank the Science and Engineering Research Council (SERC) and the Netherlands Organisation of Advanced Science (NWO), because the research work presented in this thesis was supported by these organisations in connection with the agreement between SERC and NWO concerning the SRS.

I am grateful to the mechanical workshops of the Vrije Universiteit and the University of Warwick for their technical assistance.

Very special thanks to collegue Knud Wiederspahn who prepared most of the targets I used and who introduced me to the software package and texteditor Framemaker. He transferred to me his enthusiasm for the use of the package. He also did a lot of the layout work and the typesetting of the Appendices.

Also thanks to Andries Pomper who over the years produced a vast number of graphs for publications as well as for this thesis. I am also grateful to the Daresbury photographic service for the photographs of the experimental setup in operation.

I wish to express gratitude to Dr. Tardi Tjahjadi who was so kind to provide me accomodation during my stays at Coventry.

Finally, I would like to thank the Faculty of Physics and Astronomy of the Vrije Universiteit for their hospitality and the Experimental Nuclear Physics Group for their continuing interest, and putting at my disposal room and the use of facilities to be able to do the necessary work in Amsterdam.

Contents

Chapter 1

Introduction

1.1 Beam techniques for microanalysis

The development of materials and devices for high technology as well as the detailed study of certain types of biological, geological, (bio)- chemical, archaeological or extraterrestrial samples create extensive requirements for the analytical characterization of materials. At the present state of development various established analytical techniques are available to gain information about bulk composition and elemental concentration, the distribution and concentration of major, minor and trace elements, impurities and dopants through micro analysis, the identification of surface contaminants and adsorbed species by surface analysis, and geometric and electronic structure [Gra87]. Table 1.1 shows different types of analytical characterization of solid materials, and the methods which are able to provide this type of information. During the past decades, there has been a proliferation of new physical techniques for elemental analysis with particular emphasis on the analysis of extremely small specimen volumes with high sensitivity.

Analytical Characterization	Type of Analysis	Type of Analytical Method*
Bulk Composition	Bulk	AAS, OES, (S)XRF, MS, Activation Analysis, Chemical Methods
Distribution of Elements and Phases	Surface, Interface and in-situ Micro	EPMA, SEM, TEM (EDX, TEELS), SIMS, LAMMA, XPS, AES, RBS, ISS, PIXE, SXRF
Geometric Structure	Geom. Structure	XRD, TEM, THEED, IR, RAMAN, NMR, EXAFS
Electronic Structure	Electr. Structure	UPS, XPS, X-ray Valence Band Spectroscopy

* The acronyms are defined in Appendix I.

Table 1.1 The analytical characterization of solid materials

The need for techniques that can determine trace element concentrations in a variety of specimens is growing rapidly. In biology, the so called essential elements such as copper and zinc, in low concentrations, play a crucial role in living material. The awareness that

toxic elements, even in very low concentrations, can detrimentally influence the biosphere highlights the importance of conclusive analytical procedures. In geology, the abundance of (volatile) trace elements in rocks and sediments often records their history of formation in terms of temperatures and pressures during formation or in terms of cooling rates. In material science and especially in the semiconductor industry, there is a growing need for high purity materials. Monitoring of the production process and assessment of the final product demands sensitive analysis with precise quantitative results.

In this thesis the design, the X-ray optical features and analytical capabilities of a Synchrotron X-ray microprobe for elemental analysis are presented. It is therefore illustrative to fit this technique into the existing picture of similar techniques, e.g. those described by Grasserbauer [Gra87], Wittry [Wit80], Russ [Rus85] and Shaffner [Sha86]. These physical techniques, also called beam techniques, involve bombardment of the specimen with particles or electromagnetic radiation in order a) to produce a particular excitation of the elements in the specimen, which can be detected by the emission of particles or electromagnetic radiation or b) to obtain information about the specimen by scattering or absorption of the incident particles or radiation. The specimen can be bombarded by electrons, ions (protons), X-rays or light, and various signals consisting of electromagnetic waves, charged particles or sound waves can be detected. In order to obtain information on the elemental composition of the specimen, it is in most cases necessary to use some kind of spectrometer e.g. an X-ray spectrometer (X.S.), an optical spectrometer (O.S.), an electron spectrometer (E.S.), an ion spectrometer (I.S.) or a mass spectrometer (M.S.). All techniques of microanalysis must utilize some method to localize the analysis. Wittry [Wit80] has categorized the various methods that have been used for spatial localization in the various microanalytical techniques.

Area localization

- By focussing the exciting beam (microprobe method)
- By focussing the emitted or transmitted beam (selected area method)

Depth localization

- By using reactions with small excitation depth

- By using signals with small escape depth
- By using very thin specimens

It is in principle possible to use either the microprobe method or the selected area method for spatial localization. Sometimes it is not possible to use the selected area method, e.g. EPMA, PIXE and Scanning Absorption X-ray Microscopy. For the comparison of the SXRF microprobe with other microprobes only techniques based on the microprobe method will be discussed. Some typical cases of micro analytical techniques based on bombardment of the specimen by focussed electrons, ions, X-rays or optical photons are shown in the figures 1.1-1.4. In order to obtain elemental composition of the specimen with micrometre resolution, different microbeam techniques are used nowadays, such as: EPMA, PIXE, LAMMA, SIMS and SXRF. To compare these techniques the criteria described by Russ [Rus85] are adopted:

- What is measured ?
- Where is it measured, both in depth or lateral extent ?
- Whether the method is or is not destructive ?
- What are typical detection limits and how does this vary with element and matrix ?
- What special attributes are offered, such as turn around time, sample preparation, depth profiling, chemical state etc. ?
- The method capable of quantitative results based on calibration and/or theoretical models ?

1.1.1 EPMA - Electron Probe Micro Analysis

The electron probe represents the first and most widely used microprobe technique in research and industrial laboratories. On a routine basis elemental compositions are determined by measuring X-ray energies or wavelengths by energy or wavelength dispersive spectrometers. Because electrons are used for excitation, it is possible to focus the beam to a very area (of the order of nm^2) by electromagnetic focussing. Electrons lose energy very rapidly in solids, so the depth of excitation is much less than with e.g. XRF. The detection volume is in the order of cubic microns, owing to multiple scattering,

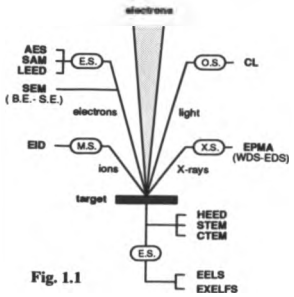

Fig. 1.1

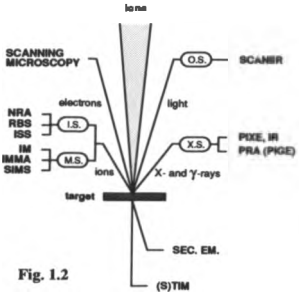

Fig. 1.2

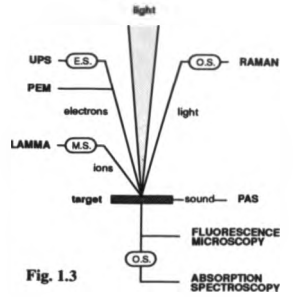

Fig. 1.3

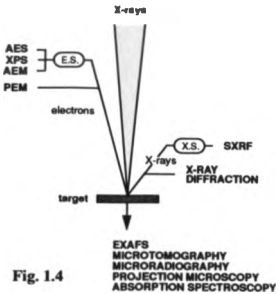

Fig. 1.4

Fig. 1.1 - 1.4 Microanalytical techniques based on focussed electrons, ions, optical photons and X-rays respectively.

which limits the lateral resolution. The use of an electron beam also requires a moderately good vacuum system. Because of the impracticality of obtaining large suites of standard samples that are homogeneous on a fine scale, there is much emphasis in EPMA on fundamental theory for quantification. Major efforts have been made to quantify elements such as B, C, N and O by improved correction procedures for e.g. fluorescence production depth and absorption, and mass absorption coefficients have been evaluated with high accuracy. This means that light elements can be quantified with an accuracy of a few percent (relative). Elemental mapping is possible by beam scanning.

method	electrons in, X-rays out
depth	about 1 μm
lateral extent	about 1 μm
beam-sample interaction	radiation damage for biological material
detection limits	typically 100 ppm
elemental range	Z greater than $_5$B
quanti- or qualitative	quant. using fundamental theory and calibration methods

Table 1.2 Characteristics of Electron Probe Micro Analysis

1.1.2 PIXE - Proton Induced X-ray Emission

Most commonly, proton beams (1-3 MeV) are used from cyclotrons or Van de Graaff generators. These beams can be focussed to a fine probe of about 1 μm in diameter and sub-micron beams are in development. The signal- to-background ratio for char-

method	ions in, X-rays out
depth	1 μm - 100 μm (depends on element line and matrix)
lateral extent	about 1 μm
beam-sample interaction	radiation damage for biological material
detection limits	typically 1 ppm
elemental range	Z greater than $_{12}$Mg
quanti- or qualitative	quant. using fundamental theory and calibration methods

Table 1.3 Characteristics of Particle Induced X-ray Emission

acteristic X-ray lines is significantly better, by about a factor 100, compared to excitation by electrons of energy 10-50 keV, yielding relative detection limits in the $\mu g g^{-1}$ range.

The sensitivity is, however, strongly dependent on both element detected and the matrix, and the time required for measurements giving a detection limit of this order can vary widely, typically from a few minutes up to an hour. Quantification is straightforward with (relative) sensitivity factors. Accuracy is comparable to that of EPMA. In addition, the use of focussed proton beams makes it possible to perform a microanalysis using other signals resulting from the beam-specimen interaction, e.g. Rutherford Backscattering (RBS), Prompt Radiation Analysis (PRA) and Nuclear Reaction Analysis (NRA). Elemental mapping is possible by beam or sample scanning. Often recognized as a disadvantage of PIXE is its need for a MV ion accelerator, which limits the technique to fewer laboratories.

1.1.3 LAMMA - Laser Microprobe Mass Analysis

In this method a laser is used as excitation source and by optical focussing a lateral resolution of about 1μm can be obtained. A high power pulse from the laser vaporizes the sample, creating a small plasma in which ions from the molecules or their fragments present are produced. These ions are extracted and analysed using preferentially a time-of-flight mass spectrometer. The degree of ionization in the plasma, and the extent to which sample molecules are fragmented vary greatly from one matrix to another. Conse-

method	photons in, ions out
depth	about 1 μm
lateral extent	1 - 5 μm
beam-sample interaction	destructive
detection limits	typically 10 ppm
elemental range	Z greater than $_1$H
quanti- or qualitative	semi-quantitative

Table 1.4 Characteristics of Laser Microprobe Mass Analysis

quently, comparison with nearly identical standards or internal standards is most useful for semi-quantitative estimates of concentrations. Typical relative detection limits are in the low $\mu g g^{-1}$ range.

1.1.4 SIMS - Secondary Ion Mass Spectrometry

The SIMS technique is based on excitation through the impact of ions in the energy range E=1-20 keV. By varying the energy and the type of primary ions (O_2^+, O^-, Ar^+, Cs^+) the mass spectrum obtained can be thoroughly optimized by the experimental conditions. The detection limits range from ngg^{-1} to μgg^{-1}. Limitations of SIMS are the complexity of the mass spectra and the severe matrix effects. Quantification is difficult, because the complex processes in the plasma are not fully understood.

method	ions in, ions out
depth	0.5 nm
lateral extent	0.5 µm
beam-sample interaction	destructive
detection limits	typically 10 ppb
elemental range	Z greater than $_1$H
quanti- or qualitative	semi-quantitative

Table 1.5 Characteristics of Secondary Ion Mass Spectrometry

1.1.5 SXRF - Synchrotron X-ray Fluorescence

Basically SXRF is not different from XRF performed with an X-ray tube. However, SXRF has a number of advantages, which makes it very attractive for a microprobe, such as a continuous spectrum with high intensity covering many orders of magnitude in wavelength, a high degree of polarisation, resulting in lower background, and natural collimation which makes it very attractive for focussing. Compared to focussing light or

method	X-rays in, X-rays out
depth	10 µm - 10 mm
lateral extent	1 - 10 µm
beam-sample interaction	non - destructive
detection limits	typically 50 ppb
elemental range	Z greater than $_5$B
quanti- or qualitative	quant. using fundamental theory and calibration methods

Table 1.6 Characteristics of Synchrotron X-ray Fluorescence

charged particles the optics necessary to focus X-rays are much more complicated. The lateral resolution of existing focussed beams is in the 1-10 μm range. Typical minimum detection limits are in the sub-ppm level. Advantages of a Synchrotron microprobe include less beam or radiation damage and the smaller demand for vacuum. The main disadvantage is its lack of convenience, because of the limited number of synchrotron sources where microprobes are available and its accessibility.

1.2 SXRF compared to other analytical microtechniques

1.2.1 Mass spectrometric and X-ray spectrometric methods

With the continued advance of experimental techniques it is possible to analyse the elemental composition and distribution of a material using focussed electrons, protons, heavy ions and photons (light and X-rays). Two classes of techniques can be distinguished: the mass and the X-ray spectrometric methods. LAMMA and SIMS are mass spectrometric techniques and EPMA, PIXE and SXRF are X-ray spectrometric techniques, where the detection system is a mass and an X-ray spectrometer respectively.

In general, X-ray spectrometric methods are quantitative, because the interaction of the incoming particle and the matrix is understood and can be described by theoretical models. Quantitative results can be obtained by calibration and/or theoretical models. The physics underlying the interaction process of the incident beam and the matrix for mass spectrometric methods is not fully understood. Therefore quantification is difficult and can only be obtained by calibration with external standards with very similar composition. Another difference between the two methods is that mass spectrometric techniques are necessarily destructive and X-ray spectrometric techniques are non-destructive as far as the incoming beam does not cause specimen damage.

1.2.2 Features of X-rays and synchrotron radiation

A feature of X-rays is that their interaction probability with atoms exhibits sharp peaks. The peaks occur in the energy region where the photoelectric cross-section for the creation of an inner-shell vacancy goes from zero to its maximum value as the incident photon energy is increased beyond a threshold value necessary to eject the bound elec-

tron. Thus a resonance exists with each electron energy level that is not available with electrons or protons as exciting particles. The sharp resonance, which can be used for selective excitation, accounts for an additional attraction of XRF for elemental analysis.

Synchrotron radiation offers a broad continuous spectrum of X-rays from which an excitation energy can be selected with a monochromator. In addition, X-rays have fluorescence cross-sections 10 - 10^3 times higher and fluorescence signal to background ratios 10 - 10^3 times larger than electrons or protons. X-rays also deposit 10^{-3} - 10^{-5} as much energy in the sample for the same minimum detection limit [Che84a]. These estimates imply lower minimum detection limits and reduced heat and radiation damage to the material under study, depending upon the experimental conditions. Comparison of electron, proton and photon excited X-ray fluorescence applied to trace element analysis can be found in e.g. Cooper, Sparks et al. and Grodzins [Coo73, Spa79, Gro83] and in Kirz et al. [Kiz78] for radiation damage.

Other useful features of synchrotron radiation are the polarisation and the natural collimation of the X-ray beam. The X-ray beam is almost linearly polarised in the plane of the electrons in the ring, and therefore a high reduction of incoherent (Compton) scattering can be obtained by positioning the X-ray detector in this plane and at 90° with respect to the incident beam. The natural collimation is very attractive for the construction of microprobes, because even at long distance the acceptance of the optics can be high.

Compared to other microprobes the spatial resolution is still poor (1 - 10 μm). Photons are not charged and therefore electromagnetic lenses as used for focussing electrons and protons can not be applied. High energy photons (X-rays) and low energy photons (light) interact very differently with material and as a result dioptric focussing with lenses is not an option. This is the reason that special focussing techniques for X-rays have been developed (see Chapter 2). A part of the investigation presented in this thesis is devoted to the development of focussing devices for hard X-rays (E>10 keV).

Another important advantage of the use of X-rays is that the specimen may be examined in its natural environment and does not need to be in a vacuum, which is of particular interest for the study of wet samples, such as biological specimens.

Recent reviews of the application of different analytical techniques to the study of geological and inorganic materials as well as on surface characterisation, which highlight current trends, can be found in Jackson et al. [Jac89] and Fulghum et al. [Ful89].

1.3 Aim of the investigation

The investigation is directed to the design and the construction of a Synchrotron X-ray microprobe facility at the SRS, Daresbury (UK), which is able to perform trace element analysis at ppm or sub-ppm level with spatial resolution of the order of 10 µm. As will be shown in the chapter reviewing the literature, X-ray optics have already been developed in the early 50s, but the construction of an X-ray microprobe failed both because of low intensity X-ray sources and a lack of the technology necessary to produce precisely figured and extremely smooth optical shapes. These problems can now be tackled with the availability of high intensity Synchrotron X-ray sources and high technology CNC-machines. As mentioned previously, the most difficult part of the construction of a Synchrotron microprobe is the manufacture of the X-ray optics for focussing hard X-rays. Although the ellipsoidally concave bent crystal which is used as the focussing device for the Daresbury X-ray microprobe has been developed for trace element analysis, the focussing crystal and optics can also benefit applications in other X-ray fields such as e.g. scanning X-ray microscopy, X-ray image transmission, X-ray spectroscopy, X-ray interferometry, focussing X-ray topography, X-ray lithography and X-ray tomography [Rie89].

1.4 Content of the thesis

In this thesis the development and performance of the Daresbury photon microprobe setup are described. The capabilities and analytical features of the setup for micro-SXRF are shown as well as some applications of the microbeam in different research areas.

Chapter 2 is a review of the literature concerning X-ray focussing in general, the application of synchrotron radiation for trace element analysis and the design and development of synchrotron photon microprobes for trace element analysis.

Chapter 3 describes methods developed to calculate and to judge the quality of different optical elements and configurations. These methods are aberration theory and ray-tracing.

Chapter 4 deals with the criteria for the design of the microprobe as well as the construction of focussing crystals.

Chapter 5 describes the experimental setup, tests and the measured specifications. The analytical features, sensitivities and minimum detection limits are presented as well as some applications of the microbeam in different research fields. These measurements show the potential of the Daresbury X-ray microprobe.

In Chapter 6 calculations show what can be expected if the ESRF (Grenoble) source parameters are used rather than the SRS (Daresbury) source parameters for different shapes and different combinations of optical components.

Finally, Chapter 7 deals with discussion, conclusions and recommendations for future work.

Chapter 2

Focussing of X-rays

2.1 The focussing of X-rays in general

About twenty years after Röntgen discovered X-rays in 1895, de Broglie and Lindemann [Bro14] and Rohmann [Roh14] showed in 1914 that X-rays are focussed by a cylindrically bent sheet of mica, by registering the many diffracted beams on a photographic plate. In 1916 Gouy [Gou16] pointed out that cylindrically bent crystals have the property to give monochromatic stigmatic images of linear X-ray sources placed near the cylinder axis. No experimental realization of this idea was known until von Hámos [Ham 32,33] published the results of his experiments in 1932 and 1933. The X-ray images are mostly related to the X-ray photographs used in medicine and other fields of radiography. Cylindrical crystals have also been used in X-ray spectroscopy in the so called "focussing spectrographs". The first operational focussing monochromators and spectrographs using bent crystals were designed and built by Johann [Joh31] and Cauchois [Cau32a,32b,33,34]. A detailed review of bent monochromators has been given by Roberts and Parrish [Rob68]. The important difference between the paths of rays in these arrangements and in the arrangement giving true X-ray images is that it is only in the latter arrangement that there exists a correspondence between the points of the source and the points of the image [Ham39]. The possibility of obtaining X-ray images by specular reflection at grazing incidence from the surface of curved mirrors was mentioned as early as 1929 by Jentzsch [Jen29] and the concept was revived in the late 1940s by Ehrenberg [Ehr47,49] and Kirkpatrick and Baez [Kir48].

At that time and continuing into the 1950s theoretical work and some experimental effort were devoted mainly to the study and development of X-ray microscopes [Cos60]. The initial enthusiasm slowly evaporated after it became evident that the achievement of high resolution was beset with experimental difficulties, particularly related to the problems of producing very precisely figured and extremely smooth mirrors. The 1960s saw a revival of X-ray optics stimulated by the prospects of carrying X-ray telescopes on rockets and satellites above the atmosphere, in order to study extraterrestrial X-ray sources

[Fra77]. Since the second half of the 1970s X-ray scientists have been challenged to study, design and build new optical devices such as mirrors, crystals, different types of monochromators, gratings, multilayers etc. with renewed interest because of intense synchrotron X-ray sources available at electron storage rings all over the world [Pro78]. After synchrotron radiation had been used as a tool for trace element analysis [Gor82, Bos84, Spa80] in the early 1980s, scientists became more interested in the design and realization of X-ray microprobes [Spa80, Pri84a,b, Che84a]. This development can be compared to the evolution of proton beams to smaller dimensions, only the latter development is more than a decade in advance over the X-ray microbeam development. In brief, two domains of focussing optics can be distinguished:

- **Imaging optics:** In fields such as radiography, X-ray microscopy and X-ray telescopy, where one-to-one images are important, the image formation is strongly dependent on the aberrations involved in the optics. The final resolution is more significant than the intensity of the X-ray beam.

- **Non-imaging optics:** In fields such as X-ray spectroscopy, EXAFS and Trace Element Analysis the optics are chosen in such a way that the highest flux density will be obtained and the criterion of one-to-one image is of no importance. Although the optics is defined as non-imaging, (trace) element mapping can be carried out by scanning techniques [Gur87, Bav88, Jon89, Gor90].

2.2 The focussing of X-rays for synchrotron microprobes

2.2.1 Advantages of synchrotron microprobes

In this paragraph attention is focussed on the published material concerning synchrotron microprobes applied to Trace Element Analysis. These reports about the design of X-ray microprobes have been published mainly in the first half of the 1980s. In a review article Chen et al. [Che84a] mentioned the advantages of X-ray microprobes over electron- and proton microprobes used for elemental analysis. These advantages have been documented by Sparks [Spa80a], Gordon [Gor82,83] and Grodzins [Gro83]. Briefly, they include:

- **Higher signal to background ratio:** The fluorescence S/B ratio from X-ray excitation is 10^2 - 10^3 times greater than that from electron excitation and 10 times greater than that from proton excitation.

- **Lower energy deposition:** X-rays deposit 10^3 - 10^5 times less energy in the sample for the same elemental detectability compared to electrons and protons. Thus the likelihood of breaking chemical bonds, redistributing and/or volatilizing susceptible elements, e.g. Br and As, is less with X-ray excitation.

- **Favourable operating conditions:** Sample analysis with X-rays can be carried out in a non-vacuum environment e.g. in air, helium, aqueous surroundings etc.

- **Lower minimum detection limits:** Under optimum conditions, MDL's as low as 10 ppm can be achieved with electron probes, but in routine analysis for most elements the practical lower limit of detection is about 100 ppm. With a proton microprobe detection limits of about 10 ppm have been reported. X-ray setups have achieved measured MDL's of 10-100 ppb.

- **Higher penetrating depth**: A disadvantage of X-ray fluorescence microprobes is sometimes the much higher penetrating depth of X-rays. In Carbon a 15 keV electron has a range of 2.5 μm; a 3 MeV proton has a range of 73 μm; whereas a 20 keV photon has a mean free path of about 1 cm.

2.2.2 X-ray focussing techniques

The absence of X-ray ($\lambda \sim 0.1$ nm) optics analogous to light optics is due to the fact that in practice X-rays are not refracted by materials. This is because the refractive index (n) is only slightly smaller than one ($1-n \sim 10^{-5}$ - 10^{-6}). In consequence, X-rays can be reflected externally in going from an electronic less dense medium to an electronic denser medium. This is in contrast to light. Alternative focussing techniques have been developed for X-rays. There are at least six ways to obtain synchrotron X-ray microbeams:

- Collimation of the synchrotron beam by the use of appropriate slits or pinholes [Che84a,b, Pet84,86, Bav88, Riv89];
- The use of (Bragg-) Fresnel zone plates [Sch84, Ari87,89a,b];

- Specular reflection from metal coated curved mirror surfaces [Jon87];
- Glancing incidence gratings [Het86];
- Bragg diffraction from (doubly) bent crystallographic planes [Lan87, Lan90a, Bar89a,b, Ant89];
- Reflection from Layered Synthetic Microstructures or multilayers [Und81, Bil83, Pia88, Dhe89].

2.2.2.1 Pinholes

The simplest way to obtain small beams of about 10 μm in diameter is by reduction of the beam size. This can be done by collimating the synchrotron beam by the use of appropriate slits and/or pinholes. Pinholes often consist of a layered structure of distinct materials, such as platinum/gold [Riv89] or platinum/iridium [Pet86]. These sandwich materials are needed to absorb not only the primary beam but also the characteristic X-rays of the main absorber. A material often used for slits is tantalum. Small holes in these materials can be produced by laser drilling or by spark sputtering techniques.

2.2.2.2 Zone plates

The only X-ray focussing optic which has been used successfully to give submicrometre resolution in the soft X-ray regime is the Fresnel zone plate. A Fresnel zone plate is a device which acts as a lens. The focal length of, and the object and image distances in the image formation by, a zone plate are related in the same way as for a conventional lens, described by the lens formula ($1/f = 1/o + 1/i$). Consider a plane wave of wavelength λ, travelling in a particular direction. The wavefront at a given instant of time may be divided into a number of concentric zones in such a way that each zone is one-half of a wavelength farther away from a point P on the optical axis than the next smaller zone. The elementary zone plate is a thin membrane with a radially symmetric set of concentric rings comprising transparent and opaque areas. Each alternate zone is rendered opaque so that the contributions at point P from the remaining zones all add in phase [Mey72]. Zone plates capable of imaging specimens to a resolution better than 1/10th of a micrometre can be produced either by optical interferometric techniques or by lithography using a scanning electron microscope [Duk90].

Kirz [Kiz74] mentions the following disadvantages of zoneplates: (i) their light collecting power is very poor, (ii) they suffer from high background, (iii) they are highly chromatic and (iv) they are difficult to produce. Published material on Fresnel zoneplates will not be further examined, because they are mainly used in X-ray microscopy for obtaining high quality images in the soft x-ray region ($\lambda > 0.15$ nm) [Sch84, Ari87]. For these reasons, for the construction of a synchrotron microprobe for trace element analysis zoneplates seem not to be very useful. Despite these disadvantages, recently Saitoh et al. [Sai89b] reported the development of circular zone plates for hard X-rays, fabricated by dc planar magnetron sputtering. These zone plates consisted of either 5 or 20 pairs of alternating WSi_2 and C layers. The minimum focal spot size attained, using 8 keV synchrotron radiation, was less than $3 \times 10\ \mu m^2$ in the vertical and horizontal directions respectively. The efficiency of the zone plate with 20 layer pairs was determined to be about 4.5%.

One other development on the Fresnel lens is worth mentioning, the so called Bragg-Fresnel lens. A crystal lattice at the exact Bragg position can be used as a diffractor for X-rays. Aristov and coworkers managed to produce zoneplates based on the idea of using Bragg diffraction on a crystal with a Fresnel zone structure artificially formed on its surface (a Bragg-Fresnel lens) [Ari87,88,89]. These devices do not have the limitations mentioned previously for Fresnel zone plates. The Bragg-Fresnel lens is still in development and seems very promising also for hard X-rays.

2.2.2.3 Mirrors

The refractive index of all materials for visible radiation is greater than one. In the far ultra-violet its value decreases rapidly to below unity. It is found that total reflection takes place at a surface for rays arriving from the less dense medium, and not from the denser medium as with light. For rays incident at angles smaller than the critical angle (~ 1 mrad) a surface behaves like a mirror and reflection is almost 100% efficient for very short wavelengths, such as X-rays. High quality mirrors can be obtained by carefully polishing the surface. Often a polished substrate (e.g. glass) is used as a mirror with a deposited layer of a high Z material (e.g. platinum or gold) to enlarge the critical angle for total reflection.

2.2.2.4 Gratings

The dispersive element in grating light or X-ray dispersion is the optical grating. This is a planar or concave, transparent or reflecting surface upon which there are rulings at regular distances. The distance between the rulings is the ruling constant (grating constant). Gratings can be regarded as a surface upon which there are a great number of parallel, regularly spaced, narrow slits. Thus the grating consists of a surface interrupted by grooves which play no part in the diffraction process. The spacing between the slits, the grating constant, has the same order of magnitude as the wavelength of the radiation to be dispersed. Among gratings the low-performance types are transmission gratings, while the higher-performance types operate on the reflecting principle [Mik74]. In the wavelength region below 30 nm, gratings are used exclusively in the grazing-incidence configuration. In practice, optical gratings are limited in their use for wavelengths down to the soft X-ray region. Gratings are usually produced by photofabrication methods [Fra77].

2.2.2.5 Crystals

The reflection of X-rays at a smooth surface, as described above, is essentially similar to specular reflection in light optics and is governed by the same laws. Unlike visible radiations, X-rays are reflected also from crystals. The 'reflection' is due to diffraction from the regular lattice formed by the constituent atoms, and will thus occur only in certain well defined directions, described by Bragg's law. As this is a three-dimensional structure the 'reflecting' surface is not necessarily the physical surface of the crystal. Especially nowadays high purity single crystals, such as Si and Ge, of high surface quality and large dimensions (~10 cm) can be obtained from the semiconductor industry.

2.2.2.6 Multilayers

Multilayers or Layered Synthetic Microstructures are manmade periodic layered structures of high enough quality to be considered as synthetic crystals. Layers of materials A and B having significant difference in their scattering powers for X-rays and uniform thicknesses t_a and t_b are combined to form a sample of uniform period $d=t_a+t_b$. The

spacing d is equivalent to the Bragg spacing in natural crystals. Layer thicknesses may be varied in several ways during synthesis [Bar84]. The main technologies used at present to prepare short periods over large surfaces are obtained with sputtering processes [Dhe89].

2.2.3 Design of synchrotron microprobes

From 1980 the number of publications dealing with synchrotron radiation optics and the design and construction of microprobe systems for trace element analysis has been increasing. In general terms, Deslattes [Des80] comments on the use of monochromators and mirrors as well as on the effect of curvature and asymmetry of crystal planes.

Sparks et al. [Spa80b] mention the relative merits of crystals compared to mirrors for focussing synchrotron radiation at energies above 10 keV. As mirrors have critical angles of reflection typically 1/20 of the Bragg scattering angles for crystals, large mirror surface areas are required. Sagittal focussing is weak for mirrors and limits the amount of radiation intercepted. The authors show by calculation what size of focus one can expect using cylindrically bent crystals, considering the NSLS synchrotron X-ray source as a point source. Also Heald [Hea82] reports on the limitations in applying bent cylindrical mirrors to X-ray beam lines.

Howells et al. [Hws83] propose a multilayer coated Kirkpatrick-Baez mirror (see also [Kir48]) (d = 2 nm, f = 0.2 m) to focus and monochromate radiation from 2-16 keV in the horizontal plane, followed by a vertically focussing mirror to achieve a beam spot of 3 μm.

Ice et al. [Ice84,88] examine mirror, multilayer and crystal combinations from the point of view of producing the most intense image of the source, tunability, energy range and energy resolution. The authors compare at 15 keV the ray tracing results from a non-dispersive multilayer system, a Kirkpatrick-Baez system and a doubly curved Ge(111) crystal. The Monte-Carlo simulations for each system show that intensities over 10^8 ph/(s. μm^2) are possible.

Si(111) crystals have been tested by Batterman et al. [Bat83] and Mills et al. [Mil86]. They used slotted bent crystals in order to prevent anticlastic bending as described by Sparks et al. [Spa82]. The entire crystal and bending device is so arranged that, coupled with the first crystal, a fixed exit beam height is maintained for all energies.

Gordon et al. [Gor87] described the design of a microprobe facility using a double monochromator followed by an 8:1 demagnification ellipsoidal mirror. It will focus the centre 240 μm of the source through the 30 μm pinhole to be placed about 4 mm in front of the target. According to the authors, sensitivity calculations predict detection limits in the 50 to 100 ppb range for 60 sec counting times using a solid state detector.

Bilderback et al. [Bil83] made a design of a doubly focussing tunable (5-30 keV), wide bandpass optical system, made from layered synthetic micro-structures (LSM). The first element is thought to be a LSM deposited on a water cooled substrate in order to be able to intercept the direct synchrotron beam. It can be bent for vertical focussing and a whole set of LSM's should be available to cover the energy range of interest. The second LSM consists of a structure with a 10% bandpass built onto a flexible substrate that can be bent for sagittal focussing.

Prins et al. [Pri83,84a,b] report on the design of an X-ray microprobe at the SRS, Daresbury (U.K.). A doubly bent Si(111) crystal is chosen as the focussing element and an intensity of $\sim 10^8$ ph/(s.μm^2) has been calculated for a 50×50 μm^2 spotsize.

2.3 Experimental work with synchrotron microprobes

2.3.1 Collimated systems

As mentioned in the previous paragraph, the most simple way to obtain a microprobe is by placing a pinhole in the white beam. The two main disadvantages are obvious. Firstly, no increase in flux density takes place by the lack of any focussing action and secondly, there is no energy definition in the beam, except the possibility to filter out low energy radiation, which worsens the detection limits obtainable.

Very useful work with a collimated system is possible as is nicely illustrated by Pe-

tersen et al. [Pet84,86]. The authors collimated the beam in two steps, namely with a first aperture (>200 μm) made of lead and a second collimator consisting of one of a set of pinholes ranging from 10 - 150 μm. Results are reported of measurements on carbon samples and aerosols.

Bavdaz et al. [Bav88] report on the use of a 1:1 mirror in front of the collimation in order to cut off higher energies, and the use of slit apertures as collimators. The authors claim resolutions better than 10 μm and show an example of an application on a space particle, collected by a high flying NASA aircraft.The second example shows the spectra of the printing ink of two precious antique documents printed by Gutenberg.

Chen et al. [Che84b,87] also use collimated beams, sometimes in combination with a channel cut Si-monochromator. The reported spot sizes vary from $20 \times 20\ \mu m^2$ to $75 \times 75\ \mu m^2$.

Another interesting application is the use of pinholes in combination with an undulator source. The radiation from an undulator is extremely intense, highly collimated in both the horizontal and vertical directions and is monochromatic with a bandwidth of about 1% [Riv89]. Rivers et al. [Riv89] used laser drilled pinholes 5 - 10 μm in diameter in 25 μm Pt and 100 μm Au, which were placed in a beam from an undulator a few mm upstream of the sample. The authors claim to have obtained better sensitivities with this beam of 10 μm resolution than using ordinary white bending magnet radiation.

2.3.2 Focussed systems

2.3.2.1 Cambridge (USA)

One of the first descriptions of focussing devices used to produce a synchrotron microbeam is given by Howell et al. [How75] and used in the first microprobe at the Cambridge Electron Accelerator [Hor72]. In addition to a mathematical formalism given to calculate the necessary mirror dimensions, experimental results are shown of the spot obtained at that time (1972-1973). The bent cylindrical mirror was made out of fused quartz; the cylinder had a radius of 10 cm and the surface area was $10 \times 60\ cm^2$.

2.3.2.2 Ithaca (USA)

Bilderback et al. [Bil86] show results of a focussing system consisting of a 10 × 60 cm^2 Pt-coated reflecting surface that can be elastically bent from a radius of 400 m to infinity. This mirror receives horizontally focussed X-rays after they are diffracted from a bent asymmetrically cut Ge(111) monochromator. In this way they focussed the beam in the vertical plane from 5 mm to 300 μm and they measured a flux of 3.10^{12} photons/s into a 1.5 × 0.3 mm^2 area. The X-ray energy was 8 keV; the storage ring operated at 5.3 GeV, 70 mA and the station was at a wiggler line intercepting 2 mrad.

2.3.2.3 Daresbury (UK)

Van Langevelde et al. [Lan87] and Lenglet et al. [Len87] describe the use of a doubly bent Si(111) crystal in a toroidal shape in order to focus X-rays of 20 keV. The authors use 100 μm thick Si wafers with a diameter of 50 mm. The minimum value of the sagittal radius of curvature is about 10 cm to prevent breaking of the crystal. In order to obtain an astigmatic optical system, it is shown that for the chosen energy the meridional curvature should be 10 m. The crystal was attached to an Al-mould of the appropriate shape using polyethylene foil as adhesive. The crystal is placed directly in the white beam and acts as both monochromator and focussing unit. The optics was tested at Daresbury on a wiggler station, while the ring was running at 2 GeV and ~100mA. The measured flux density was 200 ph/(s.mA.μm^2). As an example the setup was used to scan over the cross section of a coronary artery [Len88]. Recently, the authors replaced the toroidally shaped crystal by an ellipsoid, for which the mould is made on a computerized lathe. Van Langevelde [Lan90a] reports better focussing properties and, also important, flux densities at least 2 orders of magnitude better than the values obtained with a toroid (see Chapter 5).

2.3.2.4 Brookhaven (USA)

Another method of focussing the beam is described by Thompson et al. [Tho87, 88,89] and Underwood et al. [Und86,88]. They use two spherical mirrors in a Kirkpatrick-Baez geometry [Kir48] which considerably reduces the astigmatism inherent to

spherical mirrors for images of off-axis points. In order to have a high flux beam, the authors use multilayer reflectors selecting a relatively wide bandpass of about 1 keV at the selected energy of 10 keV. The mirrors are made by the deposition of alternating layers of two elemental materials to form a structure of periodically varying electron density and hence of varying complex refractive index. The layers must be extremely thin, but, recently, evaporation and sputtering techniques have been developed that allow layers as thin as .75 nm to be achieved. It is obvious that in addition extreme demands are set on the smoothness of the substrate. For their measurements, the authors use two different mirrors. The upstream mirror was coated with 200 layers of W and C with a 2d spacing of 5.8 nm, the second mirror with 100 layer pairs with a spacing of 8.7 nm. The beamspot obtained is less than $10 \times 10\ \mu m^2$ and the available intensities 10^8 to 10^9 photons/s, depending on the experimental station used.

The first applications of this set up include the measurement of the Fe distribution along a filament of blue-green algae [Gia88], a number of spot measurements on a tissue section of rat melanoma [Tho88] and measurements on fluid inclusions containing an aqueous calcium chloride solution [Fra88].

2.3.2.5 Novosibirsk (USSR)

The design of a synchrotron radiation X-ray fluorescence analysis station installed at the VEPP-3, Novosibirsk (USSR) (using highly bent crystal monochromators made from formed pyrolytic graphite)is described by Antonov et al. [Ant89] and Baryshev et al. [Bar89a,b] . Samples are excited by monochromatized synchrotron radiation beams produced by placing a crystal monochromator behind a 2T wiggler magnet. The ring operated at 2 GeV and 100-200 mA. A conic formed crystal of pyrolytic 40 mm long graphite with 20 mm (entrance) and 12 mm (exit) bending radii was used as the monochromator and focussing device. Such a crystal makes it possible to obtain a quasi-monochromatic X-ray beam within a 20-29 keV energy range with a spectral width of 20%-30% and a minimum focal size of 1.5 to 2 mm. The flux increase compared to a flat graphite monochromator was a factor of 20. Using a scanning system, the authors obtained elemental maps of geological and biological objects at concentrations down to 1 ppm and spatial resolution down to 30 μm by the use of collimators.

2.3.2.6 Tsukuba (Japan)

The advantage of using mirrors is that below the energy corresponding to the critical angle the focussing properties are energy independent. In combination with filters to cut off low energies, broad band excitation is feasible while maintaining good focussing properties. The production of these mirrors, however, is not easy. Moreover, mirror surfaces are very sensitive to deposits and surface alterations influenced by the beam. Owing to the glancing incidence of a few mrad, the mirror has to be quite large in order to intercept a sufficient part of the beam. Goshi et al. [Gos87] adopted the Wolter type I mirror system [Wol52]. The synchrotron radiation X-ray microanalyzer was installed on the beamline 4A at the Photon Factory (Japan). The design considerations were described by Aoki et al. [Aok87] and Goshi et al. [Gos88]. Hayakawa et al. [Hay89a,b] obtained a minimum beam size of 1.6 μm in the sagittal plane and 34 μm in the meridional plane using a condensor mirror, which brings the beam to an intermediate focus which serves as a source for the focussing Wolter mirrors. The operating energy was 10 keV and the authors claim sufficient flux to perform trace element analysis.

2.4 The focussing of X-rays for laboratory-based microprobes

Although the most serious limitation to the use of X-rays in microfluorescence on microprobe application is the lack of intensity, the construction of laboratory-based X-ray microprobe is in development. Wittry [Wit89] et al. report about the possibility of a laboratory instrument based on doubly curved crystals. The experiments consisted of cutting thin, cylindrically curved lamellae of single crystal germanium (111), polishing and bending them at an elevated temperature over a spherical mould. A spherical mould can be used because the Bragg angle for the (333) reflection of the copper line is nearly 45 degrees. Only three or four characteristic X-ray lines are needed to excite most of the elements, so the use of three or four single crystal diffractors, bent to a curvature such that all have the same source-to-image distance, configured in the Johansson geometry, gives a practical instrument for microprobe X-ray fluorescence analysis.

A laboratory-based X-ray microprobe, composed of a high-brilliance microfocus X-ray tube coupled with a small glass capillary, has been developed for material applica-

tions [Car89]. The authors show that a spatial resolution between 5 and 6 μm is possible by the use of a 10 μm glass capillary. Because of total external reflection of X-rays from the smooth inside bore of the Pyrex-glass capillary, intensity gains of as much as 180 fold compared to aperture collimation only were obtained. The laboratory X-ray microprobe has been used for the detection of the bulk composition of metals, ceramics and geological materials.

Chapter 3

Aberration theory and ray-tracing

3.1 Introduction

For the design of an optical system, information about the image forming qualities is needed. If a point object can be projected into a point image, then the system is said to be "diffraction limited" [Hws83]. However there are other limitations besides diffraction that prevent an image from being a true likeness of the object. These are called aberrations. Some of them are known as regular, such as geometrical or chromatic aberrations, others are "irregular", such as for instance aberrations due to strain in crystals resulting from either dislocations or surface defects or deformation due to the heat load dissipated by the synchrotron beam.

Historically the first method of judging optical systems is based upon aberration or Seidel theory [Dri78]. Another method is ray-tracing, which is often used to calculate the optical path of many rays, with different starting conditions, to simulate a whole beamline with different optical components by fast computer codes [Dri78]. The results then are not in terms of aberration coefficients but in terms of distributions of relative intensities. This chapter deals with aberration theory and ray-tracing. Aberration theory is used to derive the necessary focus conditions and to calculate the first non-zero coefficients of the main aberration terms. Ray-tracing is used to design the optical components (reflectors or Bragg diffractors) of the microprobe, implemented in the computer code as geometrical surfaces.

3.2 Aberration theory

3.2.1 Introduction

The usual method in aberration theory to evaluate the projection of the object on the image plane is to consider the "Eikonal function", i.e. the characteristic function connected to the optical length of each ray through the optical system [Buc70]. The characteristic function of an optical system is approximated by a polynomial, containing terms

up to the third, fifth or seventh order. The geometrical optical aberrations are obtained by a derivative of the difference of the optical path function of the principal ray and a skew ray which is supposed to be reflected or diffracted (see section 3.2.2). The best image is then determined by considering the conditions in which the first terms of the derived series vanish. Following Seidel's terminology, the image forming qualities can be described by five quantities: spherical aberration, coma, astigmatism, curvature of the field and distortion, which are related to coefficients of the polynomial. However for X-ray optical applications Seidel's theory can not be used to determine the aberration coefficients, because it holds only for symmetrical systems. Also principal rays, i.e. rays through the centre of the entrance pupil, are treated paraxially. This is in strong contrast to mirrors, multilayers and crystals as X-ray optical components where the principal rays always are far off axis or far off the normal of the optical surface. Beutler [Beu45], Haber [Hab50] and Namioka [Nam61] respectively showed that for spherical concave, toroidal and ellipsoidal concave gratings it is possible, to describe the optical path difference between a skew ray and the central or principal ray, ending up with terms related to quantities similar to those of Seidel. In the next section focus conditions for optical surfaces are derived following the procedure first described by Beutler for spherical gratings [Beu45].

3.2.2 Derivation of focus conditions

Mirror, multilayer and crystal systems with oblique incidence are non-centered systems where the "optical axis" of the components no longer coincides with the "instrument axis". The instrument axis or "zero axis" is that principal ray, i.e., a ray through the centre of the aperture diaphragm, which connects the centres of the object and image field. The treatment is restricted to those cases where all important centers lie in one plane, i.e. the meridional plane.

Consider a (semi)-symmetric, i.e. a plane of symmetry in the meridional plane, and regular optical system [Buc70]. An optical system is called regular with respect to a chosen coordinate basis if the characteristic function T can be written into a power series in terms of these coordinates. The characteristic function T describes the optical length in an optical system S with $T=T_0+t$, where T_0 is the optical path length of the principal ray,

t is called the aberration function, and all aberrations of S are absent if t=0. In practice the aberration function t is non-zero and therefore can be expanded into a power series. Following the procedure of Beutler the terms in the power series are rearranged in such a way that new terms T_n ($n \geq 1$) are formed. Each term T_n corresponds to particular powers and cross terms of the coordinates in which the optical surface is developed and can be related to Seidel's aberration quantities mentioned previously. According to Noda et al. [Nod74] the optical surface can be expressed as:

$$x = \sum_{i=0}^{\infty} \sum_{j=0}^{\infty} a_{ij} y^i z^j \qquad (3.1)$$

where $a_{00} = a_{10} = 0$ and j is even, owing to the position of the origin and the plane of symmetry (see fig. 3.1). Using Maclaurin's theorem [Arf71] the coefficients a_{ij} can be calculated for different optical surfaces or less formally by substituting equation 3.1 into

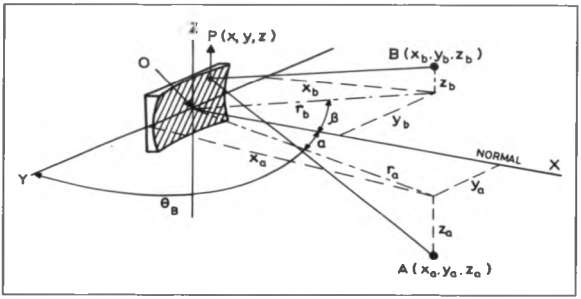

Fig. 3.1 Schematic diagram of the optical system

the equation of the optical surface and grouping the coefficients belonging to the same powers. Appendix 2 shows the equation of the optical surface for the following surfaces: meridional cylinder, sagittal cylinder, sphere, toroid, paraboloid and ellipsoid. The equa-

tion of the optical surface is based on the local cartesian system of coordinates where the principal ray connects the centre of the object, the origin and the centre of the image. Appendix 3 lists the coefficients a_{ij} up to the fourth order for these surfaces. According to Haber, it is assumed that a ray leaves the point A (x_a ,y_a ,z_a), hits the surface described by equation 3.1 and coefficients from Appendix 3 at point P (x,y,z), is then reflected and finally reaches point B (x_b ,y_b ,z_b) (see fig. 3.1). By varying the position of point P over the area of the surface, the various lengths of the paths AP and PB can be determined, and the formation and imperfections of the image can be examined. For the ray APB, the light path function T is:

$$T = AP + PB \tag{3.2}$$

with

$$AP = [(x_a - x)^2 + (y_a - y)^2 + (z_a - z)^2]^{\frac{1}{2}} \tag{3.3}$$

$$PB = [(x_b - x)^2 + (y_b - y)^2 + (z_b - z)^2]^{\frac{1}{2}} \tag{3.4}$$

$$x_a = r_a cos\alpha \tag{3.5}$$

$$y_a = r_a sin\alpha \tag{3.6}$$

$$x_b = r_b cos\beta \tag{3.7}$$

$$y_b = r_b sin\beta \tag{3.8}$$

In the equations 3.5 – 3.8 α and β are, respectively the angles of incidence and reflection, both measured in the xy-plane. The total light path function for a particular ray in terms of the coefficients a_{ij} can be derived by substituting equations 3.1 and 3.3 - 3.8 into 3.2 and carrying out power-series expansions. The total value of AP+PB expressed in the different coefficients a_{ij} can be found in Appendix 4.

In the theory of gratings there is an additional term in the light path function which describes the phase dependence related to the grating constant. The characteristic function represents the permissible lengths of the various light paths from A to B (see fig. 3.1), arriving with the same phase, as the point P wanders over the ruled surface of the grating in order to produce positive interference of the amplitudes. The geometrical shape of the grating is an integral part of the diffraction process and the image formation. Therefore diffraction and geometry cannot be treated separately, this in contrast to crystals and multilayers where Bragg diffraction can be considered to some extent independently from the geometrical shape.

As Beutler [Beu45] has demonstrated in detail for a spherical surface, the consecutive members of T_n (see also Appendix 4) have, individually, a physical significance as to the image formation and its imperfections. Also for surfaces other than a sphere the individual terms control the various conditions for the foci and for the image deficiencies in the following order: T_0 (optical path length of the principal ray), T_1 (condition for Bragg diffraction), T_2 (primary focus condition), T_3 (astigmatism), T_4 (coma), and T_5 (spherical, toriodal and elliptical aberrations). The conditions for a strict focus require that the partial derivatives of the consecutive members T_n with respect to the variables y and z vanish.

T_1: **Reflection condition** This term can be made zero for $|\alpha| = |\beta|$, this means the condition for symmetric Bragg reflection.

T_2: **Primary focus condition** By setting the lowest order term of $\partial T_2/\partial y$ to zero, the following equation expresses the primary focus condition (i.e. meridional focus):

$$\frac{1}{r_a} + \frac{1}{r_b} = \frac{4a_{20}}{sin\theta_B} \qquad (3.9)$$

where $|\alpha| = |\beta|$ and $\alpha = 90° - \theta_B$, if $a_{20} \neq 0$. The non-zero resulting terms in the series of $\partial T_2/\partial y$ are used to calculate the primary focus aberrations.

T_3: **Astigmatism** From the law of reflection it can be deduced that the relation

$$\frac{z_a}{r_a} = -\frac{z_b}{r_b} \tag{3.10}$$

holds. This relation is equivalent to the magnification.

Hence, the primary astigmatism condition, i.e. sagittal focus, is

$$\frac{1}{r_a} + \frac{1}{r_b} = 4a_{02}\sin\theta_B \tag{3.11}$$

if $a_{02} \neq 0$.

Combining the conditions described by equation 3.9 and 3.11 leads to

$$\sin^2\theta_B = \frac{a_{20}}{a_{02}} \tag{3.12}$$

for $a_{02} \neq 0$ and $a_{20} \neq 0$. The equations 3.9 and 3.11 are known as the Coddington equations and act as the lens formula. Suppose for instance a sphere with radius R, then, for dioptric focussing with lenses, equation 3.13 holds for light and 3.14 for X-rays [Fra77]:

$$\frac{1}{f} = \frac{2(n-1)}{R} \tag{3.13}$$

$$\frac{1}{f} = -\frac{2\delta}{R} \tag{3.14}$$

The symbol δ is known as the unit decrement of refractive index n of a particular material for X-rays. The negative sign in equation 3.14 indicates that the focussing action is in the opposite sense to that familiar with light; for an initially parallel beam of X-rays a biconvex lens will be divergent and a biconcave lens will be convergent. Reflection focussing of X-rays has the following meridional focal lengths for concave spherical shapes at the critical angle for mirrors (3.15), and at the Bragg angle for crystals (3.16) and multi-

layers (3.17) respectively:

$$\frac{1}{f_m} = \frac{2}{R\sqrt{2\delta}} \tag{3.15}$$

$$\frac{1}{f_m} = \frac{4d}{R\lambda} \tag{3.16}$$

$$\frac{1}{f_m} = \frac{4(d_A + d_B)}{R\lambda} \tag{3.17}$$

where d is the Bragg spacing and d_A+d_B the sum of the thicknesses of the alternating layers of material A and B in the multilayer. Equation 3.15 can be derived by substituting into the meridional part of the Coddington equations (3.9) the relation for total external reflection, i.e.:

$$sini_c = \sqrt{2\delta} \tag{3.18}$$

where i_c is the critical angle at which total reflection takes place [Fra77]. Equations 3.16 and 3.17 follow from substituting Bragg's law into equation 3.9, i.e.:

$$n\lambda = 2d sin\theta_B \tag{3.19}$$

where n is the order of reflection. By applying Bragg's law to equation 3.12 it turns out that the condition for astigmatism can be fulfilled for only one particular wavelength or energy, if the ratio of a_{20} and a_{02} is fixed. It can be deduced, using the coefficients a_{ij} from Appendix 3, that only the toroid and ellipsoid fulfill this condition. By choosing r_a, r_b and the energy, the ratio of the radii of curvature is a constant. For the toroid this is immediately obvious from the coefficients a_{02} and a_{20}. For the ellipsoid the local radii of curvature can be calculated using the analytical expression known from mathematical

textbooks:

$$R = \frac{[1 + (y')^2]^{\frac{3}{2}}}{|y''|} \tag{3.20}$$

The meridional radius of curvature applied to an ellipse defined as :

$$\frac{x^2}{a^2} + \frac{y^2}{b^2} = 1 \tag{3.21}$$

is

$$R_m = \frac{[a^4 + (b^2 - a^2)x^2]^{\frac{3}{2}}}{a^4 b} \tag{3.22}$$

The sagittal and meridional radii are found to be the same as the ones of the toroid for the same parameters r_a, r_b and θ_B.

For applications of crystals in the X-ray regime, using the focus conditions, the remaining terms T_4 and T_5 cannot be made zero. Since the partial derivatives have the geometrical significance of angles, the displacement of the diffracted rays from the true focus B can be calculated. The displacement is given by:

$$\Delta_n = r_b \cdot \left[\frac{\partial T_n}{\partial v}\right] \cdot \left[\frac{1}{cos\phi}\right] \tag{3.23}$$

where v is the respective variable (y for the meridional and z for the sagittal direction) and ϕ the angle between the reflected ray and the normal of the focal plane at B. In the next section the displacements are calculated for the main terms for an actual situation.

3.2.3 Calculation of aberration terms

To give an idea of the different aberrations for an actual situation with realistic curvatures the following example is given. By realistic curvatures are meant those which still can be produced in practice and are useful for focussing. Suppose having a sagittal

cylinder, a toroid and an ellipsoid with experimental conditions as follows:

E	= 15 keV
θ_B	= 7.57° (for Si(111))
ρ	= 0.1 m and/or R = 5.74 m
r_a	= 80 m
r_b	= 0.38 m

with ρ the sagittal and R the meridional radius of curvature, respectively. The critical parameter is the sagittal radius of curvature. When this radius is fixed together with the crystal material, structure and exciting energy, the meridional radius of curvature follows from the astigmatism condition (equation 3.12). In this way the local radii (ρ, R) are determined and directly define the toroid. The set (r_a, r_b, θ_B) which defines the ellipsoid is dependent on the set (ρ, R, θ_B). With the assumption that the source is a point source and that reflection takes place at point P with coordinates (1,5) in mm in the yz-plane, then the various displacements can be calculated. Table 3.1 shows for the two-dimensional focussing surfaces, such as the toroid and the ellipsoid, that the displacements related to T_4 (coma) components are the main aberration terms.

	sagittal cylinder	**toroid**	**ellipsoid**
Δz_3	0.11 μm	0.11 μm	0.11 μm
Δz_4	6.4 μm	6.4 μm	0.064 μm
Δz_5	0 μm	0.011 μm	0.11 μm
Δy_2	130 μm	0.25 μm	0.002 μm
Δy_4	120 μm	120 μm	1.2 μm
Δy_5	0 μm	0.009 μm	0.32 μm

Table 3.1 Calculated displacements in the focal plane

The limitation of aberration theory applied to crystals is that more information of each point is needed than the location only. Rays are Bragg diffracted when they reach the crystal with an angle only slightly deviated from the Bragg angle. This "acceptance cone" is defined by the Darwin width. Thus not every point on the surface fulfills the necessary condition for Bragg reflection. To determine the angle of incidence rays have to be treated individually and therefore "ray-tracing" is needed.

3.3 Ray-tracing

3.3.1 Introduction

The ray-tracing technique has long been used to simulate radiation sources and beamlines. In particular, it is the increased implementation of insertion device sources, such as wigglers and undulators, as well as different types of optical components in the beamline, such as mirrors, multilayers and crystal monochromators (planar or curved) that has prompted the development of ray-tracing programs. As an example, SHADOW [Lai86a,b; Lai88] is a widely available ray-tracing program for designing synchrotron radiation beamline optics. The algorithm is based on geometrical optics. The rays are traced through the optical system formed by sequential geometrical surfaces. The program is specially oriented towards reflecting mirrors, although transmission systems (lenses) and multilayer coatings are also implemented. In addition the SRS program library includes a ray-tracing package for design optimization of optical elements (e.g. slits, classical and holographic gratings) that may be coplanar or orthogonal to each other in any configuration [Hub83, Pan83]. However, at the time when the design of a synchrotron microprobe at the SRS was started no general programs were available with which it was then possible to simulate a whole beamline with curved crystals as focussing devices for X-rays. A special computer code (named SIMUL) was developed to analyse the imaging characteristics of curved monochromator design.

3.3.2 Historic evaluation of the ray-tracing code SIMUL

The computer code SIMUL is a ray-tracing program, which is based on the program KRIS (1983), originating from the Eindhoven University of Technology. The program KRIS has been developed and used as an aid to the design of a crystal spectrometer with a spherical surface as optical surface. Owing to errors in KRIS, it has been rewritten by Reinhoudt [Rei85] and is called SIM. The program SIMUL is the modified version of SIM for synchrotron radiation use. The spherical surface has been replaced by a toroid, which has been implemented by Jennekens [Jen85]. The program is written in F77 and the original runable version is operational in the language RT-11.

3.3.3 Modification and development of the ray-tracing code SIMUL

The Amsterdam modified version of SIMUL is operational under UNIX*. Over the years the development of the program has undergone different stages. In the first instance only toroidal surfaces could be ray-traced. The intersection of a ray and the surface was solved exactly. For surfaces other than toroids the exact solution of the fourth order equation is cumbersome. To tackle this problem in a general way, another approach has been chosen. Spencer et al. [Spe62] described a ray-tracing procedure applicable to systems of quite general type, which has been adopted. For the work reported in this thesis the following optical surfaces have been implemented: planar (Pl), sagittal cylinder (S.C.), meridional cylinder (M.C.), sphere (S), toroid (T), ellipsoid (E), paraboloid (P), elliptic plane (E.P.), parabolic plane (P.P.), elliptic cylinder (E.C.), parabolic cylinder (P.C.) and a logarithmic spiral (L.S.). The next version of the program was the extension to two successive optical elements, one configuration in the anti-parallel mode and the other in the Kirkpatrick-Baez geometry, where the elements are perpendicular. In the latest modified version concave as well as convex surfaces can be ray-traced.

3.3.4 Program execution of the ray-tracing code SIMUL

The basic idea of the ray-tracing program SIMUL is as follows. The program is based on the Monte Carlo method, which means that every starting ray has a randomly chosen position and direction within the given limits depending on the source size dimensions and beam divergences. The path of the ray through the optical system is calculated, and a ray is counted when it hits the optical surface at the Bragg angle within the Darwin width of the planar or curved crystal. Rays are stored in separate two dimensional arrays of 41x41 pixels, such as the source array, crystal array and image array. The chosen number of 41 pixels is based on a technical limitation of most terminals to display a number of digits on one line. The pixel size can be chosen freely. A difference with mirrors is that the crystals reflect X-rays differently according to energy. The program is run for a defined energy, so that the energy behaviour (and related chromatic aberrations) can be sorted out. A flow diagram of the program is shown in fig. 3.2.

UNIX is a trademark of AT&T Bell Laboratories

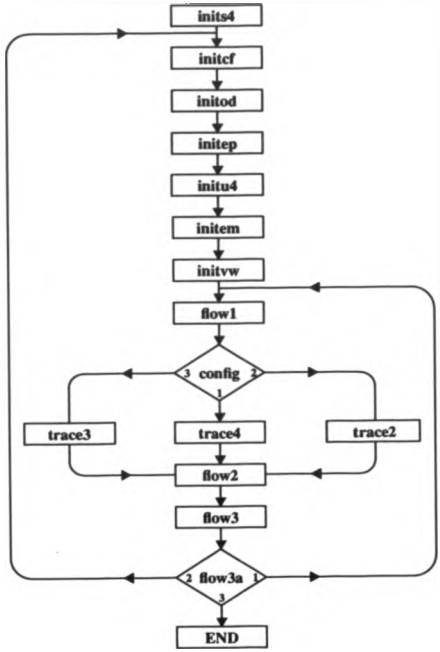

inits4: initialization of defaults
initcf: determination of the configuration
initod: set to zero of variables
initep: metres to millimetres
initu4: changing of defaults
initem: millimetres to metres
initvw: determination of the geometry

flow1: input number of rays (x 100)
trace x: determination of the intersection of the ray and the optical surface
trace2: Kirkpatrick-Baez I (vert.-hor.)
trace3: Kirkpatrick-Baez II (hor.-vert.)
trace4: Bridge (anti-parallel mode)
flow2: output ?
flow3: what next ?

Fig. 3.2 Flow diagram of the computer code SIMUL

The program input has been divided into the following parts:

- specification of the configuration (anti-parallel or Kirkpatrick-Baez mode);
- source characteristics (dimensions and divergences of the source);
- slit dimensions (sizes for two pairs of slits);
- geometry (positions of optical components);
- crystal characteristics (crystal parameters and curvatures);
- array resolutions (pixel size dimensions);
- number of starting rays (x100).

Fig. 3.3 shows the geometrical setup of the planes and the position of the optical components. The output of the program is in terms of maximum accepted horizontal and vertical divergence through the whole system, as well as the horizontal and vertical spot size

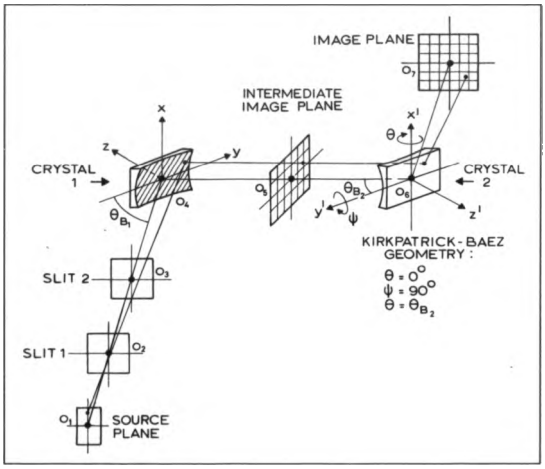

Fig. 3.3 The geometrical setup of the planes and the position of the optical components

obtained in the focal plane. Also displayed is the percentage of rays which are successively accepted by the different components and the distributions in arrays of 41x41 pixels. The limitation of the program is that the aberrations obtained are of purely geometrical origin, because it is based on geometrical optics only. The crystal is seen as a two dimensional surface, so neither depth effects nor absorption in the crystal is taken into account.

3.3.5 Beamline simulation for non, singly and doubly curved crystals

The dipole beamline 7 at the SRS, with station 7.6 at 80 m from the source, has been simulated with the ray-tracing program for a photon energy of 15 keV. A variety of optical components have been simulated as crystal monochromators, such as a planar used as a reference, singly curved surfaces like the sagittal and meridional cylinder, the elliptical and parabolic plane and the logarithmic spiral, and doubly curved surfaces like the sphere, toroid, ellipsoid, paraboloid, elliptic and parabolic cylinder. The chosen curvatures are based on a practical sagittal radius of curvature of 10 cm for Si(111)[Lan87]. According to equation 3.12 the corresponding meridional radius of curvature to avoid astigmatism is 5.74 m. For singly bent crystals the radius of curvature is specified as 10 cm or 5.74 m for sagittal and meridional bending respectively. For the spherical surface the radius of curvature is taken as 5.74 m. For the logarithmic spiral the meridional radius of curvature is 600 m, calculated according to the relation to accept the total vertical divergence of the beam with a Bragg angle of 7.57° at 80 m:

$$R_m = \frac{r_s}{sin\theta_B} \qquad (3.24)$$

Fig. 3.4 shows the flux for monochromatic 15 keV radiation as a function of horizontal slit opening for different classes of optical components, normalised on the flux of a flat Si(111) crystal at a slit opening of 1x1 mm. The figure demonstrates clearly the difference in acceptance for non or low bending and stronger bending in the meridional plane.

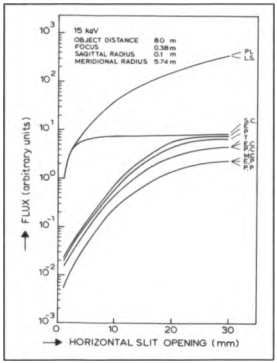

Fig. 3.4 The flux for monochromatic 15 keV radiation for different classes of optical components, normalized on the flux of a flat Si(111) crystal (see sect.3.3.3)

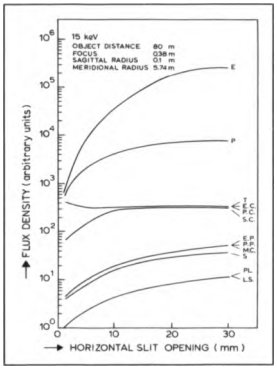

Fig. 3.5 The flux density for monochromatic 15 keV radiation for different classes of optical components, normalized on the flux density of a flat Si(111) crystal

Because of its nature the logarithmic spiral has the highest acceptance. Reflection takes place only in a small band vertically, owing to the acceptance related to the Darwin width. The low bending needed to accept the vertical divergence and the mentioned crystal acceptance is such that even a planar is a good approximation of the logarithmic spiral. This is the reason that they follow the same curve in the figure.

Fig. 3.5 gives a totally different picture. Here the flux density, i.e. the flux divided by the spotsize, is plotted as a function of horizontal slit opening. The ellipsoid has the highest flux density, owing to the better focussing properties compared to the other components. The curve of the toroid shows a slow decrease, because the contribution of the aberrations has more influence than the gain in flux for larger openings. The conclusion is that the figure demonstrates the superiority of the ellipsoid over the other components, especially for larger slit openings where geometrical aberrations become more severe. Note that the requirement of total vertical acceptance (equation 3.24) and the requirement of an astigmatic focus (equation 3.12) hold only for unit magnification. This means that the condition for total vertical acceptance and the condition for demagnification of the source cannot be fulfilled simultaneously.

3.3.6 Ray-tracing calculations

Ray-tracing calculations have been performed for the same practical situation as that described in section 3.2.3. Table 3.2 shows the outcome of the calculations in terms of horizontal and vertical acceptance through the optical system (σ_h,σ_v), the horizontal and vertical spotsizes (s_h, s_v), the ratio of the number of successful rays to the number of

	sagittal cylinder	toroid	ellipsoid
σ_v	1.9 μrad	1.9 μrad	1.9 μrad
σ_h	49 μrad	72 μrad	104 μrad
s_v	151 μm	41 μm	<0.01 μm
s_h	15 μm	20 μm	<0.01 μm
R	$303/10^6$	$105/10^6$	$179/10^6$
B	$496/10^6$	$745/10^6$	$635/10^6$

Table 3.2 Calculated results in the focal plane

starting rays (R), and the ratio of the number of rays not fulfilling the Bragg condition to the total number of started rays (B). The modified Darwin width ($\Delta\theta_m$) for a curved crystal is taken as 6.6 arcsec for 15 keV radiation (see sect. 4.4.5). The source was taken as a point source with horizontal and vertical divergence of 4 mrad and .075 mrad (15 keV) respectively and slit dimensions were 10 mm horizontally and 0.15 mm vertically.

3.3.7 Simulation and measurement of a rocking curve

In this paragraph a result is shown of a measurement on the wiggler line and the simulation of this measurement by ray-tracing. The configuration was a planar-toroid combination of Si(111) crystals in the anti-parallel mode. A rocking curve was recorded by rotating the toroid through an angle of 0.25°around the Bragg angle of 5.67°(20 keV). The object slit, located in front of the planar Si(111) crystal, was set at 10 mm horizon-

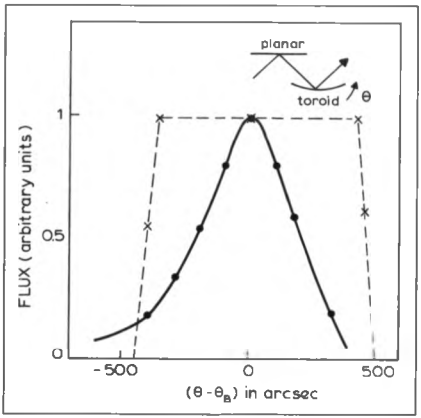

Fig. 3.6 The measured (continuous line) and ray-traced (dashed line) rocking curve for a planar-toroid combination

tally and 4.3 mm vertically. Fig. 3.6 shows the experimental and ray-traced graphs. The scale for the measured graph was relative and the position of the maximum was set to zero. The Darwin width for the planar Si(111) crystal was taken as 2.7 arcsec and for the toroidal Si(111) crystal as 7.3 arcsec, respectively (see section 4.4.5). The fwhm of the measured curve and the calculated curve turned out to be about 420 arcsec and 850 arcsec, respectively. The main reasons for the discrepancy between the measured and the calculated widths and the squareness of the calculated curve are limitations in the simulation computer code. These limitations are the assumption of a square profile of the source and the divergence, the square Bragg reflection profile (the "acceptance" cone is defined by $|\theta_B - \theta| < \Delta\theta$, with θ_B the Bragg angle, θ the angle of incidence and $\Delta\theta$ the Darwin width) and the simulation of the crystals as two dimensional geometrical shapes. However, without knowing the actual modified Darwin width ($\Delta\theta_m$) for the strong doubly bent crystal (R_s = 10 cm, R_m = 10 m) and despite the mentioned limitations the simulation of the experimental arrangement is reasonable.

3.4 Conclusions

As is described in the preceding sections the ellipsoid has the most favourable image forming qualities, with coma as the main aberration term. Despite this knowledge the first design was made and experiments were done with a toroid as the focussing device for the microprobe. The reason is that for small apertures a toroid is the best approximation to an ellipsoid, and can be produced far more easily than an ellipsoid. The next chapter deals with the design and the construction of toroidal and ellipsoidal optics. As a result the ellipsoidal optics is chosen as the heart of the microprobe for Trace Element Analysis.

Chapter 4

X-ray optics

4.1 Introduction

To construct a synchrotron X-ray microprobe a number of design criteria have to be formulated. These criteria are based on published reports, calculations of optics and information gained from initial experiments relevant to X-ray focussing and trace element analysis. This chapter deals with the design criteria for the construction of a synchrotron microprobe at the SRS (Daresbury) as well as the calculation of beam profiles and flux densities for different optical settings. The first experiments were performed at the wiggler beamline 9.4 to test toroidal crystals and in a later stage at the dipole beamline 7.6 to test ellipsoidal crystals. Calculations and simulations have therefore been done with respect to these situations.

4.2 Microprobe design criteria

In general, the essential criteria for a focussed synchrotron microprobe for trace element analysis of material of biological, organic or inorganic origin are:

- **a small spotsize** - preferably of the order of $10 \times 10\ \mu m^2$, obtained by a high demagnification factor and a minimum of aberrations of the optics and/or pinhole;
- **a high flux** - for a point measurement, about 10^{10} photons are needed to detect with sufficient statistics the majority of elements at or below the ppm level [Lan87];
- **a "high" excitation energy** - an energy which is higher than the K-binding or L-binding energy of the elements of primary analytical interest, e.g. for biological or bio-medical samples an energy between 15 - 20 keV is sufficient to detect the major essential elements; and
- **a high peak-to-background ratio** - in order to be able to detect sub-ppm levels all kinds of scattering need to be reduced.

As is described in Chapter 2 at least six methods are available to obtain microprobes. For the reasons specified in that chapter only three options will be considered for focus-

sing a beam of photons for trace element analysis: specular reflection from mirror surfaces, diffraction from multilayers, and diffraction from crystallographic planes.

Typical grazing angles for optical reflection of photons from mirror surfaces are about 1/20 of those for diffraction from crystallographic planes [Spa80a]. In the hard X-ray region (E>10 keV), necessary for trace element analysis, typical values of grazing incidence are of the order of 1 mrad. Hence, mirrors of large dimensions are required to intercept most of the available synchrotron radiation. These large dimensions make it difficult to produce an optical surface that has sufficient quality without introducing significant broadening errors or aberrations.

Multilayers are successfully used in the soft X-ray region, but in the hard X-ray region they seem at least problematic, because of the rapid decrease of difference in the refractive indices of the alternating set of higher and lower Z-layers with increasing energy above 10 keV.

Curved diffracting crystals focus sagittal rays more strongly than mirrors, because the sagittal curvature is proportional to the scattering angle, which is about 20 times larger for crystal diffraction than for specular reflection from mirrors. Moreover, mirrors cannot serve as monochromators. After considering the three options, the use of a crystal both to monochromate and to focus in the hard X-ray region appears to be the most attractive option.

4.3 "Wiggler" versus "dipole"

Historically, the first tests and experiments on curved crystals, especially toroids, were performed on the Daresbury wiggler beamline 9.4. A selected energy of 20 keV is able to detect the main essential elements in biological systems. Since the access to wiggler stations is limited by the small number of such stations available and the increasing demand for their use, it was decided, with a view to the continuity of the programme, to develop a microprobe on the dipole beamline. A lower excitation energy was chosen (15 keV) owing to the lower critical energy on the dipole beamline (see fig. 4.1). An X-ray energy of 15 keV still enables the K-lines of all the elements from Na to Rb and the L-lines up to about Bi to be excited and detected.

From theoretical calculations and ray-tracing computation it turns out that, although the flux on the dipole line for 15 keV is about a factor of 10 lower than that for 20 keV on the wiggler line, the flux density for the chosen setup on the dipole line with one focussing optical element is higher than for a two element focussing system on the wiggler beamline. On the wiggler line a two optical element focussing device is needed to protect the curved crystal from the high total incident intensity.

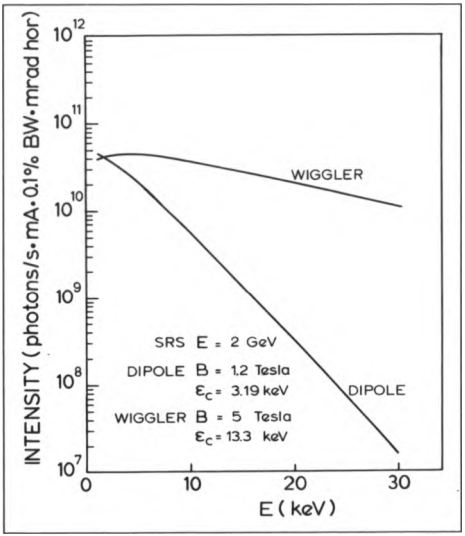

Fig. 4.1 The photon spectrum from the SRS for the dipole (beam line 7) and wiggler (beam line 9) bending magnets

4.4 Bent crystal optics

4.4.1 Introduction

The ideal geometry for focussing a point source is an ellipsoid, but for an extended source, which a synchrotron source is, no theoretical geometry exists to give a point image. However, it is evident from a theoretical point of view and from calculations presented in Chapter 3 that an ellipsoidal surface is still the best option to achieve a small focus.

Because of the long distance to the source, the small beam divergence, and the size reduction of the source to be obtained in the image, the ellipsoid is very eccentric, and therefore the easiest approximation to this geometry is a cylindrical surface, with a radius of curvature in the sagittal plane. A toroid is a better approximation to the ellipsoidal shape, and can be made using conventionally operated metal-cutting machines, such as lathes and milling machines.

Ellipsoids, however, can only be precisely produced by computer numerically controlled (CNC) machining . The reason is as follows. Any analytical surface can be locally defined by a set of sagittal and meridional radii of curvature. For a toroid this set of radii is equal for each point on the toroid surface. So both the sagittal and the meridional radii of curvature are constant for one particular dimensioned energy all over the surface. However, for an ellipsoid, defined for instance as a solid revolution of an ellipse, every two points not on the same circle have a different set of radii of curvature over the ellipsoid surface.

4.4.2 Silicon crystal material

The reason for the choice of silicon as crystal material has been the availability of high purity crystals of large dimensions from the semiconductor industry and the ability and expertise which is available to cut wafers to thin slices. These slices can be bent to a small radius of curvature. The structure factor, which is a relative measure for the monochromatic intensity, of Si(111) is high compared to other crystals [Fre88] and another advantage is that the second order reflection is forbidden, owing to the symmetry in the diamond cubic structure of silicon.

4.4.3 Toroidal optics

According to the formulae (equations 3.9, 3.11 and 3.12) presented in the previous chapter, the radius of curvature can easily be calculated for an astigmatic optical system by inserting the diffraction angle, which is 5.67° for 20 keV on Si(111) and taking the appropriate toroidal values for a_{20} and a_{02} from Appendix 3. The radius to which the crystal can be bent and the thickness of the crystal slab are closely related. A 100 μm thick Si(111) wafer can be bent to a bending radius of at least 10 cm without breaking and is still manageable during the procedure described in section 4.5 and [Lan87]. The calculated meridional radius is found to be 10 m after inserting the sagittal radius of 10 cm.

4.4.4 Ellipsoidal optics

The ellipsoidal crystal described here is intended for use on the SRS beamline 7.6 as a major element in the X-ray microprobe facility. For determining the exact equation of the ellipsoid one has to consider:

- the distance from the source at which the crystal can be placed;
- the crystal to be chosen and the planes at which reflection will take place;
- the minimum sagittal radius to which the crystal can be bent; and
- the angle of incidence, which determines the monochromated energy.

The requirement of the location of the hutch on beamline 7 has set the source-crystal distance to 80 m. Preconditions discussed in the previous sections have set the crystal and reflection planes at Si(111) with 2d = 0.627 nm, the diffracted energy 15 keV, the angle of incidence at 7.57° and the sagittal radius at 10 cm. From these data the following final expression for the ellipsoid can be derived (see fig. 4.2 and fig. 4.3, also Appendix 7 and [Lan90b]):

$$\left[\frac{X}{40.19}\right]^2 + \left[\frac{Y}{0.7289}\right]^2 + \left[\frac{Z}{0.7289}\right]^2 = 1 \qquad (4.1)$$

with the coordinates $X_0 = 39.816$, $Y_0 = 0.099$ and $Z_0 = 0$ in metres, defining the origin of the optical axis to be at the centre of the crystal. The eccentricity of the ellipsoid is

0.999835, so the ellipsoid is extremely prolate. Appendix 5 shows the design parameters and optical characteristics of the X-ray microprobe.

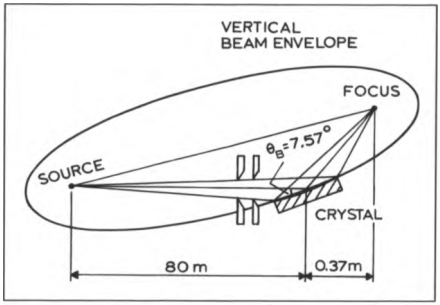

Fig. 4.2 Vertical or meridional beam envelope

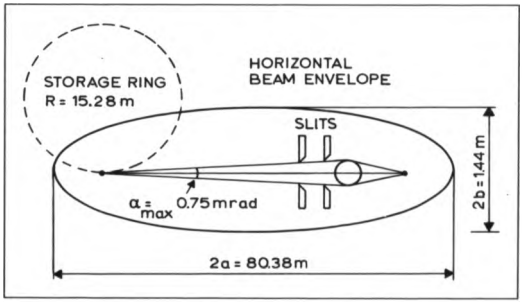

Fig. 4.3 Horizontal or sagittal beam envelope

4.4.5 Crystal bending effects

The diffraction pattern of a crystal will be affected by bending. Tail structures on the diffraction pattern will be small for the toroidal and ellipsoidal optics owing to the weak bending radius in the diffraction plane [Kui83]. The main contribution to the broadening of the rocking curve (the fwhm is called the Darwin width) is caused by the strong bending in the sagittal plane and the change in angle in the diffraction plane due to the geometrical curvature of the diffraction planes. The Darwin width ($\Delta\theta$) is not an angular physical parameter of a crystal, as is the mosaic spread, but corresponds to a smearing of the reciprocal lattice points in the direction normal to the reflection planes [Fre83]. The increase in the diffraction width due to bending is estimated with linear elasticity theory by Kuiper [Kui83] , Prins et al. [Pri84b] and Freund [Fre83] and has to be added to the dispersion relation, resulting in a modified Darwin width:

$$\Delta\theta_m = tan\theta\sqrt{\left[\left(\frac{\Delta d}{d}\right)_{flat}\right]^2 + \left[\left(\frac{\Delta d}{d}\right)_{bent}\right]^2} \qquad (4.2)$$

where $(\Delta d/d)_{flat}$ is the relative wavelength resolution obtained with a perfect crystal from a parallel white beam (symmetrical Bragg case):

$$\left(\frac{\Delta d}{d}\right)_{flat} = \left(\frac{\Delta\lambda}{\lambda}\right) = \left(\frac{\Delta E}{E}\right) = \frac{4d^2F_x}{\pi v_0} \qquad (4.3)$$

where d is the interplanar spacing of the reflecting planes (0.31355 nm for Si(111)), F_x is the Debye-Waller factor (16.7 10^{-12} cm for Si(111)) which is related to the structure factor and v_0 is the volume of the unit cell (see e.g. [Fre88]). For a flat Si(111) the relative wavelength or energy resolution in the hard X-ray region is 1.31 10^{-4}.

The relative variation in the lattice spacing due to elastic bending $(\Delta d/d)_{bent}$ is divided into two contributions, the first part comes from the change in orientation of the lattice planes with penetration depth of the beam in a bent crystal, the second part is related to contraction of the lattice planes. Parameters related to diffraction of perfect sin-

gle crystals such as silicon and germanium are tabulated by Freund [Fre88]. In Appendix 6 important physical data of silicon are listed. According to Freund the relative variation in the lattice spacing due to elastic bending for a meridional curved crystal is:

$$\left(\frac{\Delta d}{d}\right)_{bent} = \frac{(cot^2\theta - \nu)\,t}{R_m} \tag{4.4}$$

where ν is Poisson's ratio, t is the crystal thickness and R_m is the meridional radius of curvature. Equation 4.4 can be expanded to both meridional and sagittal curvatures simultaneously:

$$\left(\frac{\Delta d}{d}\right)_{bent} = \left[\frac{cot^2\theta}{R_m} - \frac{\nu}{R_{eff}}\right]t \tag{4.5}$$

where R_{eff} is the effective radius of curvature defined as:

$$\frac{1}{R_{eff}} = \frac{1}{R_m} + \frac{1}{R_s} \tag{4.6}$$

where R_s is the sagittal radius of curvature.

For thick crystals the quantity t in equation 4.4 and 4.5 must be replaced by the penetration depth which is determined by both absorption and diffraction (extinction) processes. Analogous to Suortti et al. [Suo86] the maximum number of simultaneously reflecting planes (N_π) of a bent perfect crystal can be calculated according to:

$$N_\pi = \frac{2R_{eff}}{\pi l_{ext}}\left[\frac{sin\theta}{cos^2\theta - \nu sin^2\theta}\right] \tag{4.7}$$

where l_{ext} is the extinction length defined as:

$$l_{ext} = \frac{v_0}{F_x \lambda} \tag{4.8}$$

where λ is the exciting wavelength defined by equation 3.19. Extinction is the limiting factor if the number of simultaneous reflecting planes due to bending (N_g) is larger than the number of simultaneous reflecting planes due to extinction (N_e):

$$N_e = \frac{2l_{ext}\sin\theta}{\pi d} \tag{4.9}$$

Photo-electric absorption and inelastic scattering is the other limiting factor which has to be considered, and the corresponding number of simultaneous reflecting planes due to absorption (N_a) is:

$$N_a = \frac{\sin\theta}{\mu_0 d} \tag{4.10}$$

where μ_0 is the linear attenuation coefficient.

As an example: take a doubly curved Si(111) crystal locally defined by a sagittal radius of curvature R_s = 0.1 m and a meridional radius of curvature R_m = 5.74 m. The thickness of the crystal is 100 μm and further conditions are as given in section 3.2.3. Then the number of simultaneous reflecting planes due to bending, extinction and absorption can be calculated and are found to be $N_g = 7.3\ 10^2$, $N_e = 3.1\ 10^3$ and $N_a = 1.8\ 10^5$, respectively. Now with $N_g < N_e$, the beam can penetrate to the next layer and be reflected when the direction of the incidence changes by $\Delta\theta$. Subsequently, deeper and deeper layers become effective, the rocking curve broadens, and the integrated reflectivity is limited by absorption. This means that the crystal thickness (t) in eq. 4.5 has to be replaced by the absorption thickness (t_{abs}), which is:

$$t_{abs} = \frac{\sin\theta}{2\mu_0} = (28.6\mu m) \tag{4.11}$$

Note that N_a is related to a thickness where the intensity inside the crystal has dropped 1/e, whereas t_{abs} is the thickness related to the decrease in intensity of 1/e at the surface after reflection.

4.5 The construction of focussing crystals

The focussing crystals were made by bending a 100 μm thick (111)-oriented silicon wafer with a diameter of 50 mm into a circular mould of aluminium. This thickness has been chosen because (a) it can be bent down to a radius of 10 cm and (b) it is still manageable during the procedure mentioned below. The crystals were attached to the moulds at a temperature of 165° C under air pressure of 8 bar using an oxidized polyethylene foil as adhesive. A mould with a diameter of 60 mm was given a concave toroidal shape at its surface with principal radii of 10 cm and 10 m. A photograph of the focussing crystal is shown in fig. 4.4. The shape accuracy of the crystal in the sagittal and meridional plane, see respectively fig. 4.5 and fig. 4.6, was measured with a stilus machine. The shape accuracy is plotted relative to a circle constructed through the data points. The fitted sagittal and meridional radii of curvature were found to be 99.9 mm and 9825.7 mm, respectively. The overall shape accuracy of the toroid amounts to 11 μm over a distance of 45 mm. Non-highly-symmetrical moulds like ellipsoids cannot be produced with the desired shape accuracy and low surface roughness in a conventional way. So precision machining technology, i.e. single point diamond cutting on a computerised numerically controlled (CNC) machine, has been used to make a concave ellipsoidal mould, defined analytically in section 4.4.4. Fig. 4.7 and fig. 4.8 show respectively the deviations of the curvature of the mould and of the focussing crystal in the sagittal plane.

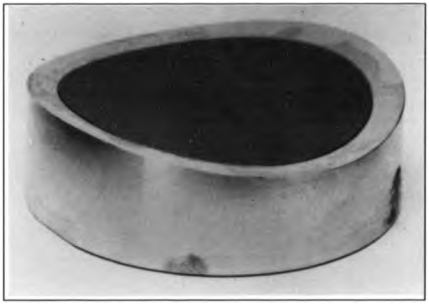

Fig. 4.4 The focussing crystal (60 mm in diameter)

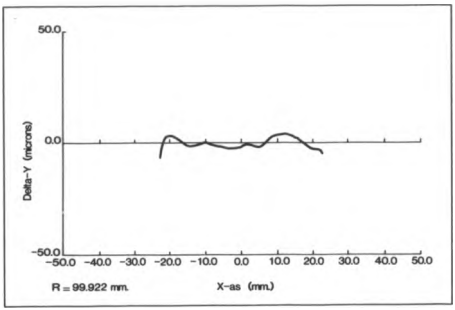

Fig. 4.5 Local deviations of the surface of the toroidal crystal from the average circular curvature, measured through the centre of the crystal (set at X=0) in the sagittal plane

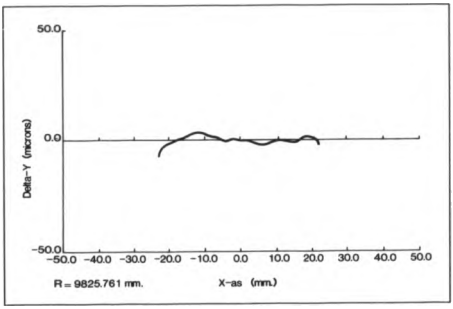

Fig. 4.6 Local deviations of the surface of the toroidal crystal from the average circular curvature, measured through the centre of the crystal (set at X=0) in the meridional plane

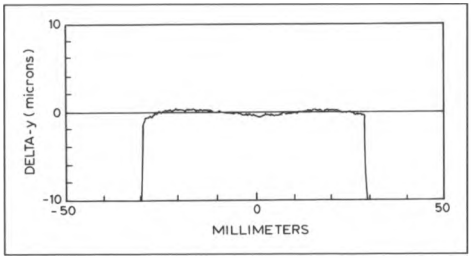

Fig. 4.7 Local deviations of the surface of the ellipsoidal mould from the circular curvature, measured through the centre (set at X=0) in the sagittal plane

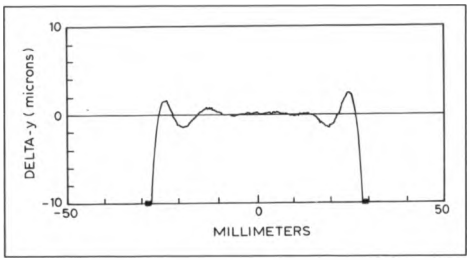

Fig. 4.8 Local deviations of the surface of the ellipsoidal mould with the Si crystal on top of it

4.6 Ray-tracing calculations for toroidal and ellipsoidal optics

4.6.1 Determination of crystal and image topograms

In order to design the microprobe optics, ray-tracing calculations have been performed to simulate beamlines with slits and crystal optics. Fig. 4.9 and fig. 4.10 show respectively the crystal topogram and the image topogram for the curvatures (R_s = 10 cm and R_m = 1000 cm) of the toroid corresponding to a Bragg angle of 20 keV. Fig. 4.9

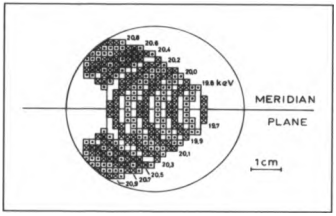

Fig. 4.9 Calculated topogram of the toroidal crystal area for the energy range from 19 to 25 keV, indicating the positions where X-rays are reflected with their energies in keV

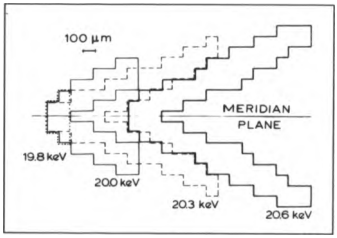

Fig. 4.10 Part of the calculated image topogram of different reflected energies (keV) in the spot for the toroidal crystal

shows a topview of the crystal area, with the incident white beam coming from the left. The calculated topogram of the crystal area for the energy range 19 to 25 keV indicates the positions on the crystal surface (in dots or crosses arbitrarily) where X-rays are Bragg diffracted with their corresponding energies (in steps of 100 eV) for maximum slit opening to irradiate the whole crystal area. The calculated image topogram (fig. 4.10) shows the spotsize in the focal plane for the different diffracted energies, with a resolution of $100 \times 100\ \mu m^2$.

Fig. 4.11 and fig. 4.12 display respectively the calculated vertical and horizontal beamprofiles for an actual slit setting (10 mm horizontally and 4.3 mm vertically). The horizontal and vertical integrated flux distributions are 250 μm and 150 μm fwhm respectively. Based on the wiggler beam line data a flux density of about 850 photons/$(s.mA.\mu m^2)$ at a spot of $70 \times 70\ \mu m^2$ is calculated. The calculated horizontal and vertical spot size reductions are 40 and 30 respectively and the source size reductions are 50 and 4.5.

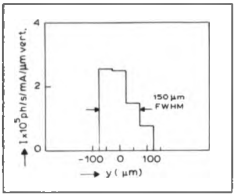

Fig. 4.11 Calculated vertical beam profile for the toroidal crystal

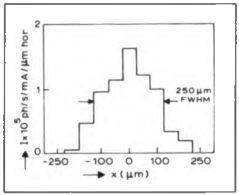

Fig. 4.12 Calculated horizontal beam profile for the toroidal crystal

Calculations for the ellipsoid are displayed in figs. 4.13 and 4.14, which respectively show the crystal topogram for 15 keV and the image topogram in the focal plane for a horizontal slit opening of 50 mm and a vertical slit opening of 3 mm. Fig. 4.13 is a similar picture to fig. 4.9. Both show a topview of the crystal indicating the areas fulfilling

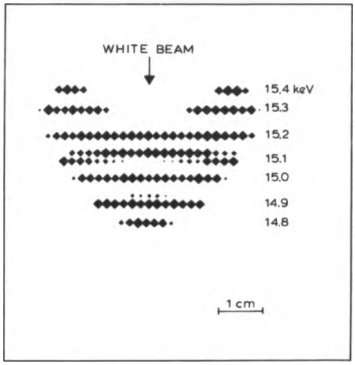

Fig. 4.13 Ray-traced reflection topogram of the ellipsoidally curved crystal

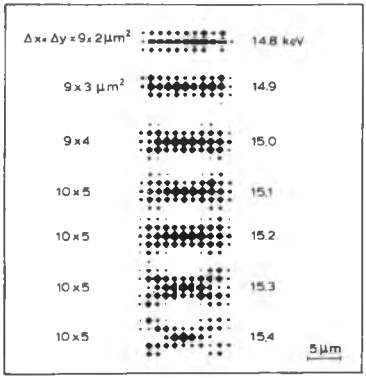

Fig. 4.14 Ray-traced reflection topogram in the focal plane

the Bragg condition. The area of the squares in the topograms are proportional to the flux. Comparison of these topograms immediately shows the difference in reflecting behaviour for the toroid and ellipsoid, respectively. In the case of the ellipsoidal crystal, the area where a particular energy reflects follows a straight line. This is in contrast to the toroidal crystal, where the areas follow curved lines. This is also the reason that a toroidal shape introduces more aberrations than an ellipsoid. Only for smaller openings of the aperture (horizontal or sagittal slit size) is the toroid a good approximation to an ellipsoid.

In fig. 4.14 the spot size is plotted as function of energy in steps of 100 eV. For the final evaluation of the spot size these images have to be superimposed. This is shown in fig. 4.15. Note that the centre of each image in fig. 4.14 is also the centre of the integrated image in fig. 4.15. Here the superimposed or composite 2D-plot of the intensity distribution in the focal plane for the diffracted energy range from 14.8 to 15.4 keV is plotted with a maximum horizontal size of 10 μm and a maximum vertical size of 5 μm. The pixel size in the 2D-plot is 0.25×0.25 μm^2. The maximum intensity in the central pixel (0.25×0.25 μm^2) is 2.10^5 ph/(s.mA. 0.25×0.25 μm^2).

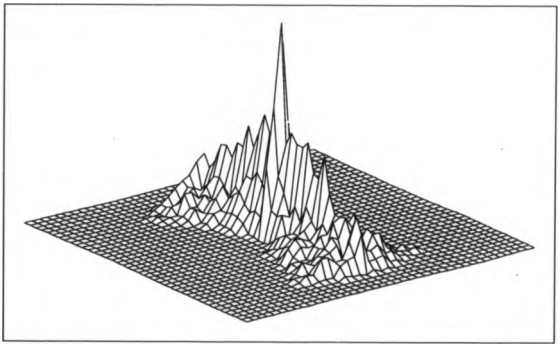

Fig. 4.15 A two dimensional intensity distribution in the focal plane in the energy range of 14.8 to 15.4 keV, with a maximum contour of 10×5 μm^2. The maximum intensity is 2.10^5 ph/(s.mA. 0.25×0.25 μm^2).

4.6.2 Determination of intensities

To determine the intensity of the spot in the focal plane, the following parameters or quantities must be known or calculated: the horizontal (α_h) and vertical (α_v) divergence accepted by the optics; the vertical divergence of the source (σ_v); the diffracted energy (E) and energy bandwidth (ΔE) passed by the optics; the horizontal (H) and vertical (V) dimensions of the spot in the focal plane; and the efficiencies (R) with which the optical component reflects or diffracts the incident radiation within the bandpass, including an absorption factor for the beam line and windows. With these parameters the flux density (F) of the spot in the focal plane can be written as:

$$F = \frac{I_0 \cdot \alpha_h \cdot \alpha_v \cdot \frac{1}{\sigma_v} \cdot \frac{\Delta E}{E} \cdot R}{H \cdot V} \qquad (4.12)$$

where I_0 is the intensity of the synchrotron source and is given in fig. 4.1. The calculated flux in the spot for the ellipsoidal crystal is about 10^7 ph/(s.mA), with a spotsize of 10×5 μm^2 which means a flux density of 2.10^5 ph/(s.mA.μm^2). The eq. 4.12 is used to calculate the flux densities, in the case of ray-tracing R is only taken as the ratio of the number of successes and the number of started rays.

4.7 Characterisation using white radiation topography

Although the image in the focal plane strongly depends on the shape accuracy of the curved shape, it also depends on the orientation of the Bragg-planes at which diffraction takes place. So an extra source of aberrations arises, when the Bragg-planes are not parallel to the surface of the mould.

A quantitative, in-situ method of judging the orientation and the quality of crystal reflection is making topographs with white radiation reflection geometry [Mil80]. A sheet of Agfa-Gevaert type D2 film was positioned and levelled 1cm above the crystal. Fig. 4.16 shows the result of exposing the ellipsoidal crystal for 1s, while the electron beam current was ~200 mA and the slit opening 1×1 mm^2. Note that the incident beam direction enters at the bottom of the photograph and the (111) reflection is the central spot on the axis of symmetry.

The symmetry of the individual spots and of the whole pattern in the meridional plane (direction top-bottom) is striking and is indicative of the precision of forming. Repeating the same procedure for larger slit areas yields topographs with larger spots, corresponding to larger reflection areas in the crystal. When one of the spots is observed in more detail, fig. 4.17 for a toroidal and fig. 4.18 for an ellipsoidal reflection using a slit opening of 10 mm horizontally and 2 mm vertically in both cases, an uniform blackening is seen in case of the ellipsoidal crystal.This is an indication of a minor number or absence of dislocations in the ellipsoidal crystal, probably due to the better surface quality compared to the toroidal crystal. Also, virtually no slipbands were observed for the ellipsoidal crystal in contrast to the toroidal crystal. Slipbands are typically induced by severe bending of a crystal in the plastic regime.

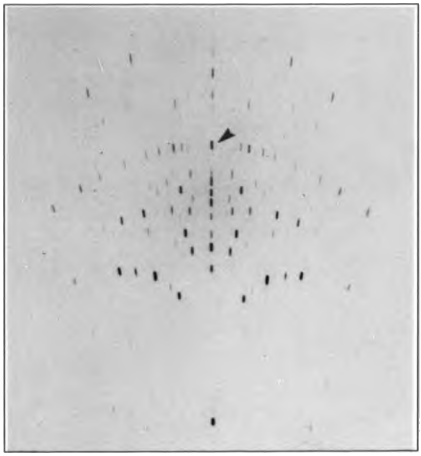

Fig. 4.16 White radiation reflection topograph of the ellipsoidal crystal, where the arrow indicates the (111) reflection and the beam direction is from below

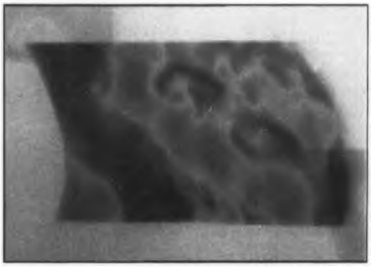

Fig. 4.17 Detail of a white radiation reflection topograph of the toroidal crystal

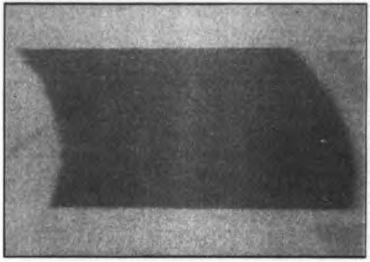

Fig. 4.18 Detail of a white radiation reflection topograph of the ellipsoidal crystal

Chapter 5

The Daresbury photon microprobe

5.1 Introduction

This chapter deals with the experimental results obtained by the use of focussing crystals. The results presented consist of X-ray optical results, such as beam profiles and flux densities to demonstrate the focussing action of the bent crystals, as well as results to show the analytical capabilities of the microprobe. Concerning the analytical features, comparisons are made between PIXE and SXRF. The experiments were carried out during the period 1986-90 at the Daresbury Synchrotron Radiation Source Laboratory. Toroidal crystals, for the characteristic parameters see the previous chapter, were dimensioned for the use on the wiggler beamline and after the installation of the HBL (High Brightness Lattice) ellipsoidal crystals were dimensioned for the dipole beamline. Fig. 5.1 shows the schematic layout of the Daresbury storage ring with the different beamlines.

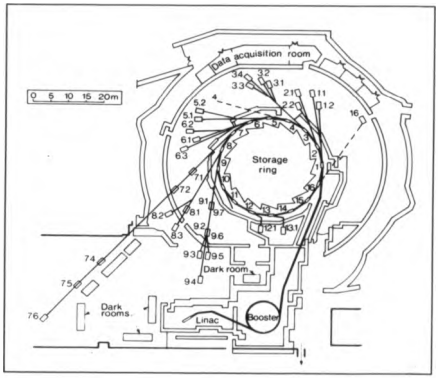

Fig. 5.1 Schematic layout of the Daresbury storage ring

5.2 Description of the experimental setup

5.2.1 Description of the experimental setup on the wiggler beamline

5.2.1.1 Synchrotron operation

The performance of the toroidal crystal, see section 4.4 and 4.5 for the characteristics of the toroid, was measured at station 9.4 of the wiggler beamline. The energy of the electrons in the ring was 2 GeV, the current typically 100 mA and the magnetic field of the wiggler was 5T during most of the experiments. Fig. 5.2 shows the schematic layout of beamline 9 and the experimental setup at station 9.4.

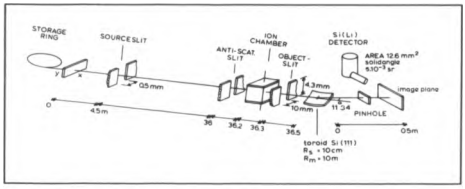

Fig. 5.2 Schematic layout of the wiggler beamline 9

5.2.1.2 Crystal and slit operation

The doubly bent Si(111) crystal was placed 36.5 m from the source, where it accepts 1.4 mrad of the horizontal divergence, to select and focus a narrow portion of the continuous spectrum of the order of several 100 eV, see also section 4.6.1. A so called horizontal source slit placed 4.5 m from the source is used for controlling the total flux. Low flux is used for exposing films to check the alignment, and high flux for beam profiles and measurements. Two other pairs of horizontal and vertical slits are placed 36 m and 36.3 m from the source. The object slit, placed at 36.3 m, is used to control the irradiated area of the crystal. The other pair of slits functions as an antiscattering device for

the object slit and was optimized by reducing the slit opening until it affected dramatically the intensity measured with an ionization chamber. The crystal rotation in the meridional plane is stepping motor controlled.

5.2.1.3 Sample holder and detection system

Samples were placed at the focus mounted on a motor controlled XY-stage, which is 0.5 m from the crystal, at twice the Bragg angle with respect to the incoming beam ($2\theta = 11.34°$, the energy used being 20 keV). A Si(Li) detector, crystal area 12.6 mm^2, was aligned at 90° with respect to the incident beam. The solid angle subtended by the detector was about $5\ 10^{-3}$ sr. A cross wire, one wire of tungsten and the other of copper, each with a diameter of 50 μm, was used for finding the most intense spot in the beam. For measuring beam profiles a composite target was used. This consisted of two plates, one of molybdenum and one of nickel, both 100 μm thick, with square profile sides in contact, which was scanned across the focal plane. To measure flux densities a nickel foil, 100 μm thick, and a 0.1 μm gold foil evaporated on to a 25 μm kapton foil were used. The setup comprised two sets of pinholes with circular holes to define the irradiated area. One set, used for precollimation, had diameters of 1 mm and 0.2 mm and was made in stacked plates of lead, iron, aluminium and carbon, being 2 mm,1 mm,1 mm and 1 mm thick respectively. The holes were produced by drilling. Pinholes of this kind were located about 5 - 10 cm in front of the sample.The other set had diameters of 1.1 mm, 0.47 mm, 0.17 mm and 0.08 mm and was made in a stack of molybdenum, stainless steel, and aluminium, 100 μm, 250 μm and 300 μm thick respectively. The holes were produced by the spark technique. These pinholes were located between the precollimator and the sample. The crystal and the pinhole-sample combination were put in air.

5.2.2 Description of the experimental setup on the dipole beamline

5.2.2.1 Synchrotron operation

The performance of the ellipsoidal crystal was measured at station 7.6 of the dipole beamline. The synchrotron was operated at 2 GeV with a maximum and a typical stored electron current of 300 mA and 200 mA respectively with lifetimes better than 20

hours. Fig. 5.3 shows the schematic layout of the beamline 7 and the experimental setup at station 7.6, which is located 80 m from the source.

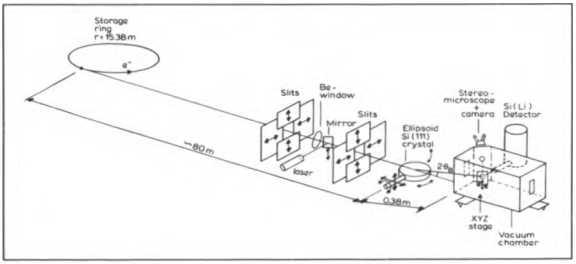

Fig. 5.3 Schematic layout of the dipole beamline 7

5.2.2.2 Crystal and slit operation

The synchrotron beam enters the hutch via a 0.5 mm thick beryllium window about 60 cm upstream from the crystal. Two pairs of horizontal and vertical slits are placed 78.5 m and 79.7 m from the source. The first pair defines the beam envelope, see fig. 4.2, and determines the irradiated area of the crystal. The minimum opening horizontally and vertically to irradiate the whole crystal is 60×8 mm^2. The other pair of slits functions as an antiscattering device.

The ellipsoidally shaped Si(111) crystal, with a local sagittal radius of curvature of 100 mm and a local meridional radius of 5.74 m, accepts maximally 0.75 mrad of the horizontal divergence, to select and focus a small part of the continuous spectrum of the order of 100 eV, see section 4.6.1.

The crystal is mounted on a Huber goniometer head. This stage, which has two independent motorized translations and rotations, is mounted on the axis of a computer-controlled goniometer, which sets the Bragg angle with a resolution better than an arcsec.

To match the ellipsoidal crystal with the geometry of the beamline and Bragg angle, five independent motions can be set by motors as indicated in fig. 5.3.

5.2.2.3 Target chamber and detection system

The design of the vacuum chamber is based on multipurpose use. Its dimensions ($0.5 \times 0.4 \times 0.3$ m^3) are chosen in such a way that the front part is used for microanalysis and the other part can be used for routine analysis. For routine analysis a multi sample rotation stage has been developed by Lenglet [Len88]. For microanalysis an XYZ-stage for positioning the sample has been developed, see below. The vacuum chamber is made out of aluminium and the wall thickness is 12 mm. In the bottom of the chamber tapped holes are put for mounting. The focussed beam enters the vacuum chamber through a 7.5 μm thick kapton window. In the vacuum chamber a collimator, with 10 mm diameter, is placed to shield sample and detector from unwanted reflections or diffraction lines from

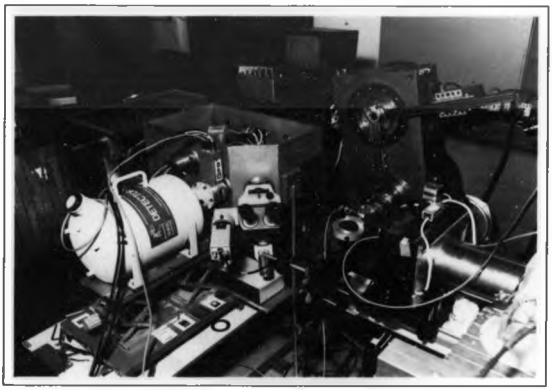

Fig. 5.4 Photograph of the experimental setup on station 7.6

the crystal. The vacuum chamber can be positioned by a three-point kinematic mounting on a base plate clamped to the optical bench which is integral to the 7.6 setup. Samples were placed at the focus, which is 0.38 m from the crystal, at twice the Bragg angle with respect to the incoming white beam ($2\theta = 15.14°$, the energy used being 15 keV). The samples are mounted at 45° to the (focussed) beam on a linear-bearing XYZ-stage driven by Sanyo-Denki stepper motors with 25 mm of travel in all directions. The stages have 1.25 µm stepsize. The sample is observed with a Zeiss SV8 stereo (zoom) microscope with 175 mm working distance, equipped with a Sony CCD camera. The microscope is positioned at 45° with respect to the incident beam (i.e. perpendicular to the sample) and outside the vacuum chamber so that samples can be observed through a perspex window in the vacuum chamber. Samples can be illuminated by two goose-neck self-sustaining glass-fibre light conductors from a 100 W Euromex cold light illuminator. A photograph of the setup is shown in fig. 5.4.

A Si(Li) detector with 50 mm^2 crystal area was aligned at 90° with respect to the incident beam. The solid angle subtended by the detector was about 4 10^{-2} sr. The periphery of the detector was shielded by sandwich materials (Pb-Fe-Al-C) to reduce background radiation due to scattering. For measuring beam profiles and flux densities the following samples were used: a titanium target with 10 µm thickness and razor blade edge, a copper grid (as used in electron microscopy), a 100 nm gold foil evaporated onto a 25 µm kapton foil and 60 µm Araldite doped with known concentrations of zinc.

5.2.2.4 Alignment procedure

The alignment and focussing of the crystal and positioning of the beamspot on the sample were achieved by putting a ZnS (Ag-activated) fluorescent screen on the sample position and viewing the focussed beam on a monitor, while adjusting the crystal. The image on the monitor is obtained using the fixed microscope. Optimum setting can be reached by minimizing the aberrations. Most crucial is to position the centre of the crystal on line with the axis of rotation (setting the Bragg angle). A mismatch of about 1 mm resulted in multiple meridional spots in the focal plane. The most important reduction of aberrations is obtained by a sagittal rotation of the crystal so that the meridional crystal plane is matched to the beam direction which is tangential to the synchrotron ring.

5.3 X-ray optical results

5.3.1 X-ray optical results on the wiggler beamline

5.3.1.1 Determination of beam profiles

The experimental beam profiles given in fig. 5.5 and 5.6 were measured by moving the 100 μm molybdenum razor blade edge through the focus in steps of 50 μm. The shape of these curves is in agreement with the calculated beamprofiles of fig. 4.11 and 4.12. The horizontal beam profile is symmetric in both cases, as expected, since the optical path from the source to the image is symmetric in the sagittal plane, in contrast to the meridional plane where the optical path is asymmetric. The fwhm of the measured beam profile is determined from fig. 5.5 and fig. 5.6 and is found to be 380 μm vertically and 200 μm horizontally, with the object slits set at 4.3 and 10 mm respectively. Hence the vertical reduction of the source size is 11 and the horizontal reduction is 50. The measured and calculated horizontal fwhm as well as the source size reductions are in good agreement. Both measured beam profiles have an uncertainty of 50 μm. The measured vertical fwhm seems to be too high and thus the vertical source size reduction too low as compared to the theoretical value. It is assumed that it is due to the higher energy reflections at the aluminium crystal backing, which will broaden the spot in the diffraction plane. An increase in intensity in the energy region 20 - 25 keV was found which corresponds to a Bragg diffracted energy from polycrystalline aluminium. This was confirmed by measurements using a similar focussing crystal mounted on a glass substrate, which show no high energy components in the spectra.

5.3.1.2 Determination of intensities

Flux densities were measured on the gold- and nickel-target. A circular pinhole of 80 μm diameter was used to define the beam size and was positioned about 5 mm in front of the sample. The measured flux density was about 200 photons/(s.mA.μm^2). This was not the maximum obtainable, since the source slit was not fully opened to prevent the crystal from high exposures. Fig. 5.7 shows a spectrum obtained from the gold foil.

When the object slit is opened more than about 15 mm there is no substantial increase of the flux in the central region of the spot. This agrees with fig. 4.9 and fig. 4.10,

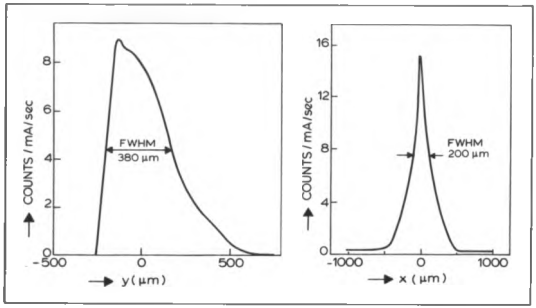

Fig. 5.5 and 5.6 Measured vertical and horizontal beam profile

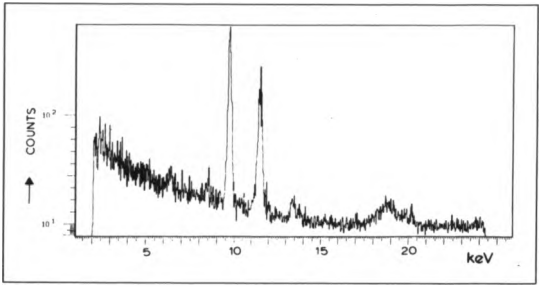

Fig 5.7 Fluorescence spectrum of 100 nm gold, obtained in 302 s with a pinhole of 80 µm diameter. The beam current was 273 mA, the object slit dimensions 4.3 × 5 mm^2, and the distance between target and detector 50 mm.

which show that the energies reflecting (E>20 keV) from more than 7.5 mm off axis hardly give any contribution to the central region of the spot in the focal plane. Thus these energies give rise to strong (chromatic) aberrations. It means that only one quarter of the horizontal divergence can effectively be accepted. Though flux measurements with a flat Si(111) crystal show that the increase of the flux density with the doubly bent crystal is about a factor 300, it is still lower than the predicted value by a factor of about 4. The predicted value may be too optimistic, because the computer program, as mentioned (see sec. 4.6.1.), does not take reflection efficiency and absorption into account.

5.3.1.3 Determination of concentrations

The flux density needed in practice for trace element analysis is an important feature. To obtain an estimate, assume 1 ppm of zinc in an organic matrix. The detection volume is assumed to consist of a cube with side x, where x is between 10 μm and 100 μm. Furthermore a minimum signal of 1 count/s is assumed and synchrotron operating conditions of 2 GeV electron energy and 150 mA of electron current. Values of ioniza-

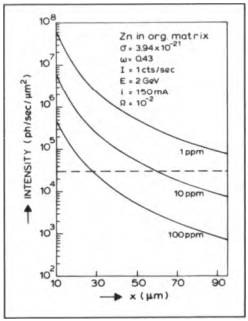

Fig. 5.8 Number of photons needed to detect 1,10 or 100 ppm of zinc in an organic matrix of a cubic detection volume with side x in μm to meet the signal detection criterium of 1 count/sec. The dashed curve gives the available intensity.

tion cross-sections (σ) in barn/at, fluorescence yield (ω) in relative units and solid angle (Ω) in relative units (see eq. 5.20) subtended by the detector are taken and are listed in fig. 5.8. The rate of background radiation for an organic matrix in the energy range of Zn K_α was between 1 and 10 counts/s. Possible sources of background radiation are diffraction at the aluminium backing of the focussing crystal, multiple scattering of high energies up to 100 keV, higher order reflections from the crystal and scattering of the focussed radiation in air. In fig. 5.8 the required flux is given as a function of the size of the cube for three values of the zinc concentration. The dashed curve in fig. 5.8 gives the available intensity based on the measured flux density of 200 photons/(s.mA.μm^2), assuming the flux density to be constant across the focussed beam in the range from 10 × 10 to 100 × 100 μm^2. The actual curve will be higher in the region of small cube sizes and lower for large cube sizes. The figure shows, that the required detection volume to meet the mentioned 1 count/s criterion is at least 60 × 60 × 60 μm^3 or 28 × 28 × 28 μm^3 for detecting 10 or 100 ppm of zinc respectively. The concentration that can be detected assuming a typical spatial resolution can also be derived from fig. 5.8.

5.3.1.4 Crystal radiation damage

During the measurements it was found that a beam current in excess of 100 mA lead to blistering of the crystal when polyethylene was used as adhesive. It is observed that the blisters are not formed in the centre of the irradiated area of the crystal, but just at the edges, where the adhesive is under tensile stress. No damage of the crystal was found when epoxy resin was used instead of polyethylene. Then, however, thickness variations of the adhesive layer caused serious broadening of the spot and a decrease of flux density by a factor of 4.

5.3.2 X-ray optical results on the dipole beamline

5.3.2.1 Determination of beam profiles

The experimental horizontal beam profile for the ellipsoidal crystal, given in fig. 5.9, was measured by moving the 100 nm gold foil with the sharp edge through the focus in steps of 1.25 µm. Note that in the graph the horizontal axis is corrected for the 45°

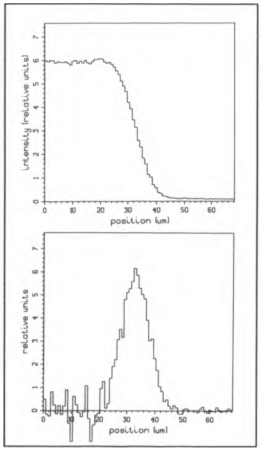

Fig. 5.9 Horizontal beam profile

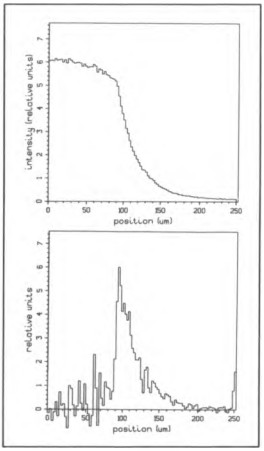

Fig. 5.10 Vertical beam profile

alignment of the sample to the beam so that one step is 0.88 μm. The fwhm of the beam profile is found to be 10 μm sagitally, which is in agreement with the calculated value of 10 μm. The irradiated area of the crystal was determined by a slit opening of 10×3 mm^2 and no further collimation was used. The experimental vertical beam profile, given in fig. 5.10, was measured by moving through the focus in steps of 2.5 μm. Using the ellipsoidally bent Si(111) crystal a minimum spotsize of 10×15 μm^2 (fwhm) is obtained. This corresponds to a demagnification of the source by a factor of 200 horizontally and 20 vertically or to a spot size reduction of the unfocussed beam at 80 m from the source by a factor of 1000 horizontally and 20 vertically. The demagnification factors show the stronger reduction in the horizontal or sagittal plane.

Fig. 5.11 shows the convergence of the beam at the focus. The measured horizontal beam envelope is displayed as a function of z (i.e. positive z is downstream from the crystal) and z = 0 is the measured position of the focus. The dashed curve is the calculated horizontal beam envelope for 15 keV radiation. The measured beam size is expressed in fwhm, in contrast to the calculated beam size which is in full size.

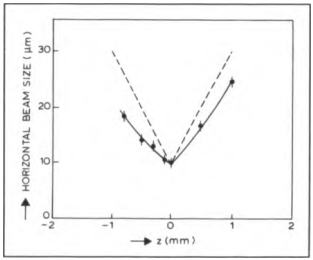

Fig. 5.11 Calculated (dashed line) and measured (solid line) horizontal beam envelope

5.3.2.2 Determination of intensities

Fluxes were measured on the gold foil and the zinc-doped Araldite. Analysis of both targets gave flux densities of about 10^4 ph/(s.mA.μm^2). In this case only 13 × 13 × 13 μm^3 is required to detect 10 ppm Zn (see fig. 5.8 and section 5.3.1.3). The ionization cross-section for 15 keV is taken as 8680 barn. The calculated or theoretical flux density is 5.10^4 ph/(s.mA.μm^2) for a 10 mm horizontal and 3 mm vertical slit opening respectively. The discrepancy between theory and experiment concerning the determination and the measurement of fluxes and flux densities is due to the incompleteness of the model. The model considers the crystal as a geometrical shape with an increased acceptance (modified Darwin width) due to bending, however no efficiencies, no depth effects and absorption effects in the crystal are taken into account.

Fig. 5.12 and fig. 5.13 show graphs for two out of a series of five measurements,

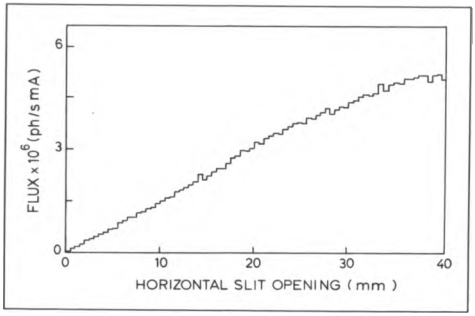

Fig. 5.12 Flux as a function of horizontal slit opening (1 mm fixed vertical opening)

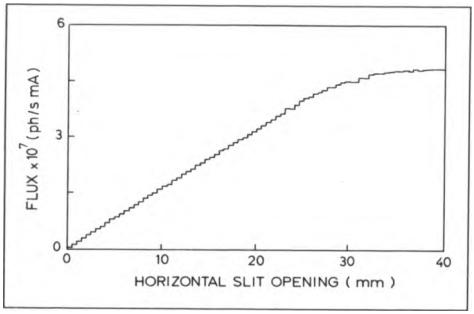

Fig. 5.13 Flux as a function of horizontal slit opening (5 mm fixed vertical opening)

in which the vertical slit opening is fixed in each measurement and increased in steps of 1 mm from 1 mm to 5 mm. The flux is seen as a function of horizontal slit opening. The conclusion is that over the whole range of slit settings the flux increase is linear, which is expected in case of an ellipsoid. The range of linearity is precisely the region in fig. 4.7 where the shape accuracy is better than 1 μm. Thus the edges of the ellipsoidal crystal where the shape accuracy is relatively bad (>1 μm) do not contribute linearly to the flux. Inspection of the horizontal beam profiles shows no significant enlargement of the spot at different slit settings.

5.4 X-ray analytical results

5.4.1 Introduction

The analytical capabilities of the microprobe can be described by the evaluation of the relative and absolute minimum detection limits and sensitivities, respectively. These parameters cannot be determined in general terms because they depend strongly on matrix composition and related background production, on geometry and solid angle of the X-ray detector system and, on excitation energy and flux. So detection limits and sensitivities have been determined for biological samples such as standard reference materials as well as artificially produced standards, imitating biological material. Trace element concentrations can be deduced from experimental calibration functions or theoretically from K or L-shell ionization cross-sections. In the latter case, coherent and incoherent scattered radiation serve as internal standards. Both methods are demonstrated.

5.4.2 Theoretical calculations of cross-sections and intensities

One of the important advantages of XRF and SXRF for the detection of trace elements is the ability to provide absolute concentration values. In conventional XRF the scattered coherent and incoherent X-rays of the primary beam are commonly used as a reference in the analysis of various kinds of samples [Kub79, And58]. Scattered X-rays have been used to normalize X-ray fluorescent intensities, which might reduce systematic errors and errors introduced by intrinsic sample variations [Cul62, Fel75]. If all the experimental parameters are known the concentrations can be calculated. Assuming a

linear dependence of the intensity of the scattered radiation on the thickness of the sample and when only first order scattering processes have to be considered (the contribution of multiple scattering in case of low-Z samples of thickness (t<100 μm) can be neglected [Fel75,Cho86]) then the number of scattered or characteristic X-rays (I_x) produced in a volume element dV in cm^3 of the sample with density ρ (g/cm^3) and detected in a surface element $d\Omega$ of the detector expressed in sterad (sr) can in general be written as:

$$I_x = N_{ph} \frac{d\sigma_x}{d\Omega} A_i A_o \rho d V \varepsilon_x d\Omega dE_i \tag{5.1}$$

where $N_{ph}dE_i$ is the number of incoming photons per cm^2 within the energy interval dE_i. The differential cross-section $d\sigma_x/d\Omega$ (barn/sr.g) is for either the production of scattered radiation or the production of characteristic X-rays. The absorption coefficients of the incoming and outgoing photons A_i and A_o respectively, e.g. described by van Espen [Esp79], reduce in our experimental set-up to:

$$A_i A_o = \left[\frac{1 - \exp\left(-\left(\frac{\mu}{\rho}(E_i) + \frac{\mu}{\rho}(E_o)\right) \rho d \sqrt{2}\right)}{\left(\frac{\mu}{\rho}(E_i) + \frac{\mu}{\rho}(E_o)\right) \rho d \sqrt{2}} \right] \tag{5.2}$$

where $\mu/\rho(E_i)$ and $\mu/\rho(E_o)$ are the mass absorption coefficients for the impinging and emerging characteristic beam respectively in (cm^2/g) and ρ.d is the sample thickness in (g/cm^2). The detector efficiency is ε_x.

In the same way as the mass absorption coefficient the incoherent and coherent mass scattering coefficient can be defined as:

$$\frac{\mu_s}{\rho} = \int \frac{d\sigma}{d\Omega} \cdot d\Omega \tag{5.3}$$

with

$$\frac{d\sigma_{incoh}}{d\Omega} = \frac{N_0}{A} \cdot S(x, Z) \cdot \frac{d\sigma_C}{d\Omega} \tag{5.4}$$

or

$$\frac{d\sigma_{coh}}{d\Omega} = \frac{N_0}{A} \cdot F^2(x, Z) \cdot \frac{d\sigma_R}{d\Omega} \tag{5.5}$$

where $d\sigma_{incoh}/d\Omega$ and $d\sigma_{coh}/d\Omega$ are the incoherent and coherent differential scattering cross-section respectively in cm^2/g, N_0 is Avogadro's number, S(x,Z) is the incoherent scattering function, x is $(E_i/12.3985)\sin(\theta/2)$, θ is the scattering angle, E_i is the incident photon energy in keV, Z is the atomic number of the scatterer, $d\sigma_C/d\Omega$ is the free electron (Compton) scattering cross-section in barn per electron and A is the atomic weight of the scatterer, F(x,Z) is the atomic form factor and $d\sigma_R/d\Omega$ is the Rayleigh scattering cross-section in barn per electron. Values of S(x,Z) and F(x,Z) were used from the compilations of Hubbel [Hub75].

The electron coherent differential scattering cross-section also known as the Thomson scattering cross-section for polarised radiation is:

$$\frac{d\sigma_R}{d\Omega} = r_0^2 \{1 - sin^2\theta \frac{(1 + P\cos 2\phi)}{2}\} \tag{5.6}$$

where r_0 is the classical electron radius, P is the degree of polarisation, ϕ is the angle between the direction of polarisation and the direction of observation and θ is the scattering angle between the direction of propagation and the direction of observation. The incoherent differential scattering cross-section is given by the Klein-Nishina formula [Hub75]:

$$\frac{d\sigma_C}{d\Omega} = r_0^2 \left[\frac{k}{k_0}\right]^2 \left\{1 - sin^2\theta \frac{(1 + P\cos 2\phi)}{2} + \left[\frac{(k_0 - k)^2}{2k_0 k}\right]\right\} \tag{5.7}$$

where k / k_0 is the ratio of the outgoing to the incident wavenumbers given by the Compton formula:

$$\frac{k}{k_0} = \frac{1}{1 + \alpha(1 - \cos\theta)} \tag{5.8}$$

where $\alpha = E_0/mc^2$ is the incident photon energy in units of the electron rest energy.

For the present case the scattering angle (θ) between the direction of propagation and the direction of observation is 90°, the angle (ϕ) between the direction of polarisation and the direction of observation is 0° and $\alpha = 0.0294$, for the incident photon energy (15 keV) in units of electron mass. A systematic error in the cross-sections related to the fact that the detector subtends a solid angle to the specimen is estimated to be about 5% for the setup. The equations 5.6 and 5.7 reduce to equations 5.9 and 5.10, respectively:

$$\frac{d\sigma_R}{d\Omega} = 3.97 \times 10^{-2} (1 - P) \tag{5.9}$$

and

$$\frac{d\sigma_C}{d\Omega} = 3.75 \times 10^{-2} (1.000837 - P) \tag{5.10}$$

Using values of S(x,Z) and F(x,Z) [Hub75] and a beam energy of 15 keV, the incoherent and coherent cross-sections were calculated for 90° scattering for different degrees of polarisation. They are plotted as a function of atomic number of the scattering atom in fig. 5.14.

If the scatterer has a known composition with elemental weight fraction w_z, the effective Rayleigh or Compton cross-section for any sample may be calculated, according to:

$$\frac{d\sigma}{d\Omega} = \sum_z w_z \cdot \frac{d\sigma(Z)}{d\Omega} \tag{5.11}$$

Both the Compton and Rayleigh scattering cross-sections are polarisation dependent, unlike the production of characteristic X-rays. Photo-electric cross-sections can be calculated [Len87] or can be taken from data tables [Sto70]. Taking the ratio of the fluorescent peak content (N_z) and the scattering peak content (N_s) from a measured spectrum and calculating the theoretical ratio (I_s/I_z), then the concentration (C_z) results in:

$$C_z = \left(\frac{N_z}{N_s}\right)_{exp} \cdot \left(\frac{I_s}{I_z}\right)_{theo} \tag{5.12}$$

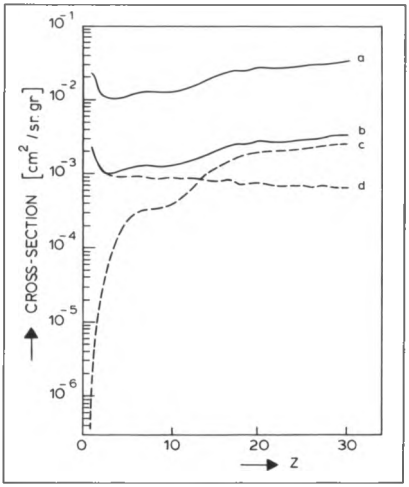

Fig. 5.14 The total scattering coefficients of the elements H through Zn for 15 keV radiation, 90° scattering angle and a degree of polarisation of 0 and 0.9 indicated as curve a and b respectively. Coherent and incoherent mass scattering coefficients for a degree of polarisation of 0.9 are indicated as curve c and d respectively.

5.4.3 Sample preparation

To calibrate the system and to check the linearity as a function of trace element concentrations, Araldite samples were irradiated in a well defined geometry, see section 5.2.2.3. The Araldite was doped with vanadium, cobalt and zinc concentrations of 5, 50 and 500 ppm and prepared in samples of 60 μm thickness. Also Araldite samples of var-

ious thickness (47, 95, 295, 495 µm) doped with vanadium and zinc (100 ppm) were sliced by a microtome. To measure flux densities a 100 nm gold foil layer evaporated onto a 25 µm kapton foil was used. To assess accuracy and precision, the standard reference material bovine liver (SRM 1577) obtained from the National Bureau of Standards (NBS, Washington, DC) was used. To compare minimum detection limits using PIXE, tube-excited XRF and SXRF, the standard reference material human hair HH-1 obtained from the IAEA (Wien) and orchard leaves (SRM 1571) from the NBS were used. To compare minimum detection limits using micro-PIXE and micro-SXRF the elemental doped Araldite samples were used. The powders were pressed into pills with a thickness of 1 mm and put on 3.8 µm hostaphane foil and glued with a 1 % solution of polyformaldehyde in dioxane. To demonstrate the analyzing capabilities of the synchrotron microprobe for measurements biological coupes, such as rat brain sections, have been prepared [Len88].

5.4.4 Sensitivities of SXRF

The intensity of the analytical signal of a given trace element is in general given by equation 5.1 or in somewhat different units by:

$$I_x = N_{ph}\sigma_x n_z A_i A_o \varepsilon_x \Delta\Omega dE_i \qquad (5.13)$$

where N_{ph} is the number of incoming photons within the energy interval dE_i, σ_x(barn/at) is the differential cross-section for the production of characteristic X-rays (including the fluorescence yield and the branching ratio), n_z (at/cm^2) is the number of trace elements seen by the beam, A_i and A_o are the absorption coefficients of the incoming and outgoing photons respectively, ε_x is the efficiency and $\Delta\Omega$ is the solid angle subtended by the detector in relative units (see eq. 5.20). Since sensitivities are usually expressed in counts/g, n_z should be converted to the mass of the trace element using:

$$n_z = \left(\frac{a_z}{A_z}\right)N_0 \qquad (5.14)$$

where a_z and A_z are the mass and the atomic weight of the trace element respectively,

and N_0 is Avogadro's number. The sensitivity of any analytical technique is defined, according to Vis [Vis90c], as:

$$S = \frac{dI_x}{da_z} = N_{ph}\sigma_x\left(\frac{N_0}{A_z}\right)A_i A_o \varepsilon_x \Delta\Omega dE_i \qquad (5.15)$$

The microprobe is developed to be used for a great deal in the bio-medical field, so the sensitivities and also detection limits are determined using biological samples, such as standard reference materials (IAEA human hair HH-1, NBS bovine liver SRM 1577 and NBS orchard leaves SRM 1571) as well as artificially produced standards, e.g. elemental doped Araldite, imitating biological material.

For the determination of the sensitivities and the minimum detection limits a modest slit opening was used, 5 mm horizontally and 1 mm vertically, which means that the experiments have not been performed with the highest flux available. At least a factor ten flux increase can be obtained by maximum opening of the slits with only a minor increase in spotsize. The measured flux during the experiments was about 10^6 ph/(s.mA) and the spotsize 15 × 20 μm horizontally and vertically, respectively.

Table 5.1 shows the experimental and theoretical values of absolute and relative sensitivity for vanadium, cobalt, zinc and bromine, based on the measurement of the Araldite samples. Absolute sensitivities (A.S.) are expressed in weight units (in counts/s.pg) and the relative sensitivities (R.S.) are expressed in relative amounts (in counts/s.ppm or counts/s.$\mu g g^{-1}$). The errors in the theoretical and experimental values are lower than 15% and 10% respectively.

Sensitivity	A.S. (exp)	A.S. (theo)	R.S. (exp)	R.S. (theo)
	(counts/s.pg)	(counts/s.pg)	(counts/s.ppm)	(counts/s.ppm)
V	1.7	2.1	0.03	0.04
Co	4.9	5.1	0.09	0.09
Zn	7.6	8.6	0.14	0.15
Br	13.3	15.1	0.24	0.27

Table 5.1 Experimental and theoretical values of absolute and relative sensitivities

The same set of samples have been measured with the micro-PIXE technique as well. The measurements were performed by the Amsterdam micro-PIXE set-up, which is described elsewhere [Bos84b]. Fig. 5.15 shows the ratio of sensitivities for SXRF and for PIXE (as a function of atomic number) assuming the thin target approximation and the same solid angle of the detector system. This ratio is nothing more than the ratio of the ionization cross-section for X-rays and protons, in this case chosen for typical operational energies 15 keV and 2.5 MeV, respectively, times the ratio of the flux densities of SXRF (3 10^6 particles/(s.μm^2)) and PIXE (2 pA/μm^2 = 1.25 10^7 particles/(s.μm^2)). These flux densities are typical values for the Daresbury and Amsterdam setup, respectively. From fig. 5.15 it can be concluded that for the element calcium the sensitivity for both techniques is equal, and that for higher Z-elements SXRF is favourable and for lower Z-elements PIXE.

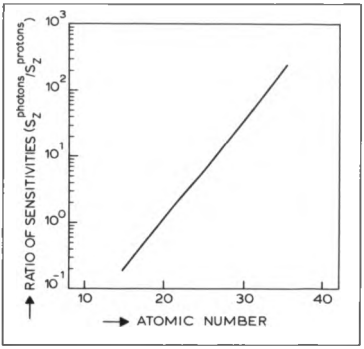

Fig. 5.15 The calculated ratio of sensitivities of photons (15 keV) to protons (2.5 MeV) as a function of atomic number (K lines) assuming the thin target approximation and an equal solid angle of the detection system for both the SXRF and PIXE setup

5.4.5 Detection limits of SXRF

Normally, the detection limits are defined by demanding that the analytical signal I_x has to be greater than three times the standard deviation (σ_B) of the background. Currie [Cur68] has documented the detection limit calculation techniques for statistical processes such as counting. At the limit of detection, the smallest detectable signal, I_{MDL}, is:

$$I_{MDL} = 3\sigma_B \tag{5.16}$$

The lowest weight detectable ($[a_z]_{MDL}$) is thus given by:

$$[a_z]_{MDL} = \frac{I_{MDL}}{S} = \frac{3\sigma_B}{N_{ph}\sigma_x\left(\frac{N_0}{A_z}\right)A_i A_o \epsilon_x \Delta\Omega d E_i} \tag{5.17}$$

The standard deviation (σ_B) of the background is normally taken as $\sigma_B = \sqrt{I_B}$, where the intensity of the background (I_B) is the column of the background present under the fluorescent peak and so dependent on the detector resolution. The sensitivity S and its parameters are defined in the previous section. The intensity of the theoretical background can be expressed in a similar way as equation 5.13 and so the lowest detectable weight can be calculated.

The (experimental) relative minimum detection limit (MDL) is determined by applying Currie's criterion [Cur68], which is:

$$MDL = c\frac{3\sqrt{I_B}}{I_x} \tag{5.18}$$

where c is the mass fraction in parts per million, I_x is the net number of counts in the peak obtained by spectrum fitting (see sect. 5.4.6) and I_B is the number of background counts. According to Bos et al. [Bos84], the number of background counts was taken as the number of counts present in an area 1.2 times the fwhm of the peak. The number of background counts under the peak is the sum of the content of the channels in that region minus the net peak.

Fig. 5.16 shows the relative minimum detection limits for the elements mentioned in Table 1 for SXRF and PIXE, based on Currie's criterion. The absolute minimum detection limit for Zn and Br is 7 and 4 femtogram respectively for SXRF and 2 and 2.2 femtogram respectively for PIXE.

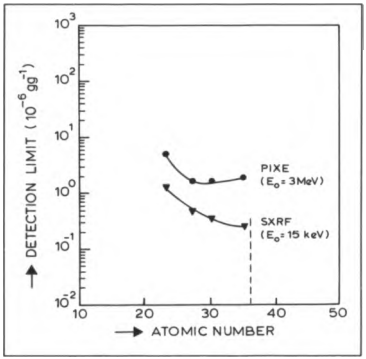

Fig. 5.16 The minimum detection limits measured for elemental doped Araldite for SXRF and PIXE, sample thickness 60 μm and irradiation time 300 sec

Other examples, where the performance of the different techniques is demonstrated, are shown in fig. 5.17 and fig. 5.18. Spectra of human hair and orchard leaves have been produced by PIXE, XRF-tube, SXRF with a broad banded (graphite) monochromator and with a narrow band (silicon) monochromator. The first three spectra of fig. 5.17 and fig. 5.18 have been described and published previously by Bos et al. [Bos84a]. The figure clearly demonstrates the different background shapes in the spectra obtained by irradiating the samples by the different techniques.

Also the effect of polarisation on the Compton scattering in the case of SXRF is clear compared to the XRF Compton scattering, which has a tail down to almost the energy of 10 keV. The decrease of flux due to the narrow energy bandwidth of the silicon

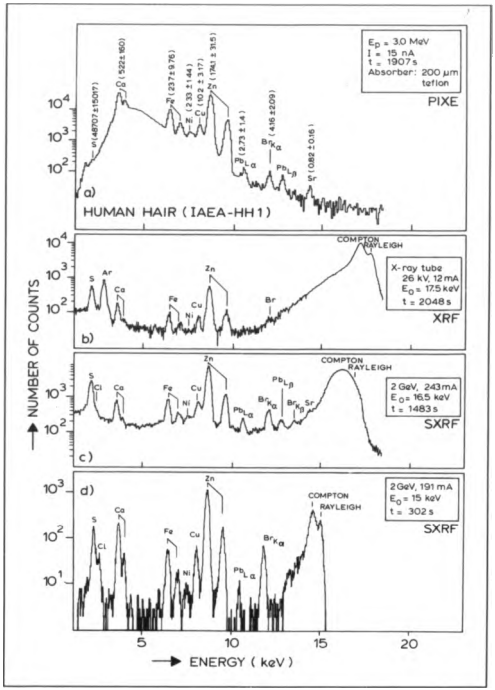

Fig. 5.17 X-ray spectra of human hair (IAEA HH-1) excited by a) 3 MeV protons, b) 17.5 keV photons from a conventional X-ray tube with a Mo anode, c) synchrotron radiation monochromated to 16.5 keV with a broadbanded graphite monochromator and d) 15 keV with a narrowbanded silicon monochromator. Number on fluorescent lines gives (unless otherwise indicated) the concentration of that element in units $\mu g g^{-1}$.

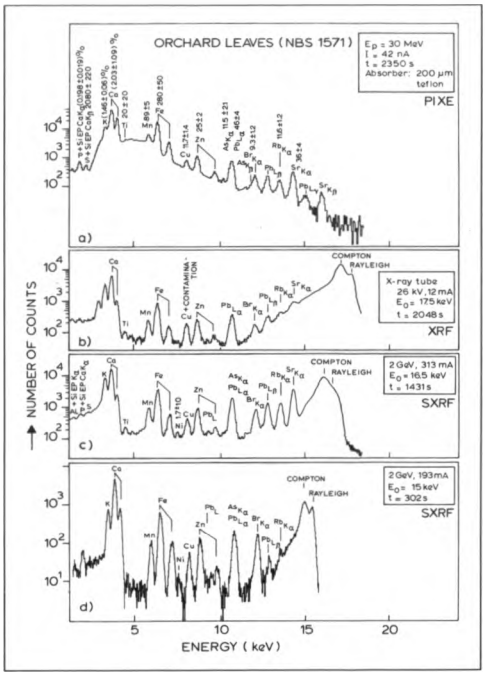

Fig. 5.18 X-ray spectra of orchard leaves (NBS SRM 1571) excited by a) 3 MeV protons, b) 17.5 keV photons from a conventional X-ray tube with a Mo anode, c) synchrotron radiation monochromated to 16.5 keV with a broad-banded graphite monochromator and d) 15 keV with a narrowbanded silicon monochromator. Number on fluorescent lines gives (unless otherwise indicated) the concentration of that element in units $\mu g g^{-1}$.

monochromator compared to the flux in case of the broad bandwidth of the graphite monochromator is compensated by the focussing action of the silicon crystal. As a result of the narrow energy bandwidth, elements with characteristic radiation $\geq$ 10 keV like for instance Pb and Br will have better detection limits because of the lower Compton - and Rayleigh background. From the obtained spectra the relative detection limits were calculated. All data were normalized to 1000 sec irradiation time and for SXRF to 200 mA stored beam. The detection limits derived from the measured spectra are shown in fig. 5.19 and fig. 5.20 for human hair and orchard leaves, respectively, and clearly demonstrate the region where SXRF is favourable compared to the other techniques.

5.4.6 Spectrum analysis

The net intensities of the characteristic X-rays were evaluated by means of a computer routine based on least-square fitting, using the Marquardt algorithm [Blo75]. Spectra include predominant peaks due to coherently and incoherently scattered X-rays in the sample, from the curved monochromator, which selects nearly monochromatic radiation with a calculated bandwidth of about 300 eV. Note that for Si(111) the second order reflection is absent, owing to the symmetry in the diamond cubic structure of silicon. The coherent peak appeared to have a near Gaussian shape and was found at 14.89 ± 0.02 keV. The incoherently scattered peak maximum was found at 14.47 ± 0.02 keV, which corresponds to the theoretical value of 14.468 keV calculated with the Compton formula for an average scatter angle of 90°.

5.4.7 Concentration assignment by the calibration method

In order to correlate specific X-ray intensities with elemental weights or concentrations for biological material, homogeneous single-element reference specimens were used. Known concentrations (5, 50, 500 ppm) of vanadium, cobalt and zinc were doped in 60 μm thick sliced Araldite. All concentration plots, corrected for self absorption, in fig. 5.21, show a linear dependence of the ratio of the fluorescent signal over the Compton - plus Rayleigh peak on the concentration. The curves in the figure hold for thin targets, so if absorption cannot be ignored the plots have to be corrected by the absorption

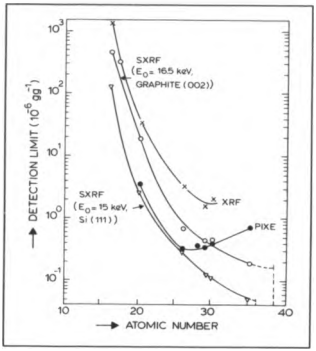

Fig. 5.19 Detection limits of several elements in IAEA human hair for different excitation modes derived from the spectra shown in fig. 5.17

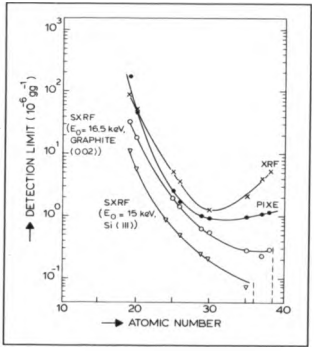

Fig. 5.20 Detection limits of several elements in NBS orchard leaves for different excitation modes derived from the spectra shown in fig. 5.18

correction term, see equation 5.2. If absorption cannot be ignored the scale of the vertical axis in fig. 5.21 has to be multiplied by the absorption term.

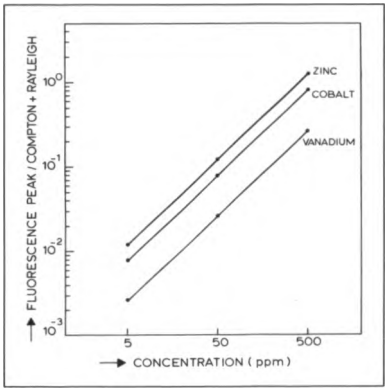

Fig. 5.21 Calibration plots for vanadium, cobalt and zinc. C is the ratio of the fluorescent signal over the sum of the Compton- and Rayleigh peak.

5.4.8 Concentration assignment by the polarisation method

Concentrations have been determined from the reference standard material bovine liver (NBS SRM 1577) in two ways, using the methods outlined in the sections on theory (sect. 5.4.2) and calibration (sect. 5.4.7) respectively. Counts of the fluorescent peaks and of the Compton- and Rayleigh peaks have been taken from spectrum fig. 5.22. For the determination of the coherent and incoherent mass scattering coefficient, the degree of polarisation is needed.

The polarisation factor was determined on a thin titanium foil, with thickness 0.4 μm. From the measured spectrum the ratio of the titanium peak (I_{Ti}) and the sum of the

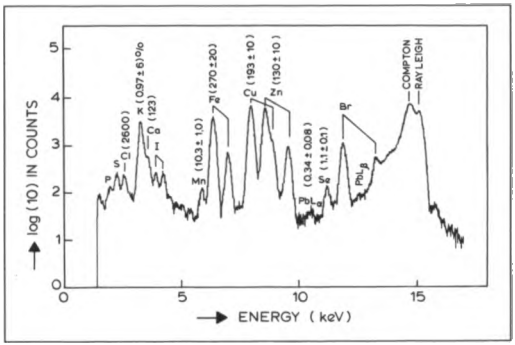

Fig. 5.22 X-ray spectrum of the reference standard bovine liver (NBS SRM 1577) excited by 15 keV radiation (2 GeV, 169 mA, 907 sec)

Compton - and Rayleigh peaks (I_{CR}) can be calculated. Applying equation 5.13 and assuming that absorption can be neglected, the titanium fluorescent signal is expressed by:

$$I_{Ti} = N_{ph} dE_i(ph) \cdot \sigma_{Ti}\left(\frac{cm^2}{at}\right) \cdot n_{Ti}\left(\frac{at}{cm^2}\right) \cdot \Delta\Omega \qquad (5.19)$$

where the solid angle of the detector ($\Delta\Omega$) is defined by:

$$\Delta\Omega = \frac{O_{det}}{4\pi R^2} \qquad (5.20)$$

with O_{det} is the active crystal area of the detector and R is the sample-detector distance.

The number of coherent and incoherent scattered rays are:

$$I_{CR} = N_{ph} dE_i\,(ph) \cdot \left[\frac{d\sigma_{coh}}{d\Omega} + \frac{d\sigma_{incoh}}{d\Omega}\right] \left(\frac{cm^2}{sr \cdot g}\right) \cdot \rho d \left(\frac{g}{cm^2}\right) \cdot d\Omega\,(sr) \qquad (5.21)$$

where the solid angle of the detector ($d\Omega$) in steradians is defined by:

$$d\Omega = \frac{O_{det}}{4\pi R^2} \cdot 4\pi\,(sr) \qquad (5.22)$$

Now inserting the number of titanium atoms seen by the beam into equation 5.19, which is:

$$n_{Ti} \left(\frac{at}{cm^2}\right) = \frac{N_0}{A_{Ti}} \left(\frac{at}{g}\right) \cdot \rho d \left(\frac{g}{cm^2}\right) \qquad (5.23)$$

the ratio reduces to:

$$\frac{I_{Ti}}{I_{CR}} = \frac{\sigma_{Ti} \cdot \frac{N_0}{A_{Ti}}}{\left[\frac{d\sigma_{coh}}{d\Omega} + \frac{d\sigma_{incoh}}{d\Omega}\right] \cdot 4\pi} \qquad (5.24)$$

where N_0 is Avogadro's number, A_{Ti} is the atomic weight of titanium, ρ the titanium density and d the thickness. The degree of polarisation found for the measurement was 0.939.

The total mass scattering coefficient for bovine liver, with the composition taken from Gladney [Gla80], could now be calculated with P = 0.939 and turned out to be 1.1 10^{-2} cm^2/g. Kubo et al. [Kub79] have listed average experimental cross-sections for various biological samples including bovine liver and reported the small variation in cross-section among the samples. The mass scattering cross-sections typically do not vary more than a few percent from the average, with a maximum of 10 %.

Table 5.2 shows the calculated concentrations, the values determined from the calibration line and the certified values for different trace elements in bovine liver SRM 1577. The errors indicated in the first two columns are only statistical errors. X-ray production cross-sections are estimated to be lower than 15% for all the elements and the coherent and incoherent cross-sections are accurate within 5%. Probable errors in the spectrum fitting procedure are not taken into account. The errors of the measured and NBS values are larger because the spread by different analytical methods is included.

Element	Cal. method[1]	Pol. method[2]	Mea. values[3]	NBS values[3]
K	8395 ±59	8654 ±61	9430 ±990	9700 ±600
Mn	9.0 ±0.3	9.3 ±0.3	10.2 ±0.9	10.37 ±1.0
Fe	241 ±2	247 ±2	263 ±13	270 ±20
Cu	193 ±2	199 ±2	189 ±21	193 ±10
Zn	133 ±1	137 ±1	132 ±10	130 ±10
Se	1.3 ±0.1	1.3 ±0.1	1.08 ±0.07	1.1 ±0.1
Br	10.5 ±0.2	10.7 ±0.2	8.7 ±1.7	(10)

1) this work, determined by the calibration method outlined in section 5.4.6
2) this work, determined by the polarisation method outlined in section 5.4.2 and 5.4.7
3) measured and NBS certified values from Gladney [Gla80]

Table 5.2 Trace element concentrations in Bovine Liver (SRM 1577) in ppm (μg/g)

5.4.9 Applications

The synchrotron microprobe has been employed for experiments on human hair and hair roots [Lan89a], hamster tooth germs [Lan90b,Tro90], gel electrophoresis samples and rat brain sections. Also other type of samples have been investigated and elemental distributions have been determined for archaeological bones, fluid inclusions in quartz, fly ash particles, glass particles, cosmic dust, chondrites and other geological samples.

5.4.9.1 Zinc determination in the hippocampus

In this paragraph experiments on rat brain sections, more specifically the hippocampus, will be discussed. In particular the role of zinc has been investigated thoroughly [Fre81]. Wensink et al. [Wen87] studied the effect on dietary zinc deficiency on the zinc content of mossy fibres of the rat hippocampus. Fig. 5.23 shows a photograph of a control rat brain section of 4 μm thickness. This particular coupe has been measured with micro-PIXE as well as micro-SXRF. Specimen preparation, micro-PIXE setup and data analysis have been described by Lenglet [Len88]. A synchrotron radiation linescan, constructed as a 26-points measurement of 300 sec each over a length of 400 μm, was measured along a line parallel to and 250 μm above the line of the PIXE scan. Fig. 5.24 shows a typical synchrotron radiation spectrum from a point measurement and fig. 5.25 shows the zinc distribution over the hippocampus. Concentration assignment of the zinc

Fig. 5.23 Photograph of a rat brain section. The dimension of the PIXE line scan, seen as the black line, is 2 mm.

distribution has been determined by the calibration method. In the mossy fibre region, where zinc concentrations have highest values, the mean concentration turned out to be 114 ± 8 ppm with a mean zinc content of 60 ± 6 ppm elsewhere in the section. The ratio of mean zinc content in and outside the mossy fibre zone was 1.9 ± 0.33, which is con-

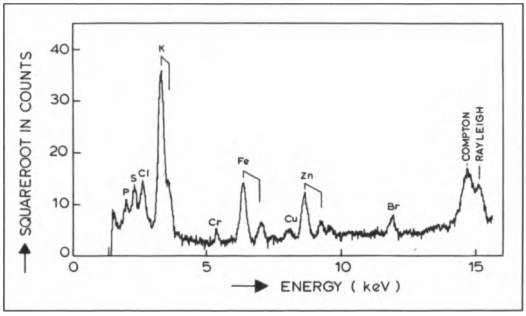

Fig. 5.24 A typical synchrotron radiation X-ray spectrum of a point measurement on the line scan measured by micro-SXRF in 300 sec

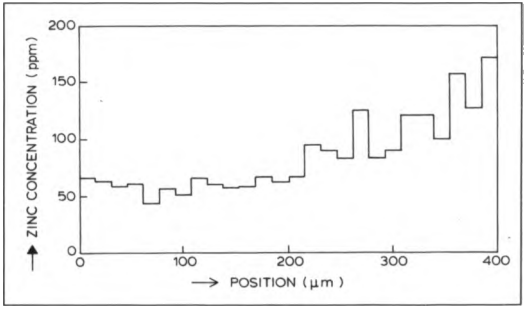

Fig. 5.25 Elemental zinc distribution performed across the hippocampus

sistent with the value of 2.1 ± 0.33 for controls found by Lenglet [Len88]. The photograph fig. 5.23 taken after the measurements of PIXE and SXRF clearly shows visible radiation damage in case of PIXE.

Fig. 5.26 shows the matrix thickness distribution of brain tissue before and after proton bombardment. This figure demonstrates not only the considerable loss of material, but also the phenomenon that this loss is position dependent. The technique to establish mass loss during irradiation has been described by Vis [Vis88]. In the SXRF case no visual radiation damage could be found by investigating the coupe with a light microscope.

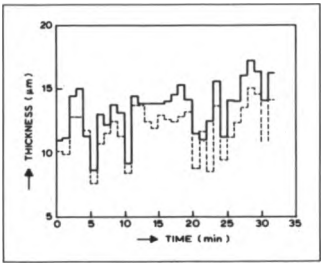

Fig. 5.26 Thickness variation of matrix brain tissue before (solid line) and after (dotted line) proton bombardment for 1 hr with 1 nA beam. Results shown are from a line scan divided into 32 pixels.

The local radiation dose delivered by the synchrotron microprobe and the proton microprobe can be evaluated according to Kirz and Sayre [Kiz80] and Lenglet et al. [Len85] respectively. The doses were calculated according to the experimental circumstances and amounted to about 10^2 J/g and 10^6 J/g, for the micro-SXRF and the micro-PIXE experiments respectively. These local radiation doses seem to be consistent with Kirz and Sayre [Kiz80], who state that a dose of 10^2 J/g is sufficient to kill living cells and that a dose of 10^4 J/g is sufficient to cause serious structural changes in the sample.

5.4.9.2 Zinc and copper determination in hamster tooth germs

Generally, hamster tooth germs are studied for the role of fluorine on the mineralisation of the dental layer. The discussion from a biochemical point of view can be found in Lyaruu et al. [Lya90]. The role of essential elements like zinc and copper of enzymes which take part in the mineralisation process is not known, therefore a pilot study has been performed.

Fig. 5.27 shows a photograph of a hamster tooth germ section of 2 μm thickness. This coupe has also been measured with micro-SXRF as well as micro-PIXE. In case of micro-PIXE the beam size was $5 \times 20\ \mu m^2$ and the beam energy 3 MeV with 400 pA beam current and 20 min scan time over 500 μm. Fig. 5.28 shows the measured sum spectrum for the (top) scan indicated in the picture. Also a line scan was carried out with the synchrotron microprobe with a beam size of $10 \times 20\ \mu m^2$. The line scan was constructed as a 20 points measurement of 5 min. per point over a length of 1 mm. The micro-SXRF line scan was performed parallel to but 200 μm above the PIXE line scan. The

Fig. 5.27 Photograph of a hamster tooth germ section of 2 μm thickness. The dimension of the PIXE line scans, seen as black lines, is 500 μm. The SXRF line scan was done 200 μm above the top PIXE scan.

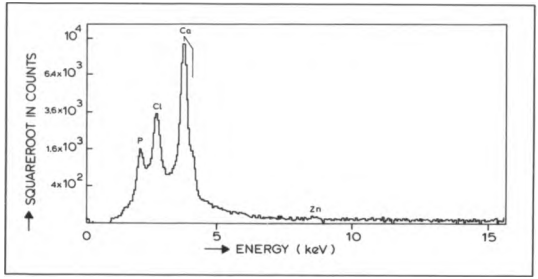

Fig. 5.28 The X-ray fluorescence sum spectrum of the (top) line scan measured by micro-PIXE in 20 min over a distance of 500 µm

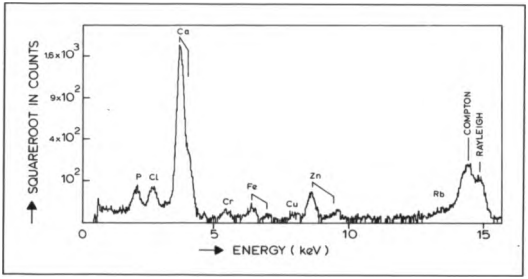

Fig. 5.29 The X-ray fluorescence sum spectrum of the line scan (11 points of equi-distance) measured by micro-SXRF in 55 min over a distance of 500 µm

micro-SXRF sum spectrum over 500 µm parallel to the PIXE line scan is shown in fig. 5.29. Again it is shown that the sensitivity for the heavier elements like copper and zinc is better for SXRF than for PIXE.

Finally figs. 30a, b, c and d show the elemental distributions measured by micro-SXRF over the dental layer for the elements calcium, phosphorus, copper and zinc. The concentrations of copper and zinc have been determined by the calibration method (see sec. 4.5.7). The calcium and/or phosphorus distributions are needed to be able to locate the copper and zinc distributions and are plotted in relative units (the ratio of the number of fluorescent counts and the sum of the Compton and Rayleigh counts). The local radiation doses delivered by the synchrotron microprobe and the proton microprobe were calculated according to the experimental circumstances and amounted to about 250 J/g and 5×10^5 J/g, respectively.

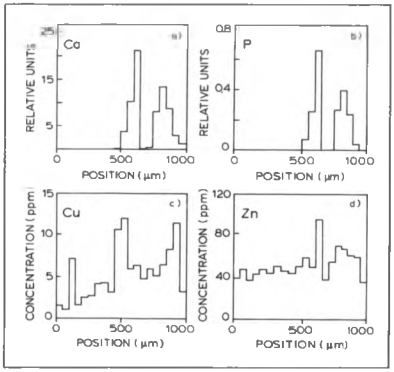

Fig. 5.30 The elemental distributions obtained by micro-SXRF for (a) calcium, (b) phosphorus, (c) copper and (d) zinc

Chapter 6

Crystal optics for the SRS (Daresbury) and the ESRF (Grenoble)

6.1 Introduction

In the preceding Chapters 4 and 5 it is demonstrated that with a concave bent ellipsoidally shaped Si(111) crystal as a focussing device a microprobe can be constructed. The analytical results and applications show the potential of the microprobe. However, the optical features and analytical capabilities are strongly dependent on the source parameters, in particular the brilliance of the source. If the source size is smaller higher flux densities and smaller spotsizes can be obtained for the same combination of focussing device and source distance. As third generation (insertion-based dedicated) storage rings are under construction, for instance the ESRF at Grenoble, it is useful to calculate the performance of a microprobe, when the same type of optics developed at Daresbury is used. Also more sophisticated systems are options to minimize aberrations, because higher flux is available at these facilities. This chapter deals with the comparison of the crystal optics used at Daresbury and what can be expected if the ESRF source parameters are used rather than the SRS source parameters. Also a comparison is made for more sophisticated, combined systems like Kirkpatrick-Baez and Wolter systems.

6.2 Beam conditions and source parameters: SRS versus ESRF

The source parameters, the horizontal and vertical source size (fwhm) as well as the divergence, used in the calculations are listed in table 6.1 for both the SRS and the ESRF. The beam conditions assumed are 2 GeV and 100 mA for the SRS and 6 GeV and 100 mA for the ESRF. ESRF data are taken and calculated from values specified in the "Red Book" [Red87] and in an ESRF report [Boe89]. The total beam line power and the surface power density is calculated according to Mourikis et al. [Mou88]. Note that in general no damage occurs for $P < 50$ W/cm^2 [Sai89a]. Fig. 6.1 shows the intensity for the energy range up to 30 keV for both machines. For trace element analysis this energy range is basically sufficient to excite and to detect the K- or L-lines of all the elements.

storage ring	SRS	ESRF
electron energy (GeV)	2	6
magnetic field (T)	1.2	0.8
critical energy (keV)	3.9	19.2
horizontal source size (mm)	2.0	0.376
vertical source size (mm)	0.3	0.303
horizontal source divergence (mrad)	4	6
vertical source divergence (mrad)	~0.1	~0.1
total beam line power (kW)	~2	~6
surface power density (W/cm^2)	~0.2	~10

Table 6.1 Beam conditions and source parameters for the SRS and the ESRF

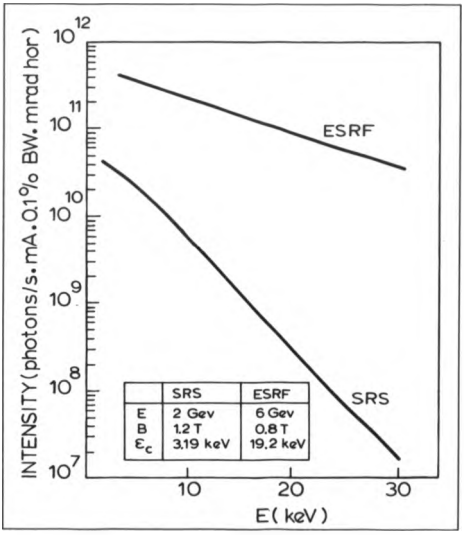

Fig. 6.1 The photon spectrum from the SRS and the ESRF for dipole bending magnets

6.3 X-ray optical configurations

6.3.1 Single crystal option

As is concluded in Chapter 3 the ellipsoid is the best focussing device when a single crystal is used. Also discussed is that in the X-ray regime coma is the main aberration for Bragg reflection from curved crystals or reflection from curved mirrors. In order to be free of coma an optical system must obey the Abbé sine condition, which is equivalent to the condition that all the geometric paths through the optical system produce the same final magnification [Fra77]. In practice, this means that two or an even number of reflections are necessary to reduce or eliminate coma. This is one of the reasons for investigating the performance of double crystal options, such as Kirkpatrick-Baez or Wolter systems. It is evident that a better resolution obtained by a double crystal combination can be reached only at the cost of reduced flux compared to single crystal systems.

6.3.2 Double crystal option

It is worthwhile considering the double crystal option because smaller spot sizes can be obtained by the reduction of coma. Already in 1948 Kirkpatrick and Baez described the optical features of double crystal configurations [Kir48]. Two spherical or cylindrical reflectors are crossed so that their meridional planes are at right angles (see fig. 6.2). Another method is described by Wolter [Wol50], where the reflecting surfaces are

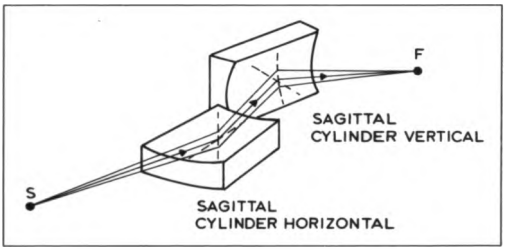

Fig. 6.2 The Kirkpatrick-Baez geometry

coaxial surfaces of revolution (i.e. paraboloids, ellipsoids and hyperboloids) about the axis of symmetry (see fig. 6.3) so that the back focus of the first coincides with the focus of the second. X-ray microscopy provided the original motivation for the development of

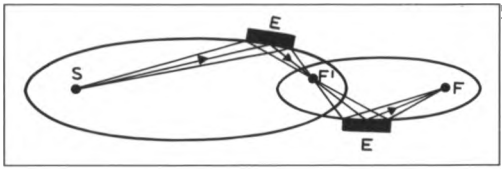

Fig. 6.3 A Wolter system

both Kirkpatrick-Baez and Wolter systems. So far, the former has been used predominantly for microscopes and the latter for telescopes, although both systems are used as the basic optics in existing microprobes (see section 3.2). The advantage of the Kirkpatrick-Baez system is that this system can be made astigmatism free, which is not the case when using one spherical or cylindrical reflector. Furthermore coma is reduced by approximating the Abbé sine condition. Another advantage is that simple surfaces are used, which can be produced easily by conventional techniques. This is in contrast with Wolter systems, where aspherical surfaces of revolution are used, but coma is more strongly reduced.

The performance of a third combination of reflectors (planar-ellipsoid) is also calculated. This is a compromise between the single crystal option and the double crystal options mentioned (see fig. 6.4). The reason is that by use of this combination the central ray remains horizontal, this in contrast to the single crystal option, where the focal plane is deflected from the horizontal plane under the double Bragg angle. A consequence is that by exchanging optical elements for other energies the vacuum chamber needs only be translated instead of rotated in order to maintain the minimum projected spotsize. The geometry of the Kirkpatrick-Baez system is even more awkward than the geometry of a single crystal, because the focal plane is deflected in two dimensions from the initial

plane rather than in one dimension. Although the use of a planar as the first optical component and an ellipsoid as the second does not influence the Abbé sine condition as compared to only a single ellipsoid, the planar can be used as a cooling device to accept the high thermal beam loads. The other double crystal options are more critical, because now the curved crystal as first optical component has to deal with the thermal loads.

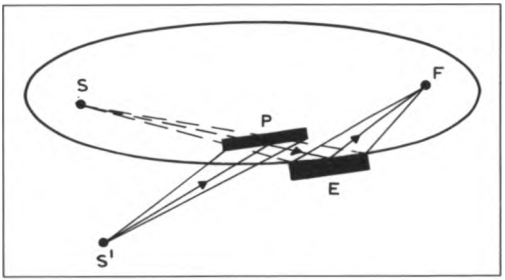

Fig. 6.4 The planar-ellipsoid configuration

6.4 Ray-tracing results of single and double crystal options

Five optical configurations have been ray-traced for the SRS (Daresbury) and the ESRF (Grenoble) situation. These are the single crystal option (ellipsoid) and the double crystal options (a Kirkpatrick-Baez system, a Wolter system and a planar-ellipsoid combination) and a planar-planar combination as reference. The chosen crystal is Si(111) in all cases. The calculations are based on a minimum radius of curvature of 10 cm and the distance to the source of 80 m. The Darwin width is calculated according to section 4.4.5 and is 3.7 arcsec for a flat Si(111) crystal and 6.6 arcsec for the curved crystal for 15 keV.

The tables 6.2 and 6.3 list the results of ray-tracing for the five configurations for the SRS and ESRF respectively with the crystals defined for 15 keV. The tables consist of a column of the ratio (N_s) of the number of successful rays through the optical system

and the number of started rays (10^6), the maximum accepted horizontal divergence (d_h), the bandwith (dE), the horizontal spotsize (s_h), vertical spotsize (s_v), the flux and the flux density. The initial beamline intensity for 15 keV is 9 10^7 photons/(s.mA.mrad hor. eV) and 7.4 10^9 photons/(s.mA.mrad hor.eV) for the SRS and the ESRF respectively. In addition to15 keV, the 30 keV and 45 keV have also been ray-traced to investigate the energy dependence of the planar-planar, ellipsoid and planar-ellipsoid configurations with other geometrical circumstances equal, i.e. the same minimum radius of curvature and location to the source. The Bragg angle is derived from the chosen energy. For a flat

SRS	N_g	d_h	dE	s_h	s_v	flux	fluxdensity
	ab. units	mrad	eV	μm	μm	ph/s.mA	ph/s.mA.μm^2
planar-planar	7 10^{-2}	0.65	-5	50000	3000	1 10^7	7 10^{-2}
ellipsoid	7 10^{-4}	0.44	-500	10	4	8 10^6	2 10^5
planar-ellipsoid	7 10^{-4}	0.44	-4	10	4	9 10^4	2 10^3
Kirkpatrick-Baez	5 10^{-5}	0.024	-5	4	11	3 10^2	6 10^0
Wolter	2 10^{-5}	0.05	-35	3	0.5	1.5 10^2	1 10^2

Table 6.2 Ray-tracing results for the SRS (see text)

ESRF	N_g	d_h	dE	s_h	s_v	flux	fluxdensity
	ab. units	mrad	eV	μm	μm	ph/s.mA	ph/s.mA.μm^2
planar-planar	3 10^{-2}	0.65	-5	50000	3000	2.0 10^8	1.5 10^0
ellipsoid	3 10^{-4}	0.44	-500	1.9	1.6	1.5 10^8	5.0 10^7
planar-ellipsoid	3 10^{-4}	0.44	-4	1.9	1.6	1.5 10^6	5.0 10^5
Kirkpatrick-Baez	2 10^{-5}	0.005	-5	4.0	1.9	9.0 10^2	1.0 10^2
Wolter	7 10^{-6}	0.04	-35	0.6	0.4	1.5 10^3	6.5 10^3

Table 6.3 Ray-tracing results for the ESRF (see text)

crystal the Darwin width is 1.9 arcsec and 1.2 arcsec, and for the curved crystal 9.9 arcsec and 6.6 arcsec, for 30 keV and 45 keV respectively. The whole geometry is fixed, if the Bragg angle, the minimum radius of curvature and the location of the crystal is known. Fig. 6.5 shows the flux density as a function of energy for the three configurations for SRS and ESRF conditions. Finally table 6.4 demonstrates the energy depend-

ence of the spot size, the flux and the flux density for the planar-ellipsoid combination for both storage rings.

The method for calculating what flux density is needed, assuming a countrate of 1 count/sec, to detect for instance 10 ppm zinc in an organic matrix is described in section 5.3.1.3 and 5.3.2.2 . In the same way an estimate can be made for the zinc concentration which can be detected in a 10 μm thick organic matrix with the calculated flux density from table 6.4, if the same countrate criterion is fulfilled and assuming 150 mA in the storage ring. As an example, the planar-ellipsoid microprobe with 15 keV excitation energy can detect 200 ppm under SRS and 13 ppm under ESRF conditions.

	SRS (Daresbury)			ESRF (Grenoble)		
energy	**spotsize**	**flux**	**fluxdensity**	**spotsize**	**flux**	**fluxdensity**
keV	x.z μm^2	ph/s.mA	ph/s.mA.μm^2	x.z μm^2	ph/s.mA	ph/s.mA.μm^2
15	10x4	$9.5\ 10^4$	$2.4\ 10^3$	1.9x1.6	$1.5\ 10^6$	$5.0\ 10^5$
30	19x7	$1.4\ 10^3$	$1.0\ 10^1$	3.9x3.4	$1.5\ 10^6$	$1.0\ 10^5$
45	29x10	$1.7\ 10^1$	$5.9\ 10^{-2}$	5.7x4.9	$5.0\ 10^5$	$2.0\ 10^4$

Table 6.4 Ray-tracing results for the planar-ellipsoid configuration

6.5 Conclusion

Although the ellipsoid delivers the highest flux density owing to its greater bandwith, and although a combination of aspherical shapes of revolution can obtain the smallest spot size owing to the strong reduction of coma, the planar-ellipsoid combination seems to be the best option as a compromise with some additional attractive features.

The planar is more able to tackle problems of heat load compared to curved crystals. Also this configuration is elegant when interchanging crystals for other energies. Note that for a fixed minimum radius of curvature and energy an unique ellipsoid exists, so that the geometry changes with energy.

With two crystals it is possible to filter out higher orders or unwanted reflections by a minor mistuning of the Bragg angle. A mistuning of the planar crystal has no effect or a minor effect only on the optical properties of the focussing system.

Also the planar-ellipsoid combination is more easy to align than a combination of two curved crystals. A small mismatch of the planar with respect to the ellipsoid affects the energy only slightly but does not affect the final optical properties. For Kirkpatrick-Baez or Wolter systems a mismatch of one element with respect to the other has consequences for the energy as well as the optical geometry.

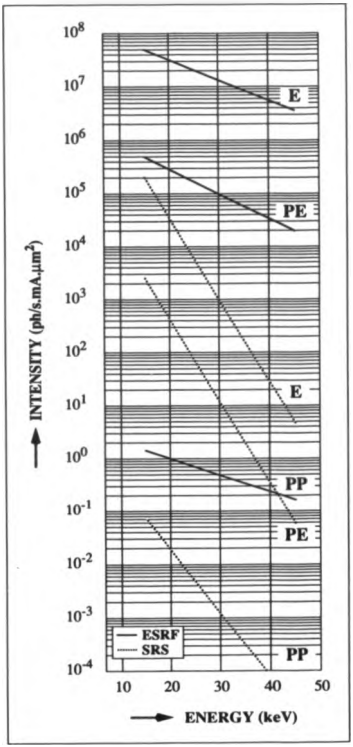

Fig. 6.5 The fluxdensity as a function of energy for different optical systems for both the SRS and the ESRF (E=ellipsoid, PE=planar-ellipsoid, PP=planar-planar)

Chapter 7

Discussion and conclusions

7.1 Discussion

At present, a few synchrotron microprobes are available at institutions equipped with an electron storage ring. Different approaches have been chosen to focus beams of X-rays to spot sizes of about one to tens of μm. Compared with ion probes, the spatial resolution is not as good yet, but already the synchrotron microprobe deserves a place among the analytical microprobes owing to its special advantages. Major advantages of the synchrotron beam are the much lower radiation damage caused by the beam, its very high stability and the higher cross-sections for inner-shell ionisation, especially for the heavier elements.

The performance of the optics of the synchrotron microprobe at Daresbury is limited mainly by the source parameters, in particular the horizontal and vertical source size. To the first order the spotsize of the microprobe decreases proportionally with the reduction of the source size. The main aberration term in X-ray optics is coma and at least two reflections are needed to meet the Abbe' sine condition. The technique of focussing using an ellipsoidal crystal as the single optical component is not the best solution in terms of optics but it is simple in its use and delivers the highest flux as compared to combined or compound systems. The use of crystals in contrast to mirrors or multilayers is basically not limited to lower X-ray energies. For the Daresbury Photon Microprobe the chosen energy is limited by the available intensity of the source which determines the measuring time to perform line- or area scans. Measuring times of more than about two hours are not very practical.

Good agreement was found between the measured spot profile and the profile calculations done by the ray-tracing program, which is indicative of the good overall shape accuracy of the ellipsoidally bent crystal. However, the measured vertical spot size, expressed in fwhm, is larger than the expected vertical spot size based on ray-tracing calculations. As discussed in sect. 3.3, the ray-tracing program uses square source profiles and the curved crystal is simulated as a geometrical shape with no simulation of the penetra-

tion of rays into the crystal. Also it is assumed that the Bragg planes are parallel to the surface. A mismatch generates aberrations and these can be substantial especially in the diffraction plane which can be seen from aberration theory, outlined in Chapter 3.

The advantage of the higher brightness of the third generation synchrotrons is that the flux in the spot will be higher and the resolution of the spot will be better. The higher flux available will allow the use of wavelength dispersive systems. In combination with other techniques such as EXAFS and Tomography the optics developed can be used to extend these techniques to applications on the micrometre scale (micro-EXAFS and micro-Tomography). Smaller spot sizes make the technique (micro-SXRF) more competitive with other analytical techniques.

7.2 Suggestions for further work

The main research program as reported in this thesis, both theoretical and experimental, has been concerned with X-ray optics, specifically for Trace Element Analysis. For the Daresbury facility the implementation of the chosen optics into a setup for Trace Element Analysis turned out to be successful. Further work must be focussed on software development for data acquisition and display modes of the data. The program for the measurement of single spectra is functioning satisfactorily, however for line- or area scans the program is underdeveloped and needs modification and extension to current standards, such as the use of menu's for choosing options, windows for the simultaneous use of programs and colours for displaying elemental distributions. The implementation of established X-ray analysis software packages like AXIL or CRISS might be useful.

From the aberration theory, outlined in Chapter 3, the basis is given to derive for asymmetrical cut crystals the necessary equations for meridional and sagittal focussing as well as the condition for a stigmatic system. It is worthwhile to consider the use of asymmetrical cut crystals for curved crystal X-ray optics, especially the effect on the focus conditions and aberrations to be expected. An advantage of asymmetrical cut crystals is that the same geometry can be used when crystals are exchanged for other energies.

The simulation program can be further improved by the implementation of non-square source profiles. Another useful improvement of the simulation program would be

the implementation of 2D displays of the topograms, in particular the distribution in the focal plane. Also the option to study the depth effects for a particular geometrical shape as well as the effect of mismatch of the Bragg planes and the surface is very useful for the understanding of the focussing behaviour of curved crystals.

If high quality silicon crystals can be produced in thinner slices, focussing can be improved by applying higher curvatures. Also the use of glass moulds can give better results by the reduction of unwanted reflections of the backing for higher energies.

Reliability of the XYZ stage can be improved by the implementation of optical rulers, where the readout is independent from the motor actions. Also a special focussing crystal stage with independent motors with readout would improve the flexibility of the system. Especially in combination with good diagnostics to display the spot, the alignment procedure can be done more quickly. The alignment times need to be reduced when different wavelength crystals are to be used.

The alignment procedure of the crystal needs further care and attention. Basically there is a lack of good beam diagnostics. The fluorescent screen in use (ZnS) is functioning. The grain size however is big compared to the beam dimensions and the ZnS layer is too thick so that the visible fluorescent spot is blurred by scattering. Improvement can be reached by a thin layer of a fluorescent single crystal. For example CsI gives better images though the intensity is very weak. To improve the alignment procedure the use of two-dimensional X-ray detectors are also an option. Although the resolution of these is mostly worse than the beam diameter, the detector does not need to be placed in the focal plane to have a diagnostic tool to minimize aberrations.

7.3 Conclusions

The results as presented in this thesis show that the concept of ellipsoidal focussing is successful and that the criteria adopted for the construction of a synchrotron microprobe (in brief, a small spot size, a high flux, a "high" excitation energy and a high peak-to-background ratio) are fulfilled.

Using an ellipsoidally concave bent Si(111) crystal a spot size of 10 μm horizontal-

ly and 15 μm vertically has been obtained, corresponding to a demagnification of the source dimensions by a factor 200 horizontally and a factor of 20 vertically or to a spot size reduction of the unfocussed beam at 80 m from the source by a factor 1000 horizontally and a factor 20 vertically.

The measured fluxdensity of 10^4 photons/(s.mA.μm^2) was a factor 10^4 higher than the reflection from a flat Si(111) crystal. The fluxdensity is sufficient for the detection of K-lines of the elements in the transition range and the L-lines close up to Bi on the sub-ppm level with a spatial resolution of about 10 μm. Analytical methods, like the calibration- and polarisation method, have been described which are to quantify the measured data, which demonstrates that absolute quantities of the order of femtograms have been measured in biological systems. Artificially produced samples, standard reference materials and demonstration experiments have already shown great potential in the study of biological, inorganic and geological samples.

The limitation of the Daresbury X-ray microprobe is not the quality of the ellipsoidal crystal but the quality of the X-ray source in terms of source dimensions. The quality of the optics of future X-ray microprobes can be improved, either by the new generation of storage rings producing point-like X-ray sources with narrow natural collimation or by new X-ray optical focussing techniques and technologies such as for instance the Bragg-Fresnel zoneplates which seem very promising. The limited availability of synchrotron facilities may hamper a fast development of better microprobes, although new storage rings, socalled third (or fourth) generation machines such as the ESRF and the APS, are under construction. It is to be expected that, owing to the high brightness of these new sources and owing to the development of insertion devices in the electron beam to obtain small source sizes, the future synchrotron microprobes will have spatial resolutions comparable with the ion probes in operation now ($\geq$ 0.5 μm). Especially for these very small spots, the advantage of lower radiation damage becomes very important in a variety of applications.

Appendix 1

List of acronyms and abbreviations

AAS	Atomic Absorption Spectroscopy
AEM	Auger Electron Microscopy
AES	Auger Electron Spectroscopy
B.E.	Backscattered Electrons
CL	Cathodoluminescence
CTEM	Conventional Transmission Electron Microscopy
EDS	Energy Dispersive (X-ray) Spectroscopy
EDX	Energy Dispersive (X-ray) Spectrometry
EELS	Electron Energy Loss Spectroscopy
EID	Electron Induced Desorption
EM	Electron Microscopy
EPMA	Electron Probe (X-ray) Microanalysis
E.S.	Electron Spectrometer
EXAFS	Extended X-ray Absorption Fine Structure
EXELFS	Extended Electron Loss Fine Structure
HEED	High Energy Electron Diffraction
IM	Ion Microscopy
IMMA	Ion Microprobe Mass Analysis
IR	Induced Radioactivity
LS.	Ion Spectrometer
ISS	Ion Scattering Spectrometry
LAMMA	Laser Microprobe Mass Analysis
LEED	Low Energy Electron Diffraction
MS	Mass Spectrometry
M.S.	Mass Spectrometer
NMR	Nuclear Magnetic Resonance

Appendix 1

NRA	Nuclear Reaction Analysis
OES	Optical Emission Spectroscopy
O.S.	Optical Spectrometer
PAS	Photo Acoustic Spectrometry
PEM	Photo Emission Microscopy
PIXE	Proton (Particle) Induced X-ray Emission
PIGE	Proton (Particle) Induced γ-ray Emission
PRA	Prompt Radiation Analysis
RAMAN	Laser Raman spectroscopy
RBS	Rutherford Back Scattering
SAM	Scanning Auger Microscopy
SCANIIR	Surface Chemical Analysis by Neutral and Ionized Impact Radiation
S.E.	Secondary Electrons
SEM	Scanning Electron Microscopy
SIMS	Secondary Ion Mass Spectrometry
STEM	Scanning Transmission Electron Microscopy
(S)TIM	(Scanning) Transmission Ion Microscopy
SXRF	Synchrotron X-ray Fluorescence
TEELS	Transmission EELS
TEM	Transmission Electron Microscopy
THEED	Transmission HEED
UPS	Ultraviolet Photoelectron Spectrometry
WDS	Wavelength Dispersive (X-ray) Spectrometry
XPS	X-ray Photoelectron Spectrometry
XRD	X-ray Diffraction
XRF	X-ray Fluorescence
X.S.	X-ray Spectrometer

Appendix 2

Equations for optical surfaces *

meridional cylinder:
$x^2+y^2-2Rx=0$
sagittal cylinder:
$x^2+z^2-2\rho x=0$
sphere:
$x^2+y^2+z^2-2Rx=0$
toroid:
$x^2+y^2+z^2-2Rx+2R(R-\rho)-2(R-\rho)\left[(R-x)^2+y^2\right]^{1/2}=0$
paraboloid:
$x^2 cos^2\theta_B + y^2 sin^2\theta_B + z^2 - 2yz\,sin\theta_B cos\theta_B - 4xr_b sin\theta_B = 0$
ellipsoid:
$\left[\frac{cot^2\theta_B}{r_a r_b}+\frac{4}{(r_a+r_b)^2}\right]x^2+\left[\frac{1}{r_a r_b}\right]y^2+\left[\frac{1}{r_a r_b sin^2\theta_B}\right]z^2$ $-x\left[\frac{4}{(r_a+r_b)\,sin\theta_B}\right]+xy\left[2cot\theta_B\left(\frac{1}{r_a}-\frac{1}{r_b}\right)\left(\frac{1}{r_a+r_b}\right)\right]=0$

* Equations for optical surfaces in the local reference frame as defined in fig. 3.1

Appendix 3

"Noda" coefficients for optical surfaces *

	meridional cylinder	sagittal cylinder	sphere	toroid	paraboloid	ellipsoid
a_{20}	$\frac{1}{2R}$	0	$\frac{1}{2R}$	$\frac{1}{2R}$	$\frac{\sin\theta_B}{f}$	$\frac{\sin\theta_B}{4f}$
a_{02}	0	$\frac{1}{2\rho}$	$\frac{1}{2R}$	$\frac{1}{2\rho}$	$\frac{1}{4f\sin\theta_B}$	$\frac{1}{4f\sin\theta_B}$
a_{12}	0	0	0	0	$\frac{-\cot\theta_B}{8f^2}$	$\frac{-\cot\theta_B}{8f^2}\left[\frac{r_a - r_b}{r_a + r_b}\right]$
a_{22}	0	0	$\frac{1}{4R^2}$	$\frac{1}{4R^2\rho}$	$\frac{3\cos^2\theta_B}{32f^3\sin\theta_B}$	$\frac{\cos^2\theta_B}{16f^3\sin\theta_B}\left[\frac{3}{2} - \frac{4f^2}{r_a r_b}\left(1 - \frac{\tan^2\theta_B}{2}\right)\right]$
a_{30}	0	0	0	0	$\frac{-\sin\theta_B\cos\theta_B}{8f^2}$	$\frac{-\cot\theta_B}{8f^2\sin^2\theta_B}\left[\frac{r_a - r_b}{r_a + r_b}\right]$
a_{04}	0	$\frac{1}{8\rho^3}$	$\frac{1}{8R^3}$	$\frac{1}{8\rho^3}$	$\frac{\cos^2\theta_B}{64f^3\sin^3\theta_B}$	$\frac{1}{64f^3\sin^3\theta_B}\left[\cos^2\theta_B + \frac{4f^2}{r_a r_b}\sin^2\theta_B\right]$
a_{40}	$\frac{1}{8R^3}$	0	$\frac{1}{8R^3}$	$\frac{1}{8R^3}$	$\frac{5\sin\theta_B\cos^2\theta_B}{64f^3}$	$\frac{\sin\theta_B}{64f^3}\left[5\cos^2\theta_B + \frac{4f^2}{r_a r_b}(1 - 5\cos^2\theta_B)\right]$

* The coefficients for optical surfaces as determined according to section 3.2.2

Appendix 4

The total light path function

$$\mathbf{AP + PB} = r_a + r_b \qquad] T_0$$

$$-y\,(sin\alpha + sin\beta) \qquad] T_1$$

$$\left.\begin{aligned}
&\frac{1}{2}\left[\frac{cos^2\alpha}{r_a} - 2a_{20}cos\alpha\right]y^2 + \frac{1}{2}\left[\frac{cos^2\beta}{r_b} - 2a_{20}cos\beta\right]y^2 \\
&\frac{1}{2}\left[\frac{sin\alpha}{r_a}\left(\frac{cos^2\alpha}{r_a} - 2a_{20}cos\alpha\right) - 2a_{30}cos\alpha\right]y^3 \\
&\frac{1}{2}\left[\frac{sin\beta}{r_b}\left(\frac{cos^2\beta}{r_b} - 2a_{20}cos\beta\right) - 2a_{30}cos\beta\right]y^3 \\
&\frac{1}{2}\left[\frac{sin^2\alpha}{r_a^2}\left(\frac{cos^2\alpha}{r_a} - 2a_{20}cos\alpha\right) - \frac{sin\alpha}{r_a}(2a_{30}cos\alpha)\right]y^4 \\
&\frac{1}{2}\left[\frac{sin^2\beta}{r_b^2}\left(\frac{cos^2\beta}{r_b} - 2a_{20}cos\beta\right) - \frac{sin\beta}{r_b}(2a_{30}cos\beta)\right]y^4
\end{aligned}\right\} T_2$$

$$\left.\begin{aligned}
&\frac{1}{2}\left[\frac{1}{r_a} - 2a_{02}cos\alpha\right]z^2 + \frac{1}{2}\left[\frac{1}{r_b} - 2a_{02}cos\beta\right]z^2 \\
&\frac{1}{2r_a}[z_a^2 - 2zz_a] + \frac{1}{2r_b}[z_b^2 - 2zz_b] \\
&-\frac{1}{8r_a}\left[(\frac{1}{r_a} - 2a_{02}r_a cos\alpha)\,z^2 + \frac{1}{r_a}(z_a^2 - 2zz_a)\right]^2
\end{aligned}\right\} T_3$$

Appendix 4

$$-\frac{1}{8r_b}\left[\left(\frac{1}{r_b}-2a_{02}r_b\cos\beta\right)z^2+\frac{1}{r_b}\left(z_b^2-2zz_b\right)\right]^2 \qquad \Big\} T_3$$

$$\frac{1}{2}\frac{\sin\alpha}{r_a}\left[\frac{1}{r_a}-2a_{02}\cos\alpha\right]yz^2+\frac{1}{2}\frac{\sin\beta}{r_b}\left[\frac{1}{r_b}-2a_{02}\cos\beta\right]yz^2$$

$$-\left[a_{12}\cos\alpha\right]yz^2-\left[a_{12}\cos\beta\right]yz^2$$

$$\frac{1}{2}\frac{\sin\alpha}{r_a^2}\left[z_a^2-2zz_a\right]y+\frac{1}{2}\frac{\sin\beta}{r_b^2}\left[z_b^2-2zz_b\right]y$$

$$\frac{1}{2}\frac{\sin^2\alpha}{r_a^3}\left[z_a^2-2zz_a\right]y^2+\frac{1}{2}\frac{\sin^2\beta}{r_b^3}\left[z_b^2-2zz_b\right]y^2 \qquad \Big\} T_4$$

$$\frac{1}{2}\frac{\sin^2\alpha}{r_a^2}\left[\frac{1}{r_a}-2a_{02}\cos\alpha\right]y^2z^2+\frac{1}{2}\frac{\sin^2\beta}{r_b^2}\left[\frac{1}{r_b}-2a_{02}\cos\beta\right]y^2z^2$$

$$\frac{1}{2}\frac{\sin\alpha}{r_a}\left[-2a_{12}\cos\alpha\right]y^2z^2+\frac{1}{2}\frac{\sin\beta}{r_b}\left[-2a_{12}\cos\beta\right]y^2z^2$$

$$\frac{1}{2}\left[\frac{a_{20}^2}{r_a}-2a_{40}\cos\alpha\right]y^4+\frac{1}{2}\left[\frac{a_{20}^2}{r_b}-2a_{40}\cos\beta\right]y^4$$

$$\frac{1}{2}\left[\frac{a_{02}^2}{r_a}-2a_{04}\cos\alpha\right]z^4+\frac{1}{2}\left[\frac{a_{02}^2}{r_b}-2a_{04}\cos\beta\right]z^4 \qquad \Big\} T_5$$

$$\left[\frac{a_{20}\cdot a_{02}}{r_a}-a_{22}\cos\alpha\right]y^2z^2+\left[\frac{a_{20}\cdot a_{02}}{r_b}-a_{22}\cos\beta\right]y^2z^2$$

Appendix 5

Design parameters of the Daresbury photon microprobe

Horizontal object size	2 mm
Vertical object size	0.3 mm
Horizontal source divergence	4 mrad
Vertical source divergence (15 keV)	0.075 mrad
Object distance	80 m
Image distance	0.38 m
Magnification	1/210
Semimajor axis of the ellipsoid	40.19 m
Semiminor axis of the ellipsoid	0.72 m
Eccentricity of the ellipsoid	0.999835
Local sagittal radius of curvature	0.1 m
Local meridional radius of curvature	5.74 m
Crystal material and reflection planes	Si(111)
2d-spacing	0.627 nm
Bragg angle	7.57°
Darwin width, flat Si(111)	3.7″
Darwin width, bent Si(111)	6.6″
Extinction length, flat Si(111)	11.6 μm
$\Delta E/E$, flat Si(111)	$1.31\ 10^{-4}$
Operating energy and calculated bandwidth	15.0/0.3 keV
Available 15 keV fluxdensity at 80 m	$3.2\ 10^{5}$
(per area slit opening)	ph/(s.mA.100eV.mm^2)
Crystal dimension	diam 60 mm
Crystal thickness	100 μm
Crystal substrate material	Aluminium
Shape accuracy (over 30 mm in the centre)	<1 μm

Appendix 6

Physical data of Silicon *

property	symbol	quantity	unit
atomic number	A	14	-
density @20 °C	ρ	2.34	g cm^{-3}
hardness	H	7.0	Mohs
elastic constants @Poisson's ratio: $\nu = c_{12}/(c_{11}+c_{12})$	c_{11} c_{12} c_{44}	167.4 65.2 79.6	GPa GPa GPa
temperature coefficients of elastic constants	dc_{11}/dT dc_{12}/dT dc_{44}/dT	-75.0×10^{-5} -24.5×10^{-5} -55.5×10^{-5}	Pa K^{-1} Pa K^{-1} Pa K^{-1}
Young's modulus	Y_1	190	GPa
thermal conductivity	κ	157	W m^{-1} K^{-1}
coefficients of linear thermal expansion	κ'	2.33×10^{-6}	K^{-1}
inter planar spacing	d	0.31355	nm
volume of the unit cell	v_0	0.16	nm^3
Debye-Waller factor	F_x	16.7×10^{-12}	cm
linear attenuation coefficient @15 keV	μ_0	23	cm^{-1}
extinction length @15 keV	l_{ext}	11.6	µm
extinction thickness @15 keV	t_{ext}	1.53	µm
absorption thickness @15 keV	t_{abs}	28.6	µm
energy resolution	$\Delta E/E$	1.31×10^{-4}	-
Darwin width @15 keV @(111)	$\Delta\theta$	3.6	arcsec

* data taken from [Kui 83, Suo 86, Goo 87, Fre 88], where relevant for reflection planes (111)

Appendix 7

Derivation of the equation of the 15 keV ellipsoidal crystal

In general, it is more convenient for synchrotron focussed beam applications to change the system of coordinates from one in which the ellipsoid is defined as a revolution of an ellipse around the x-axis, to the local system of coordinates of the focussing crystal (see fig. A1).

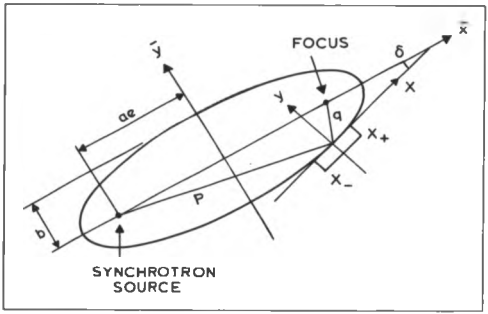

Fig. A1 Diagram of the elliptical focussing geometry

For convenience the plane tangent to the ellipsoid in $(\bar{x}_0, \bar{y}_0, 0)$ tilted at angle δ to the horizontal incident beam is considered, because of rotation symmetry of the ellipsoid in the (y, z)-plane, so the equation of the ellipsoid as referred to the tangent plane is:

$$\frac{(x\cos\delta - y\sin\delta + \bar{x}_0)^2}{a^2} + \frac{(x\sin\delta + y\cos\delta - \bar{y}_0)^2}{b^2} + \frac{z^2}{b^2} = 1 \qquad \text{(A.1)}$$

or

$$Ax^2 + By^2 + Cz^2 + Dxy + Ex + Fy = 0 . \tag{A.2}$$

where

$$A = \frac{cos^2\delta}{a^2} + \frac{sin^2\delta}{b^2} , \tag{A.3}$$

$$B = \frac{sin^2\delta}{a^2} + \frac{cos^2\delta}{b^2} , \tag{A.4}$$

$$C = \frac{1}{b^2} , \tag{A.5}$$

$$D = 2cos\delta sin\delta\left(\frac{1}{b^2} - \frac{1}{a^2}\right) , \tag{A.6}$$

$$E = 2\left(\frac{\bar{x}_0 cos\delta}{a^2} - \frac{\bar{y}_0 sin\delta}{b^2}\right) , \tag{A.7}$$

$$F = -2\left(\frac{\bar{x}_0 sin\delta}{a^2} + \frac{\bar{y}_0 cos\delta}{b^2}\right) . \tag{A.8}$$

The position on the ellipsoid is known, when the major axis a, the minor axis b and the tilt angle δ are given, except for the position in the (y, z)-plane because of rotation symmetry.

From the experimental setup the parameters (a, b, δ) are not directly known, and therefore (p, q, θ) are more convenient parameters, where p is the major distance from the source to the crystal, q the minor distance from the crystal to the focus, and θ the Bragg angle. The distance p is fixed by the distance from the experimental hutch to the SR source, which is 80 m. The Bragg angle is fixed by the choice of the crystal, the reflecting planes and the excitation energy, which is 7.57°, as discussed in section 4.4.2.

The distance q is set by the minimum acceptable radius of curvature of the crystal. The radius is fixed at 10 cm. With the expression of sagittal focussing (see section 3.2.2):

$$\frac{1}{p} + \frac{1}{q} = \frac{2\sin\theta}{R_s} , \tag{A.9}$$

there follows q = 38 cm. Now the transformation T: (p, q, θ) → (a, b, δ) can be performed by:

$$a = \frac{1}{2}(p+q) = 40.19 , \tag{A.10}$$

$$b = \sin\theta\sqrt{pq} = 0.72892227 , \tag{A.11}$$

$$\delta = a\tan\left(\frac{p-q}{p+q}\tan\theta\right) = 7.526^\circ , \tag{A.12}$$

with dimensions in m.

The final expression of the ellipsoid is thus:

$$\left[\frac{\bar{x}}{40.19}\right]^2 + \left[\frac{\bar{y}}{0.72892}\right]^2 + \left[\frac{\bar{z}}{0.72892}\right]^2 = 1 , \tag{A.13}$$

with:

$$\bar{y}_0 = R_s\cos\delta = 0.099 , \tag{A.14}$$

$$\bar{x}_0 = a\left[1 - (\bar{y}_0/b)^2\right]^{1/2} = 39.816 . \tag{A.15}$$

The height of several points on the crystal surface can be calculated from eq. A.2:

$$By^2 + (Dx + F)y + (Ax^2 + Cz^2) = 0 . \tag{A.16}$$

The equation has a solution, in the diffraction plane z = 0, which is:

$$y = \left| \frac{-(Dx + F) + [(Dx + F)^2 - 4BAx]^{1/2}}{2B} \right| , \qquad \text{(A.17)}$$

As an example: What is the heigth of the crystal at $x_+ = +2.5$ cm and $x_- = -2.5$ cm from the centre in the meridional plane? From eq. A.17 one finds: $y_+ = 60$ µm and $y_- = 53$ µm. Note that in the centre the condition for astigmatism holds:

$$\frac{Rs}{Rm} = \sin^2\theta = 0.0175 . \qquad \text{(A.18)}$$

In case of a toroid, therefore, the heigths of the crystal on the same position would be $y_+ = y_- = 55$ µm. An ellipsoid is a better focussing device than a toroid because of the decreasing sagittal radius with increasing x (see fig. A.1) rather than because of the deviation from the meridional radius. So coma will be minimized with respect to the toroid, where the sagittal radius is a constant.

References

And58 G. Andermann and J.W. Kemp, *Anal. Chem.* **Vol.34** (1958) 1306.

Ant89 A.A. Antonov, V.B. Baryshev, I.G. Grigoryeva, G.N. Kulipanov, Ya.V. Terehkov and N.N. Shipkov, *Rev. Sci. Instrum.* **60(7)** (1989) 2462.

Aok87 S. Aoki, Y. Goshi and A. Iida, in *X-ray Microscopy* ed. P.C. Cheng and G.J. Jan, Springer, Berlin (1987) 254.

Arf71 G. Arfken, *Mathematical Methods for Physicists*, Academic Press, New York and London, 1971.

Ari87 V.V. Aristov, Yu. A. Basov, S.V. Redkin, A.A. Snigirev and V.A. Yunkin, *Nucl. Instr. Meth.* **A261** (1987) 72.

Ari89a V.V. Aristov, Yu. A. Basov, G.N. Kulipanov, V.F. Pindyurin, A.A. Snigirev and A.S. Sokolov, *Nucl. Instr. Meth.* **A274** (1989) 390.

Ari88 V.V. Aristov, Bragg-Fresnel Optics in: *X-ray Microscopy II* eds. D. Sayre, M. Howells, J. Kirz and H. Rarback, Springer Verlag, Berlin, 1988.

Ari89b V.V. Aristov, Yu. A. Basov, and A.A. Snigirev, *Rev. Sci. Instr.* **60(7)** (1989) 1517.

Bar84 T.W. Barbee Jr., Multilayers for X-ray Optical Applications in: *X-ray Microscopy* eds. J. Schmahl and D. Rudolph, Springer Verlag, Berlin, 1984.

Bar86 V.B. Baryshev, G. N. Kulipanov and A.N. Skrinsky, *Nucl. Instr. Meth.* **A246** (1986) 739.

Bar89a V.B. Baryshev, N.G. Gavrilov, A.V. Daryin, K.V. Zolotarev, G.N. Kulipanov, N.A. Mezentsev and Ya.V. Terekhov, *Rev. Sci. Instrum.* **60(7)** (1989) 2456.

Bar89b V.B. Baryshev, N.G. Gavrilov, A.V. Daryin, K.V. Zolotarev, G.N. Kulipanov, N.A. Mezentsev and Ya.V. Terekhov, *Nucl. Instr. Meth.* **A282** (1989) 570.

Bat83 B.W. Batterman and L. Berman, *Nucl. Instr. Meth.* **208** (1983) 327.

Bav88 M. Bavdaz, A. Knöchel, P. Ketelsen, W. Petersen, N. Gurker, M.H. Salehi and T. Dietrich, *Nucl. Instr. Meth.* **A266** (1988) 308.

Bea74 J.H. Beaumont and M. Hart, *J. Phys.* **E7** (1974) 823.

Beu45 H.G. Beutler, *J. Opt. Soc. Am.* **35** (1945) 311.

Bil83 D.H. Bilderback, B.M. Lairson, T.W. Barbee Jr., G.E. Ice and C.J. Sparks Jr., *Nucl. Instr. Meth.* **208** (1983) 251.

Bil86 D. Bilderback, C. Henderson and C. Prior, *Nucl. Instr. Meth.* **A246** (1986) 194.

Blo75 H.P. Blok, J.C. de Lange and J.W. Schotman, *Nucl. Instr. Meth.* **128** (1975) 545.

Boe89 A. Boeuf et M. Belakhovsky, *Caracteristiques des sources de RSX sur aimant de courbure de l'ESRF*, ESRF, Grenoble, juin 1989.

Bos84a A.J.J. Bos, R.D. Vis, H. Verheul, M. Prins, S.T. Davies, D.K. Bowen, J. Makjanic´ and V. Valkovic´, *Nucl. Instr. Meth.* **B3** (1984) 232.

Bos84b A.J.J. Bos, *Ph.D. Thesis*, Free University, Amsterdam (1984).

Bro14 M. de Broglie and F.A. Lindemann, *C. R. Acad. Sci. Paris* **158** (1914) 944.

Buc70 H.A. Buchdahl, *An Introduction to Hamiltonian Optics* University Press, Cambridge, 1970.

Car89 D.A. Carpenter, M.A. Taylor and C.E. Holcombe, *Adv. X-ray Anal.* **Vol.32** (1989) 115.

Cau32a Y. Cauchois, *C. R. Acad. Sci. Paris* **194** (1932) 362.

Cau32b Y. Cauchois, *C. R. Acad. Sci. Paris* **195** (1932) 228.

Cau33 Y. Cauchois, *J. Phys. Radium* **4** (1933) 61.

Cau34 Y. Cauchois, *Ann. Phys. Paris* **1** (1934) 215.

Che84a J.R. Chen, B.M. Gordon, A.L. Hanson, K.W. Jones, H.W. Kraner, E.C.T. Chao and J.A. Minkin, *Scan. El. Micros.* **IV** (1984) 1483.

Che84b J.R. Chen, N. Martijs, E.C.T. Chao, J.A. Minkin, C.L. Thompson, A.L. Hanson, H.W. Kraner, K.W. Jones, B.M. Gordon and R.E. Mills, *Nucl. Instr. Meth.* **B3** (1984) 241.

Che87 J.R. Chen, E.C.T. Chao, J.A. Minkin, J.M. Back, W.C. Bagby, M.L. Rivers, S.R. Sutton, B.M. Gordon, A.L. Hanson and K.W. Jones, *Nucl. Instr. Meth.* **B22** (1987) 394.

Cho86 J. Chomilier, G. Loupias and J. Felsteiner, *Nucl. Instr. Meth.* **B14** (1986) 38.

Coo73 J. Cooper, *Nucl. Instr. Meth.* **106** (1973) 525.

Cos60 V.E. Cosslett and W.C. Nixon, *X-ray microscopy*, Cambridge, 1960.

Cul62 T.J. Cullen, *Anal. Chem.* **Vol.34** (1962) 812.

Cur68 L.A. Currie, *Anal. Chem.* **Vol.40** (1968) 586.

Des80 R.D. Deslattes, *Nucl. Instr. Meth.* **172** (1980) 201.

Dhe89 P. Dhez, *Nucl. Instr. Meth.* **A282** (1989) 519.

Dri78 W.G. Driscoll and W. Vaughan, *Handbook of Optics*, Mc Graw-Hill, New York, 1978.

Duk90 P.J. Duke, Chap. 12 in: *Applications of Synchrotron Radiation* eds. C.R.A. Catlow and G.N. Greaves, Blackie, Glasgow and London, 1990.

Ehr47 W. Ehrenberg, *Nature* **160** (1947) 330.

Ehr49 W. Ehrenberg, *J. Opt. Soc. Am.* **39** (1949) 741.

Esp79 P. van Espen, L. van 't Dack, F. Adams and R. van Grieken, *Anal. Chem.* **Vol.51** (1979) 961.

Fel75 J. Felsteiner and P. Pattison, *Nucl. Instr. Meth.* **124** (1975) 449.

Fra77 A. Franks, *Sci. Prog. Oxf.* **64** (1977) 371.

Fra88 J.D. Frantz, H.K. Mao, Y.-G. Zhang, Y. Wu, A.C. Thompson, J.H. Underwood, R.D. Giauque, K.W. Jones and M.L. Rivers, *Chem. Geo.* **69** (1988) 235.

Fre81 C.J. Frederickson, M.H. Frederickson and G.A. Howell, *Exp. Neurol.* **73** (1981) 812.

Fre83 A.K. Freund, *Nucl. Instr. Meth.* **A216** (1983) 269.

Fre88 A.K. Freund, *Nucl. Instr. Meth.* **A266** (1988) 461.

Ful89 J.E. Fulghum, G.E. McGuire, I.H. Musselman, R.J. Nemanich, J.M. White, D.R. Chopra and A.R. Chourasia, *Anal. Chem.* **Vol.61** (1989) 243R.

Gia88 R.D. Giauque, A.C. Thompson, J.H. Underwood, Y. Wu, K.W. Jones and M.L. Rivers, *Anal. Chem.* **60** (1988) 385.

Gla80 E.S. Gladney, *Anal. Chim. Acta* **118** (1980) 855.

Goo87 Goodfellow, *Catalogue* 8 (1987-88) 245.

Gor82 B.M. Gordon, *Nucl. Instr. Meth.* **204** (1982) 223.

Gor83 B.M. Gordon, *Neurotoxicology* No.3, **4** (1983) 13.

Gor85 B.M. Gordon and K.W. Jones, *Nucl. Instr. Meth.* **B10/11** (1985) 293.

Gor87 B.M. Gordon, K.W. Jones and A.L. Hanson, *SPIE* **Vol.681** (1987) 102.

Gor90 B.M. Gordon, A.L. Hanson, K.W. Jones, J.G. Pounds, M.L. Rivers, G. Schidlovsky, P. Spanne and S.R. Sutton, *Nucl. Instr. Meth.* **B45** (1990) 527.

Gos87 Y. Goshi, A. Aoki, A. Iida, S. Hayakawa, H. Yamaji and K. Sakurai, *Jpn. J.*

Appl. Phys. **26** (1987) L.1260.

Gos88 Y. Goshi, S. Aoki, A. Iida, S. Hayakawa, H. Yamaji and K. Sakurai, *Adv. X-ray Anal.* **Vol.31** (1988) 495.

Gou16 G. Gouy, *Ann. Phys.* **5** (1916) 241.

Gra87 M. Grasserbauer, *Anal. Chim. Acta* **195** (1987) 1.

Gro83 L. Grodzins, *Neurotoxicology* No.3, **4** (1983) 23.

Gur87 N. Gurker, *Adv. X-Ray Anal.* **Vol.30** (1987) 53.

Hab50 H. Haber, *J. Opt. Soc. Am.* **40** (1950) 153.

Ham32 L. von Hámos, *Naturwiss.* **20** (1932) 705.

Ham33 L. von Hámos, *Nature* **134** (1933) 181.

Ham39 L. von Hámos, *Z. Kristallographie* **101** (1939) 2.

Hay89a S. Hayakawa, A. Iida, S. Aoki and Y. Goshi, *Adv. X-ray Anal.* **Vol.32** (1989).

Hay89b S. Hayakawa, A. Iida, S. Aoki and Y. Goshi, *Rev. Sci. Instr.* **60(7)** (1989) 2456.

Hea82 S.M. Heald, *Nucl. Instr. Meth.* **195** (1982) 59.

Het86 M.C. Hettrick, *Appl. Opt.* **25** (1986) 3269.

Hor72 P. Horowitz and J.A. Howell, *Science* **178** (1972) 608.

How75 J.A. Howell and P. Horowitz, *Nucl. Instr. Meth.* **125** (1975) 225.

Hws83 M.R. Howells and J.B. Hastings, *Nucl. Instr. Meth.* **208** (1983) 379.

Hub75 J.M. Hubbel, W.M.J. Veigele, E.A. Briggs, R.T. Brown, D.T. Cramer and R.J. Howerton, *J. Phys. Chem. Ref. Data* **4** (1975) 471.

Hub83 H.J. Hubbard and E. Pantos, *Nucl. Instr. Meth.* **208** (1983) 319.

Ice84 G.E. Ice and C.J. Sparks Jr., *Nucl. Instr. Meth.* **222** (1984) 121.

Ice88 G.E. Ice and C.J. Sparks Jr., *Nucl. Instr. Meth.* **266** (1988) 394.

Jac89 L.L. Jackson, D.M. McKown, J.E. Taggert Jr., P.J. Lamothe and F.E. Lichte, *Anal. Chem.* **Vol.61** (1989) 109R.

Jen29 F. Jentzsch, *Phys. Zeit.* **30** (1929) 268.

Jen85 T.J.J.M. Jennekens, *Internal Report*, Eindhoven University of Technology, VDF-NK-85-45.

Joh31 H.H. Johann, *Z. Physik* **69** (1931) 185.

Jon84 K.W. Jones, B.W. Gordon, A.L. Hanson, J.B. Hastings, M.R. Howells, H.W. Kraner and J.R. Chen, *Nucl. Instr. Meth.* **B3** (1984) 225.

Jon87 K.W. Jones, P.Z. Takacz, J.B. Hastings, J.M. Casstevens and C.D. Poinke, *SPIE* **Vol.179** (1987) 37.

Jon89 K.W. Jones and B.M. Gordon, *Anal. Chem.* **Vol.61** (1989) 341A.

Khv87 V.P. Khvostova and V.A. Trunova, *Nucl. Instr. Meth.* **A261** (1987) 293.

Kir48 P. Kirkpatrick and A.V. Baez, *J. Opt. Soc. Am.* **38** (1948) 766.

Kiz74 J. Kirz, *J. Opt. Soc. Am.* **64** (1974) 301.

Kiz78 J. Kirz, D. Sayre and J. Dilger, *Ann. N. Y. Acad. Sci.* **306** (1978) 291.

Kiz80 J. Kirz and D. Sayre, *Chap. 14 in: Synchrotron Radiation Research* eds. H. Winick and S. Doniach, Plenum, New York, 1980.

Kub79 H. Kubo and W.R. Smythe, *Anal. Chem.* **Vol.51**, no.8 (1979) 1194.

Kui83 J.M. Kuiper, *Internal Report*, Eindhoven University of Technology, VDF-NK-83-29.

Lai86a B. Lai, F. Cerrena and M. Pouey, *Nucl. Instr. Meth.* **A246** (1986) 297.

Lai86b B. Lai and F. Cerrena, *Nucl. Instr. Meth.* **A246** (1986) 337.

Lai88 B. Lai, K. Chapman and F. Cerrena, *Nucl. Instr. Meth.* **A266** (1988) 544.

Lan87 F. van Langevelde, W.J.M. Lenglet, R.M.W. Overwater, R.D. Vis, A. Huizing, M.P.A. Viegers, C.P.G.M. Zegers and J.A. van der Heide, *Nucl. Instr. Meth.* **A257** (1987) 436.

Lan89a F. van Langevelde, G.H.J. Tros and R.D. Vis, *J. Trace Micropr. Techn.* **Vol.7**, No.4 (1989-90) 247.

Lan89b F. van Langevelde, D.K. Bowen, G.H.J. Tros and R.D. Vis, *Proc. XIIth Int. Con. on X-ray Optics and Microanalysis* Cracow, Poland (1989).

Lan90a F. van Langevelde, D.K. Bowen, G.H.J. Tros, R.D. Vis, A. Huizing and D.K.G. de Boer, *Nucl. Instr. Meth.* **A292** (1990) 719.

Lan90b F. van Langevelde, G.H.J. Tros, D.K. Bowen and R.D. Vis, *Nucl. Instr. Meth.* **B49** (1990) 544.

Len85 W.J.M. Lenglet, F. van Langevelde, A.J.J. Bos, R.D. Vis and H. Verheul, *Spectrochimica Acta* **Vol.40B** (1985) 763.

Len87 W.J.M. Lenglet, R.D. Vis, F. van Langevelde and H. Verheul, *Anal. Chim. Acta* **195** (1987) 153.

Len88 W.J.M. Lenglet, *Ph.D. Thesis*, Free University, Amsterdam (1988).

Lya90 D.M. Lyaruu, G.H.J. Tros, A.L.J.J. Brouckers and J.H.M. Wöltgens, *Scan. Micr.* **Vol.4**, No.2 (1990) 315.

Mey72 J.R. Meyer-Arendt, *Introduction to Classical and Modern Optics*, Prentice Hall, London, 1972, 198-203.

Mik74 J. Mika and T. Török, *Analytical Emission Spectroscopy*, Butterworths, London, 1974.

Mil80 J. Miltat, *in: Characterization of Crystal Growth Defects by X-ray Methods*, eds. B.K. Tanner and D.K. Bowen, Plenum, New York, 1980.

Mil86 D.M. Mills, C. Henderson and B.W. Batterman, *Nucl. Instr. Meth.* **A246** (1986) 356.

Mou88 S. Mourikis, E.E Koch and V. Saile, *Nucl. Instr. Meth.* **A267** (1988) 218.

Nam61 T. Namioka, *J. Opt. Soc. Am.* **51** (1961) 4,13.

Nod74 H. Noda, T. Namioka and M. Seya, *J. Opt. Soc. Am.* **64** (1974) 1031.

Pan83 E. Pantos, *Nucl. Instr. Meth.* **208** (1983) 449.

Pet84 W. Petersen, *Internal Report Desy F41* Hasylab **84-02** (1984).

Pet86 W. Petersen, P. Ketelsen, A. Knöchel and R. Pausch, *Nucl. Instr. Meth.* **A246** (1986) 731.

Pia88 P. Pianetta and T.W. Barbee Jr., *Nucl. Instr. Meth.* **A266** (1988) 441.

Pri83 M. Prins, J.A. van der Heide, A.J.J. Bos, D.K. Bowen and S.T. Davies, *IEEE Trans. Nucl. Sci.* **Vol. NS-30**, No.2 (1983) 1243.

Pri84a M. Prins, S.T. Davies and D.K. Bowen, *Nucl. Instr. Meth.* **222** (1984) 324.

Pri84b M. Prins, J.M. Kuipers and M.P.A. Viegers, *Nucl. Instr. Meth.*, **B3** (1984) 246.

Pro78 Proc. of the Int. Conf. on Synchrotron Rad. Instr. and New Devel., *Nucl. Instr. Meth.* **152** (1978).

Red87 "Red Book", ESRF, *Foundation Phase Report*, Grenoble, Febr. 1987.

Rei85 C.J. Reinhoudt, *Internal Report*, Eindhoven University of Technology, VDF-NK-85-27.

Rie89 C. Riekel, *Synchr. Rad. News* **Vol.2**, No.1 (1989) 9.

Riv89 M.L. Rivers, S.R. Sutton and B.M. Gordon, *Mat. Res. Soc. Symp. Proc.* **Vol.143** (1989) 285.

Rob68 B.W. Roberts and W. Parrish, *International Tables for X-ray Crystallography*,

Birmingham, 1968.

Roh14 H. Rohmann, *Phys. Z.* **15** (1914) 510.

Rus85 J.C. Russ, *Adv. X-ray Anal.* **Vol.28** (1985) 11.

Sai88 K. Saitoh, K. Inagawa, K. Kohra, C. Hayashi, A. Iida and N. Kato, *Jap. J. Appl. Phys.* **Vol.27**, No.11 (1988) L2131.

Sai89a V. Saile, in: *Workshop in Cooling of X-ray Monochromators on high Power Beam Lines*, eds. T. Matsushita and T. Ishikawa, KEK Report 88-15, 1989.

Sai89b K. Saitoh, K. Inagawa, K. Kohra, C. Hayashi, A. Iida and N. Kato, *Rev. Sci. Instr.* **60(7)** (1989) 1519.

Sch84 G. Schmahl and D. Rudolph, *X-ray Microscopy* Springer Verlag, Berlin, 1984.

Sha86 T.J. Shaffner, *Scanning Electron Microscopy* **I** (1986) 11.

Spa77 C.J. Sparks Jr., S. Raman, H.L. Yakel, R.V. Gentry and M.O. Krause, *Phys. Rev. Lett.* **38** (1977) 205.

Spa79a C.J. Sparks Jr., S. Raman, E. Ricci, R.V. Gentry and M.O. Krause, *Phys. Rev. Lett.* **40** (1979) 507.

Spa79b C.J. Sparks Jr., S. Raman, E. Ricci, M.O. Krause and R.V. Gentry, *IEEE Trans. Nucl. Sci.* **Vol. NS-26**, No.1 (1979) 1368.

Spa80a C.J. Sparks, Chap. 14 in: *Synchrotron Radiation Research* eds. H. Winick and S. Doniach, Plenum, New York, 1980.

Spa80b C.J. Sparks Jr., B.S. Boric and J.S. Hastings, *Nucl. Instr. Meth.* **172** (1980) 237.

Spa82 C.J. Sparks Jr., G.E. Ice, J. Wong and B.W. Batterman, *Nucl. Instr. Meth.* **194** (1982) 73.

Spe62 G.H. Spencer and R.K. Murty, *J. Opt. Soc. Am.* **52** (1962) 672.

Sto70 E. Storm and H.I. Israel, *Nuclear Data Tables* **Vol.7**, no.6 (1970) 565.

Suo86 P. Suortti, P.Pattison and W. Weyrich, *J. Appl. Cryst.* **19** (1986) 336.

Tho87 A.C. Thompson, Y. Wu, J.H. Underwood and T.W. Barbee Jr., *Nucl. Instr. Meth.* **A255** (1987) 603.

Tho88 A.C. Thompson, J.H. Underwood, Y. Wu, R.D. Giauque, K.W. Jones and M.L. Rivers, *Nucl. Instr. Meth.* **A266** (1988) 318.

Tho89 A.C. Thompson, J.H. Underwood, Y. Wu, R.D. Giauque, M.L. Rivers and R.

Futernick, *Adv. X-ray Anal.* **Vol.32** (1989) 149.

Tro90 G.H.J. Tros, F. van Langevelde and R.D. Vis, *Nucl. Instr. Meth.* **B50** (1990) 343.

Und81 J.H. Underwood and T.W. Barbee Jr., *Appl. Opt.* **20** (1981) 3027.

Und86 J.H. Underwood, T.W. Barbee Jr. and C. Frieber, *Appl. Opt.* **25** (1986) 1730.

Und88 J.H. Underwood, A.C. Thompson, Y. Wu and R.D. Giauque, *Nucl. Instr. Meth.* **A266** (1988) 296.

Vis88 R.D. Vis, *Scan. Micr.* **Vol.2**, no.2 (1988) 977.

Vis90a R.D. Vis and F. van Langevelde, *Proc. 3rd Int. Conf. on Nucl. Micropr. Techn. and Appl.*, Melbourne, Australia (1990), *Nucl. Instr. Meth.* **B54** (1991) 417.

Vis90b R.D. Vis, G.H.J Tros and F. van Langevelde, *Int. J. PIXE* **Vol.1**, No.1 (1990) 31.

Vis90c R.D. Vis, Chap. 13 in: *Applications of Synchrotron Radiation* eds. C.R.A. Catlow and G.N. Greaves, Blackie, Glasgow, (1990) 311-332.

Wen87 J. Wensink, W.J.M. Lenglet, R.D. Vis, C.J. van den Hamer, *Histochemistry* **87** (1987) 65.

Whi50 J.E. White, *J. Appl. Phys.* **21** (1950) 855.

Wit80 D.B. Wittry, *Electron Microscopy* **Vol.3** (1980) 14.

Wit89 D.B. Wittry, D.M. Golijanin and S. Sun, *Proc. of the XIIth Int. Con. on X-ray Optics and Microanalysis* Cracow, Poland (1989).

Wol52 H. Wolter, *Ann. Phys.* **10** (1952) 94.

List of publications

1. W.J.M. Lenglet, R.D. Vis, F. van Langevelde and H. Verheul, Bulk and microprobe analysis for trace elements with synchrotron radiation, *Anal. Chim. Acta* **195** (1987) 153.
2. F. van Langevelde, W.J.M. Lenglet, R.M.W. Overwater, R.D. Vis, A. Huizing, M.P.A. Viegers, C.P.G.M. Zegers and J.A. van der Heide, X-ray focussing for synchrotron radiation microprobe analysis at the SRS, Daresbury (UK), *Nucl. Instr. Meth.* **A257** (1987) 436.
3. F. van Langevelde, G.H.J. Tros and R.D. Vis, The assessment of the body-burden of lead by means of the analysis of human hair using synchrotron radiation X-ray fluorescence and micro-PIXE, *J. Trace Micropr. Techn.* **Vol.7**, No.4 (1989-90) 247.
4. F. van Langevelde, D.K. Bowen, G.H.J. Tros and R.D. Vis, Non-imaging optics for photon probe microanalysis at the SRS, Daresbury (UK), *Proc. XIIth Int. Con. on X-ray Optics and Microanalysis*, Cracow, Poland (1989).
5. F. van Langevelde, D.K. Bowen, G.H.J. Tros, R.D. Vis, A. Huizing and D.K.G. de Boer, Ellipsoid X-ray focussing for synchrotron radiation microprobe analysis at the SRS, Daresbury (UK), *Nucl. Instr. Meth.* **A292** (1990) 719.
6. F. van Langevelde, G.H.J. Tros, D.K. Bowen and R.D. Vis, The synchrotron radiation microprobe at the SRS, Daresbury (UK) and its applications, *Nucl. Instr. Meth.* **B49** (1990) 544.
7. G.H.J. Tros, F. van Langevelde and R.D. Vis, On the analysis of neonatal hamster tooth germs with a photon microprobe at Daresbury (UK), *Nucl. Instr. Meth.* **B50** (1990) 343.
8. R.D. Vis and F. van Langevelde, On the development of X-ray microprobes using synchrotron radiation, *Proc. 3rd Int. Conf. on Nucl. Micropr. Techn. and Appl.*, Melbourne, Australia (1990), *Nucl. Instr. Meth.* **B54** (1991) 417.
9. R.D. Vis, G.H.J. Tros and F. van Langevelde, Trace element distributions measured by a proton microprobe and a synchrotron microprobe, *Int. J. PIXE* **Vol.1**, No.1 (1990) 31.
10. F. van Langevelde and R.D. Vis, Trace element determinations using a 15 keV syn-

chrotron X-ray microprobe at the Synchrotron Radiation Source, Daresbury (United Kingdom), *accepted for publication in Anal. Chem. nov.* (1991).

11. K.H. Janssens, F. van Langevelde, F.C. Adams, R.D. Vis, S.R. Sutton, M.L. Rivers, K.W. Jones and D.K. Bowen, Comparison of Synchrotron X-ray Micro-analysis with Electron and Proton Microscopy for Individual Particle Analysis, *Pacific International Congress on X-ray Analytical Methods*, Honolulu, USA (1991).

APPENDIX D.1

Maloney murine leukemia virus complete genome

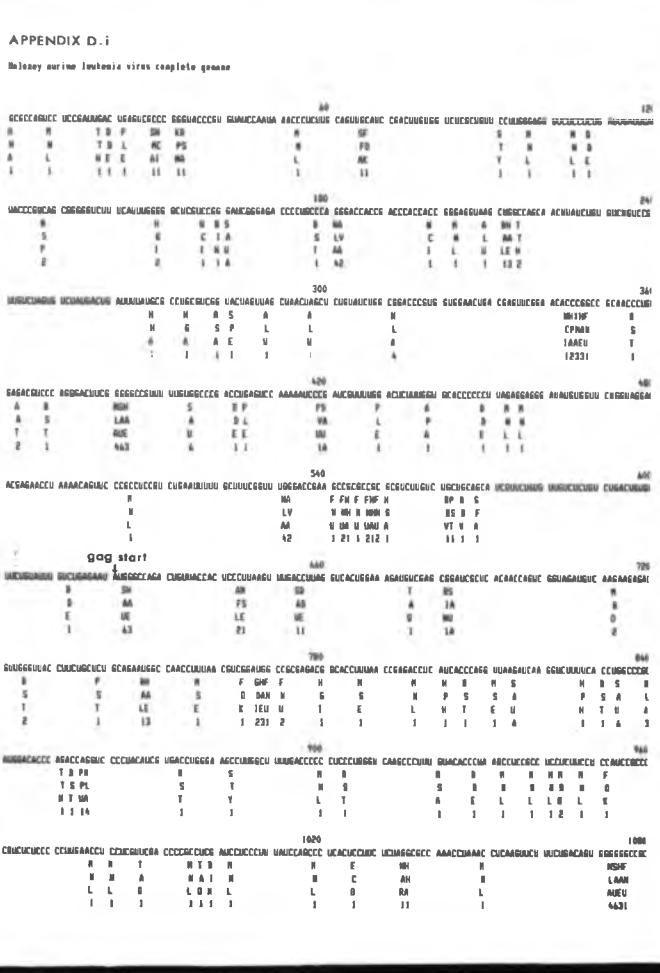

Moloney murine leukemia virus complete genome

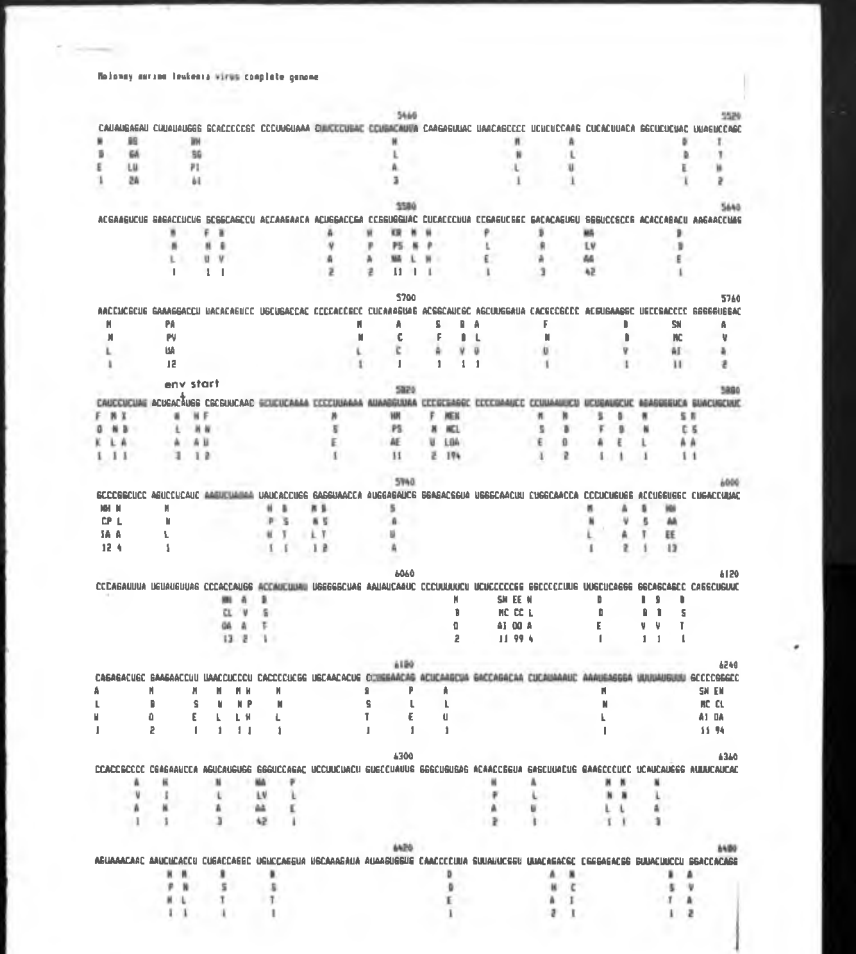

Moloney murine leukemia virus complete genome

```
                                                6540                                                6600
ACAUUACUGG GGCUUACGUU UGUAUGUCUC CGGACAAGAU CCAGGGCUUA CAUUUGGGAU CCGACUCAGA UACCAAAAUC UAGGACCCCG CGUCCCAAUA GGGCCAAACC CCGUUCUGGC
                          BH      IB  B            BB    P D          PN    FH          SH
                          SP      HI  S            AI    L D          PL    NG          AA
                          PA      ON  T            MN    E E          UA    UA          UE
                          22      21  1            11    1 1          14    21          63

                                                6660                                                6720
AGACCAACAG CCACUCUCCA AGCCCAAACC UGUUAAGUCG CCUUCAGUCA CCAAACCACC CAGUGGGACU CCUCUCUCCC CUACCCAACU UCCACCGGCG GGAACGGAAA AUAGGCUGCU
  T                       M           H   PD      P   M                       H                   B
  T                       S           P   FR      L   N                       P                   B
  H                       E           N   LA      E   L                       A                   V
  2                       1           1   13      1   1                       2                   1

                                                6780                                                6840
AAACUUAGUA GACGGAGCCU ACCAAGCCCU CAACCUCACC AGUCCUGACA AAACCCAAGA GUGCUGGUUG UGUCUAGUAG CGGGACCCCC CUACUACGAA GGGGUUGCCG UCCUGGGUAC
  D   A     N           M   M H                         T                   PN                  D   KR
  D   C     L           N   N P                         T                   PL                  S   PS
  E   C     A           L   L H                         H                   UA                  T   NA
  1   1     4           1   1 1                         2                   14                  1   11

                                                6900                                                6960
CUACUCCAAC CAUACCUCUG CUCCAGCCAA CUGCUCCGUG GCCUCCCAAC ACAAGUUGAC CCUGUCCGAA GUGACCGGAC AGGGACUCUG CAUAGGAGCA GUUCCCAAAA CACAUCAGGC
                  M                   HH  M   T       H   T                   H       P                                   ES
                  N                   AA  N   T       I   T                   P       L                                   CA
                  L                   EE  L   H       N   H                   A       E                                   OU
                  1                   13  1   2       2   1                   2       1                                   96

                                                7020                                                7080
CCUAUGUAAU ACCACCCAGA CAAGCAGUCG AGGGUCCUAU UAUCUAGUUG CCCCUACAGG UACCAUGUGG GCUUGUAGUA CCGGGCUUAC UCCAUGCAUC UCCACCACCA UACUGAACCU
                        T M  PA                    KR    N               R   N           MN S
                        A N  PV                    PS    L               S   C           LS F
                        0 L  UA                    NA    A               A   I           AI A
                        1 1  12                    11    3               1   1           31 1

                                                7140                                                7200
UACCACUGAU UAUUGUGUUC UUGUCGAACU CUGGCCAAGA GUCACCUAUC AUUCCCCCAG CUAUGUUUAC GGCCUGUUUG AGAGAUCCAA CCGACACAAA AGAGAACCGG UGUCGUUAAC
                      T     BH    P   H                A             H       XB                  H     HM
                      A     AA    L   P                L             A       HI                  P     PS
                      0     LE    E   H                U             E       ON                  A     AE
                      1     13    1   1                1             3       21                  2     11

                                                7260                                                7320
CCUGGCCCUA UUAUUGGGUG GACUAACCAU GGGGGGAAUU GCCGCUGGAA UAGGAACAGG GACUACUGCU CUAAUGGCCA CUCAGCAAUU CCAGCAGCUC CAACCCGCAG UACAGGAUGA
B  S                 NN              FN                                  BH    D           T  D A       F     R     F   S
S  A                 CL              NS                                  AA    D           T  B L       N     S     0   A
T  U                 DA              UP                                  LE    E           H  V U       U     A     K   U
1  6                 13              12                                  13    1           2  1 1       1     1     1   A

                                                7380                                                7440
UCUCAGGGAG GUUGAAAAAU CAAUCUCUAA CCUAGAAAAG UCUCUCACUU CCCUGUCUGA AGUUGUCCUA CAGAAUCGAA GGGGCCUAGA CUUGUUAUUU CUAAAAGAAG GAGGGCUGUG
D   M                                                               H   T   EGH                     M
D   N                                                               I   A   CAA                     N
E   L                                                               N   0   DUE                     L
1   1                                                               1   1   963                     1

                                                7500                                                7560
UGCUGCUCUA AAAGAAGAAU GUUGCUUCUA UGCGGACCAC ACAGGACUAG UGAGAGACAG CAUGGCCAAA UUGAGAGAGA GGCUUAAUCA GAGACAGAAA CUGUUUGAGU CAACUCAAGG
B           H               A       S               N BH            H   H       A           P H         F
B           B               V       P               L AA            N   S       L           L I         0
V           0               A       E               A LE            L   E       W           E N         K
1           2               2       1               3 13            1   1       1           1 2         1
```

Moloney murine leukemia virus complete genome

```
                                                    7620                                                                7680
AUGGUUUGAG GGACUGUUUA ACAGAUCCCC UUGGUUUACC ACCUUGAUAU CUACCAUUAU GGGACCCCUC AUUGUACUCC UAAUGAUUUU GCUCUUCGGA CCCUGCAUUC UUAAUCGAUU
      M       M    IB   S            E              PN    M     R                M    N       B     M  CT
      N       S    HI   T            C              PL    N     S                B    L       S     S  LA
      L       E    ON   Y            D              UA    L     A                D    A       M     E  AQ
      1       1    21   1            5              14    1     1                2    4       1     1  11

                                                    7740                                                                7800
AGUCCAAUUU GUUAAAGACA GGAUAUCAGU GGUCCAGGCU CUAGUUUUGA CUCAACAAUA UCACCAGCUG AAGCCUAUAG AGUACGAGCC AUAGAUAAAA UAAAAGAUUU UAUUUAGUCU
            M       E      A  B            P              H    PA               R
            S       C      V  S            L              P    VL               S
            E       D      A  T            E              H    UU               A
            1       5      2  1            1              1    21               1

                                                    7860                                                                7920
CCAGAAAAAG GGGGGAAUGA AAGACCCCAC CUGUAGGUUU GGCAAGCUAG CUUAAGUAAC GCCAUUUUGC AAGGCAUGGA AAAAUACAUA ACUGAGAAUA GAGAAGUUCA GAUCAAGGUC
                                              AN   A  AM                N               D                S
                                              LH   L  FS                L               D                A
                                              UE   U  LE                A               E                U
                                              11   1  21                3               1                A

                                                    7980                                                                8040
AGGAACAGAU GGAACAGCUG AAUAUGGGCC AAACAGGAUA UCUGUGGUAA GCAGUUCCUG CCCCGGCUCA GGGCCAAGAA CAGAUGGAAC AGCUGAAUAU GGGCCAAACA GGAUAUCUGU
            PA       SH       E              A       NH    D     SH               P A              SH       E
            VL       AA       C              L       CP    D     AA               V L              AA       C
            UU       UE       D              W       IA    E     UE               U U              UE       D
            21       63       5              1       12    1     63               2 1              63       5

                                                    8100                                                                8160
GGUAAGCAGU UCCUGCCCCG GCUCAGGGCC AAGAACAGAU GGUCCCCAGA UGCGGUCCAG CCCUCAGCAG UUUCUAGAGA ACCAUCAGAU GUUCCAGGG UGCCCCAAGG ACCUGAAAUG
      A       NH    D  SH            N       S     A          ND          I                B  HB    S  PA
      L       CP    D  AA            L       F     V          ND          B                S  GS    T  PV
      W       IA    E  UE            A       A     A          LE          A                T  IP    Y  UA
      1       12    1  63            4       1     2          11          1                1  16    1  12

                                                    8220                                                                8280
ACCCUGUGCC UUAUUUGAAC UAACCAAUCA GUUCGCUUCU CGCUUCUGUU CGCGGCUUAC UGCUCCCCGA GCUCAAUAAA AGAGCCCACA ACCCCUCACU CGGGGCGCCA GUCCUCCGAU
                                              FBFH             A  SA              H          M    A     NH       M
                                              NSNH             V  AL              G          N    V     AH       N
                                              USUA             A  CU              I          L    A     RA       L
                                              2221             1  11              2          1    1     11       1

UGACUGAGUC GCCCGGGUAC CCGUGUAUCC AAUAAACCCU CUUGCAGUUG CA
 T D P    SN  KR                 K
 T D L    NC  PS                 N
 H E E    AI  NA                 L
 1 1 1    11  11                 1
```

Moloney murine leukemia virus complete genome

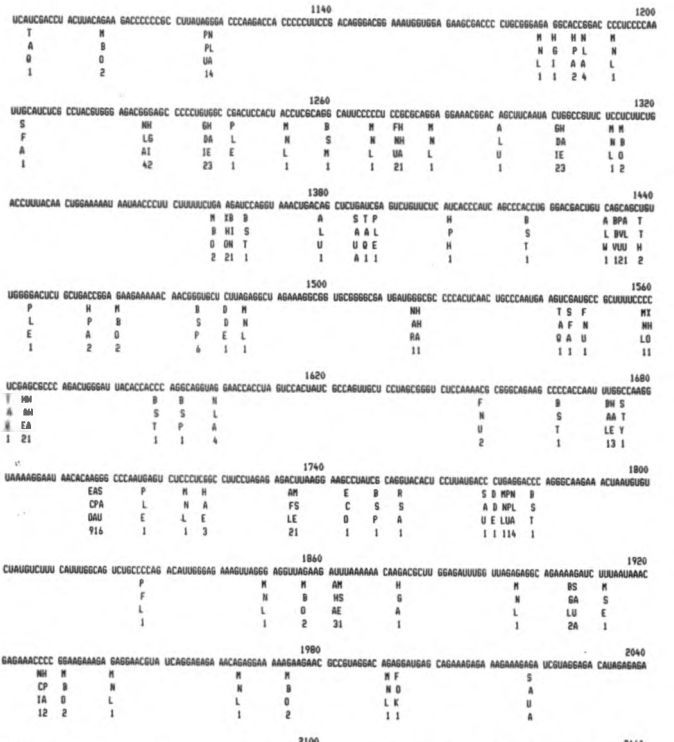

Moloney murine leukemia virus complete genome

pol start

```
                                                2220                                                                                2280
CUAAAGAUUG UCCCAAGAAA CCACGAGGAC CUCGGGGACC AAGACCCCAG ACCUCCCUCC UGACCCUAGA UGACUAGGGA GGUCAGGGUC AGGACCCCCC CCCUGAACCC AGGAUAACCC
                     MPA M A  NA              M  M                 M          PN                 B          N
                     NPV N V  LV              N  N                 N          PL                 S          N
                     LUA L A  AA              L  L                 L          UA                 T          L
                     112 1 1  42              1  1                 1          14                 1          1

                                                2340                                                                                2400
UCAAAGUCGG GGGGCAACCC GUCACCUUCC UGGUAGAUAC UGGGGCCCAA CACUCCGUGC UGACCCAAAA UCCUGGACCC CUAAGUGAUA AGUCUGCCUG GGUCCAAGGG GCUACUGGAG
                     H    B                EAS  T   D            B      B  N    D                 B N A  S                 M
                     P    S                CPA  T   R            S      S  L    D                 S L V  T                 N
                     H    T                OAU  H   A            T      T  A    E                 T A A  Y                 L
                     1    1                916  2   3            1      1  4    1                 1 4 2  1                 1

                                                2460                                                                                2520
GAAAGCGGUA UCGCUGGACC ACGGAUCGCA AAGUACAUCU AGCUACCGGU AAGGUCACCC ACUCUUUCCU CCAUGUACCA GACUGUCCCU AUCCUCUGUU AGGAAGAGAU UUGCUGACUA
                     A    BS       R        A   H       P H          M   M R                  E        M
                     V    IA       S        L   P       S P          N   L S                  C        B
                     A    NU       A        U   A       T H          L   A A                  D        O
                     2    1A       1        1   2       2 1          1   3 1                  1        2

                                                2580                                                                                2640
AACUAAAAGC CCAAAUCCAC UUUGAGGGAU CAGGAGCUCA GGUUAUGGGA CCAAUGGGGC AGCCCCUGCA AGUGUUGACC CUAAAUAUAG AAGAUGAGCA UCGGCUACAU GAGACCUCAA
                     M  BS    SA D       NA       BA           H              M      S        N   M
                     N  IA    AL D       LV       BL           I              B      F        L   N
                     L  NU    CU E       AA       VW           N              O      A        A   L
                     1  1A    11 1       42       11           2              2      1        3   1

                                                2700                                                                                2760
AAGAGCCAGA UGUUUCUCUA GGGUCCACAU GGCUGUCUGA UUUUCCUCAG GCCUGGGCGG AAACCGGGGG CAUGGGACUG GCAGUUCGCC AAGCUCCUCU GAUCAUACCU CUAAAGCAA
                     NA   N                SD  SH  D        N   N                  A  M  B S   M
                     LV   L                AD  TA  S        C   L                  L  N  C A   N
                     AA   A                UE  UE  T        I   A                  U  L  L U   L
                     42   3                11  13  1        1   3                  1  1  1 A   1

                                                2820                                                                                2880
CCUCUACCCC CGUGUCCAUA AAACAAUACC CCAUGUCACA AGAAGCCAGA CUGGGGAUCA AGCCCCACAU ACAGAGACUG UUGGACCAGG GAAUACUGGU ACCCUGCCAG UCCCCUGGA
M                    N                    BS                   A   T   A B                KR                  B
N                    L                    IA                   L   T   V S                PS                  S
L                    A                    NU                   W   H   A T                NA                  T
1                    3                    1A                   1   2   2 1                11                  1

                                                2940                                                                                3000
ACACGCCCCU GCUACCCGUU AAGAAACCAG GGACUAAUGA UUAUAGGCCU GUCCAGGAUC UGAGAGAAGU CAACAAGCGG GUGGAAGACA UCCACCCCAC CGUGCCCAAC CCUUACAACC
                     M    B                SH       BA IS  D        H              M   F            B                  M
                     S    S                TA       SL HA  D        I              B   O            S                  N
                     E    T                UE       TW OU  E        N              O   K            P                  L
                     1    1                13       11 2A  1        2              2   1            6                  1

                                                3060                                                                                3120
UCUUGAGCGG GCUCCCACCG UCCCACCAGU GGUACACUGU GCUUGAUUUA AAGGAUGCCU UUUUCUGCCU GAGACUCCAC CCCACCAGUC AGCCUCUCUU CGCCUUUGAG UGGAGAGAUC
           HN                   R        AM   FS           D   P                  M  M                    IB
           GL                   S        HS   OF           D   L                  N  B                    HI
           IA                   A        AE   KA           E   E                  L  O                    ON
           24                   1        31   11           1   1                  1  2                    21

                                                3180                                                                                3240
CAGAGAUGGG AAUCUCAGGA CAAUGGACCU GGACCAGACU CCCACAGGGU UUCAAAAACA GUCCCACCCU GUUUGAUGAG GCACUGCACA GAGACCUAGC AGACUUCCGG AUCCAGCACC
           H   D            B   A   P                                  M                                  BH BB   T
           I   O            S   V   L                                  N                                  SP AI   T
           N   E            T   A   E                                  L                                  PA MN   H
           1   1            1   2   1                                  1                                  22 11   2
```

Moloney murine leukemia virus complete genome

```
                                                
```

Moloney murine leukemia virus complete genome

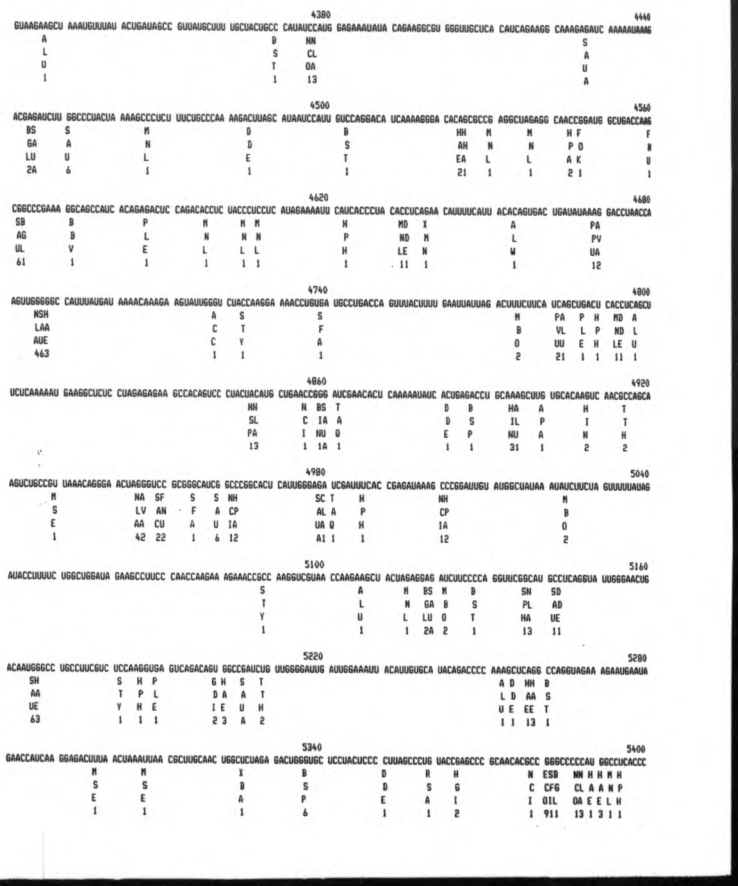

APPENDIX D. ii

AKV murine leukemia virus, complete proviral genome

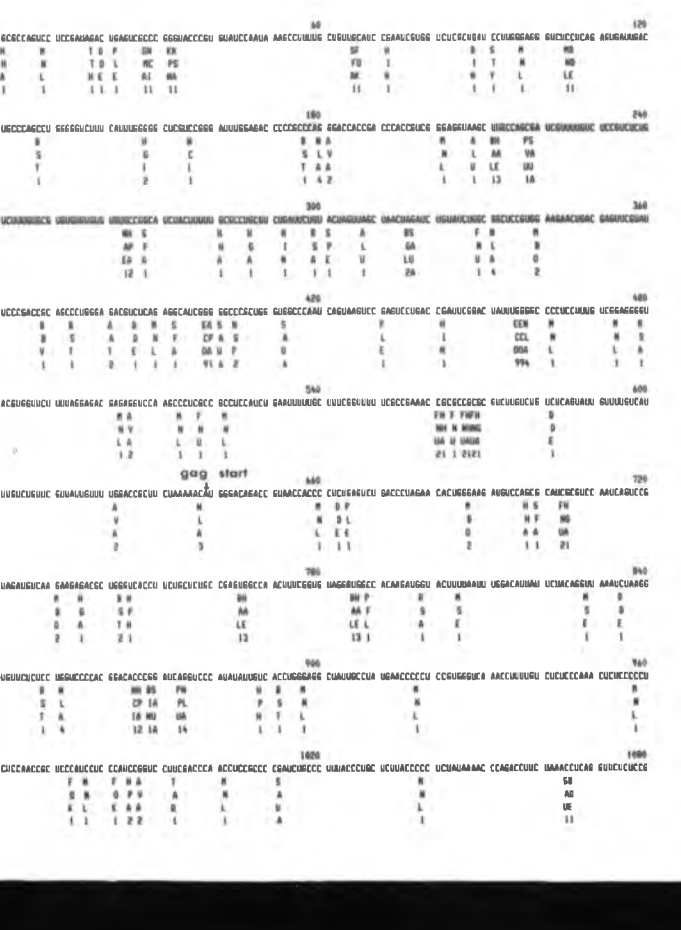

MEV murine leukemia virus, complete proviral genome

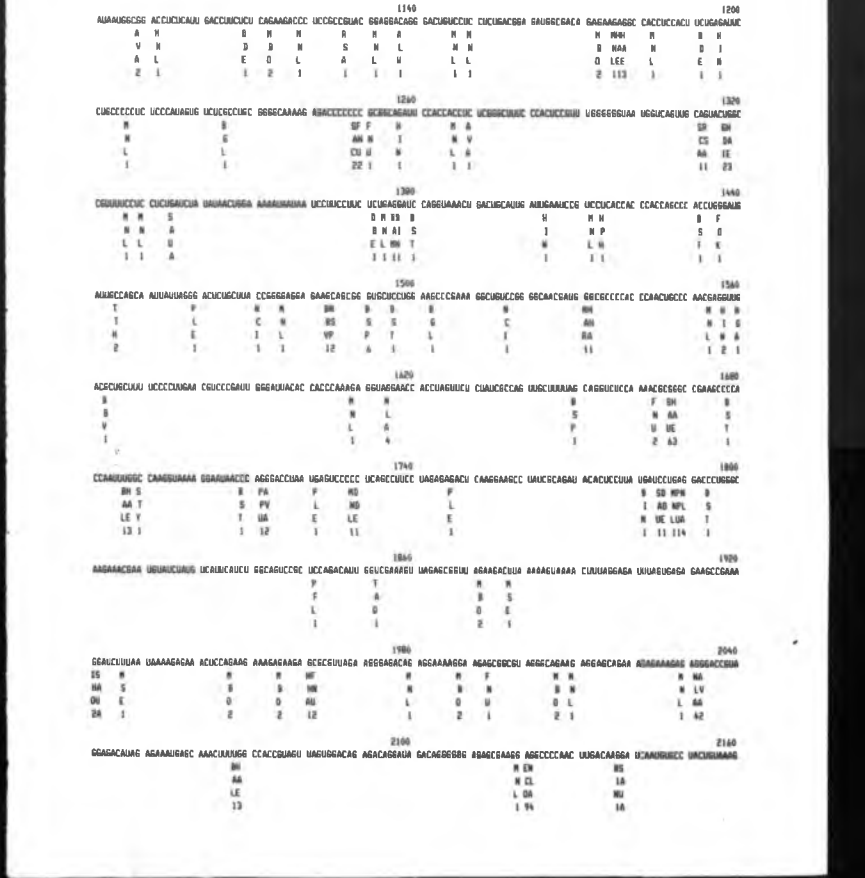

AKV murine leukemia virus, complete proviral genome

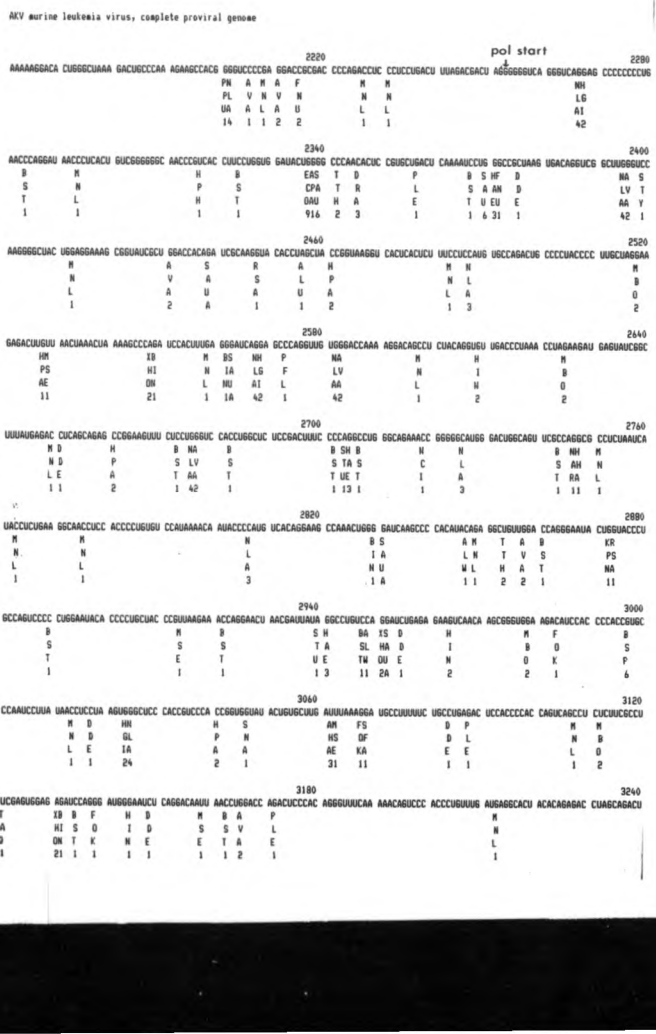

AKV murine leukemia virus, complete proviral genome

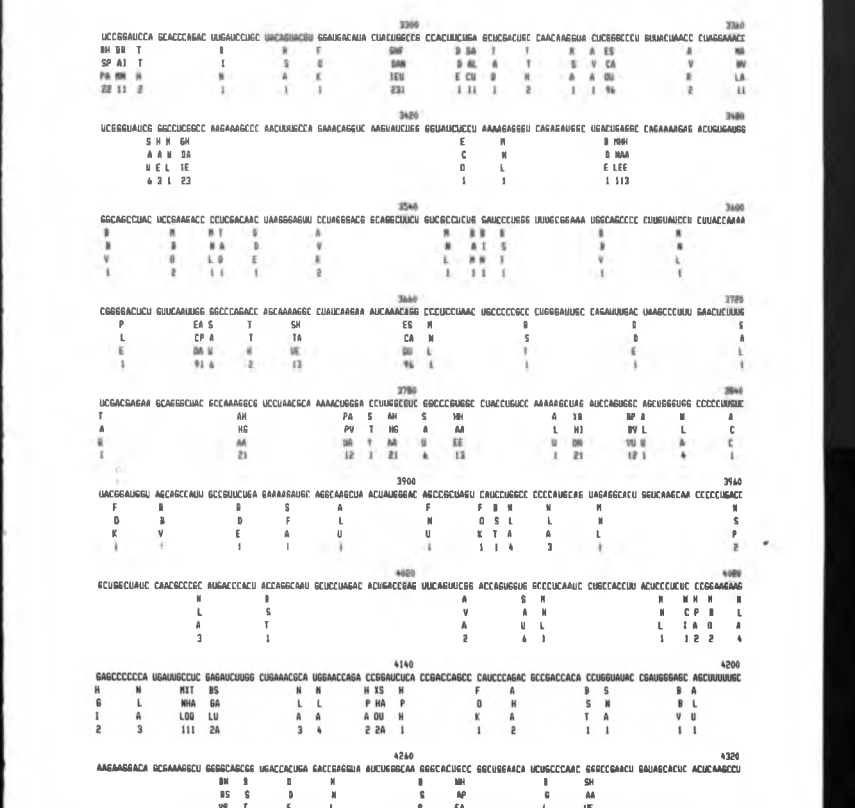

AKV murine leukemia virus, complete proviral genome

```
                                                    4380                                                    4440
UGAAGAUGGC AGAAGGUAAG AGGCUAAACG UUUACACUGA CAGCCGAUAU GCUUUCGCCA CGGCCCAUAU CCAUGGAGAG AUCUAUAGGA GGCGAGGGUU GCUAACCUCA GAGGGUAGAG
M                  M                                                  S  B    NN    BS        M   M          KD  M
B                  N                                                  A  S    CL    GA        N   N          ND  N
O                  L                                                  U  T    OA    LU        L   L          LE  L
2                  1                                                  6  1    13    2A        1   1          11  1

                                                    4500                                                    4560
AAAUCAAAAA CAAGAGCGAG AUCCUGGCUU UACUGAAAGC UCUUUUUCUG CCAAAGAGAC UCAGUAUAAU CCACUGCCUG GGGCAUCAAA AAGGAGAUAG UGCCGAGGCU AGGGGCAACC
                   IB  B          A                  P D          P   B   S                  M
                   HI  S          L                  L O          F   S   F                  N
                   ON  T          U                  E E          L   T   A                  L
                   21  1          1                  1 1          1   1   1                  1

                                                    4620                                                    4680
GCCUAGCAGA CCAAGCGGCC CGGGAGGCAG CCAUAAAGAC GCCUCCAGAU ACAUCCACUC UCCUUAUAGA GGAUUCAACC CCAUAUACGC CUGCCUAUUU CCAUUAUACU GAAACAGAUC
               F SBSN   M  B          A   M          F          E   M   H                                                  BS
               N AGHC   N  B          H   N          O          C   N   1                                                  GA
               U ULAI   L  V          A   L          K          O   L   N                                                  LU
               1 6111   1  1          2   1          1          1   1   1                                                  2A

                                                    4740                                                    4800
UAAAGAAACU CAGAGAGCUU GGGGCCACCU AUAACCAGAG CAAAGGAUAC UGGGUCUUCC AAGGCAAGCC GGUGAUGCCC GACCAAUUUG UAUUUGAACU GUUAGACUCA CUCCACCGGC
         D     A    NSH                                  M   S          H H S                                  P          H
         D     L    LAA                                  B   T          P P F                                  L          P
         E     U    AUE                                  O   Y          A H A                                  E          A
         1     1    463                                  2   1          2 1 1                                  1          2

                                                    4860                                                    4920
UCACCCACCU CGGCUACCAG AAAAUGAAAG CACUCCUUGA CAGAGGAGAA AGCCCCUACU ACAUGCUAAA CCGGGACAAA ACCCUCCAAU AUGUGGCAGA UUCCUGCACG GUCUGUCCCC
H     M                                              M                NN          N          M  P          H                B
P     N                                              N                SL          C          N  F          I                S
H     L                                              L                PA          I          L  L          N                P
1     1                                              1                13          1          1  1          1                6

                                                    4980                                                    5040
AAGUAAAUGC CAGCAAAGCU AAAAUCGGGG CAGGAGUGAG AGUACGAGGA CAUCGGCCAG GCUCCCAUUG GGAGAUCGAU UUUACAGAAG UCAAGCCAGG GCUGUAUGGG UACAAGUACC
         T   A                                      R  M      GH B  N          SCT                B          R  R  M
         T   L                                      S  N      DA S  L          ALA                S          S  S  N
         H   U                                      A  L      IE T  A          UAG                T          A  A  L
         2   1                                      1  1      23 1  4          A11                1          1  1  1

                                                    5100                                                    5160
UCCUGGUAUU CGUGGACACC UUCUCUGGUU GGGUGGAAGC CUUUCCAACC AAGAGAGAAA CAGCAAGAGU CGUGUCCAAG AAAUUGCUGG AAGAAAUAUU CCCGAGAUUC GGAAUGCCAC
B                                  X                  P                  T  M  S  A  H  B
S                                  M                  L                  T  B  S  V  I  S
T                                  N                  E                  H  O  P  A  N  M
1                                  1                  1                  2  2  1  1  1  1

                                                    5220                                                    5280
AGGUAUUGGG AUCUGAUAAC GGGCCUGCCU UCACCUCCCA GGUAAGUCAG UCGGUGGCCG AUUUACUGGG GAUCGAUUGG AAAUUACAUU GUGCUUAUAG ACCCCAGAGU UCAGGUCAGG
         IS          SH       H  M  B          GH          B SCT
         HA          AA       P  N  S          DA          I ALA
         OU          UE       H  L  T          IE          N UAG
         2A          63       1  1  1          23          1 A11

                                                    5340                                                    5400
UAGAAAGAAU GAAUAGAACC AUCAAGGAGA CUCUAACUAA AUUAACBCUU GCAGCUGGCA CUAGAGACUG GGUACUCCUA CUCCCCUUAG CUCUUUACCG AGCCCGGAAC ACUCCGGGCC
                        P          M          BPA                R          D  A          H  NH          N EN
                        L          S          BVL                S          D  L          G  CP          C CL
                        E          E          VUU                A          E  U          I  IA          I OA
                        1          1          121                1          1  1          2  12          1 94
```

AKV murine leukemia virus, complete proviral genome

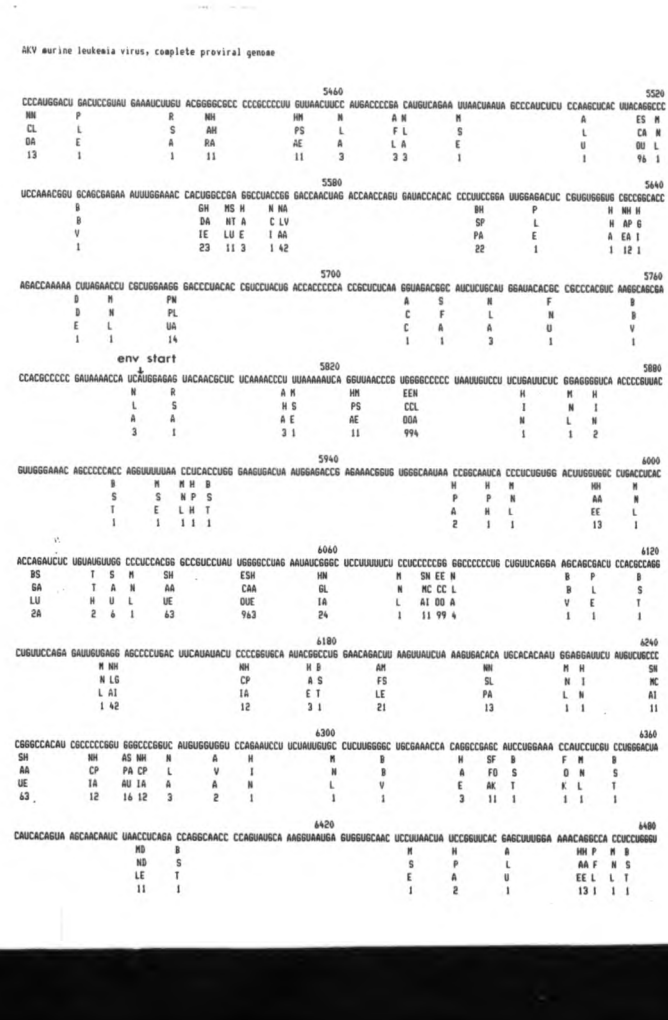

AKV murine leukemia virus, complete proviral genome

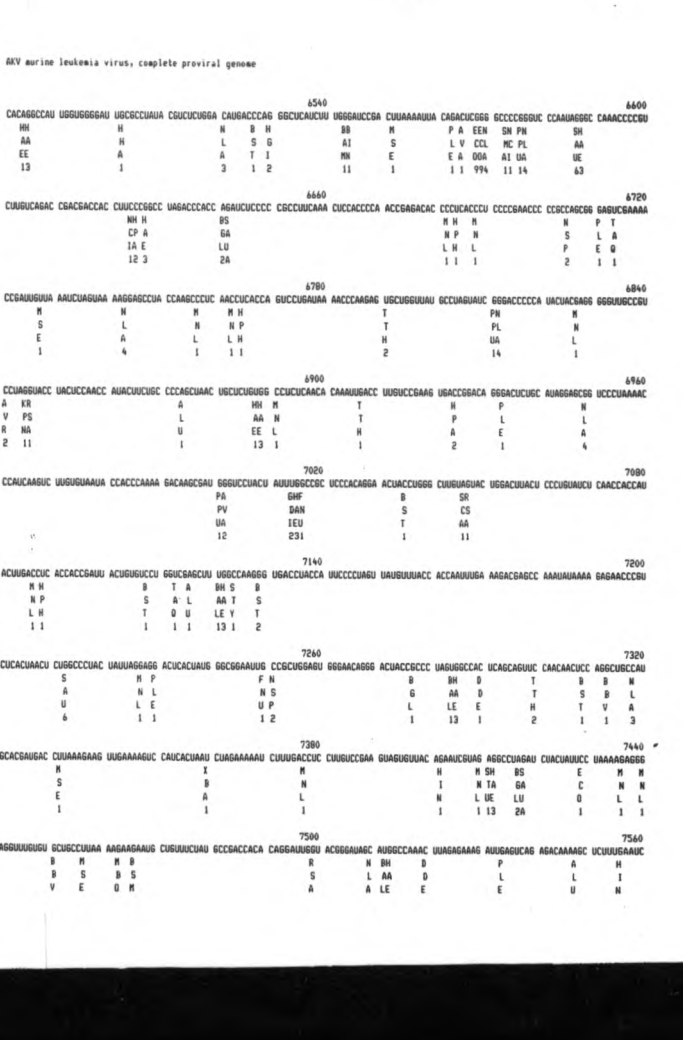

AKV murine leukemia virus, complete proviral genome

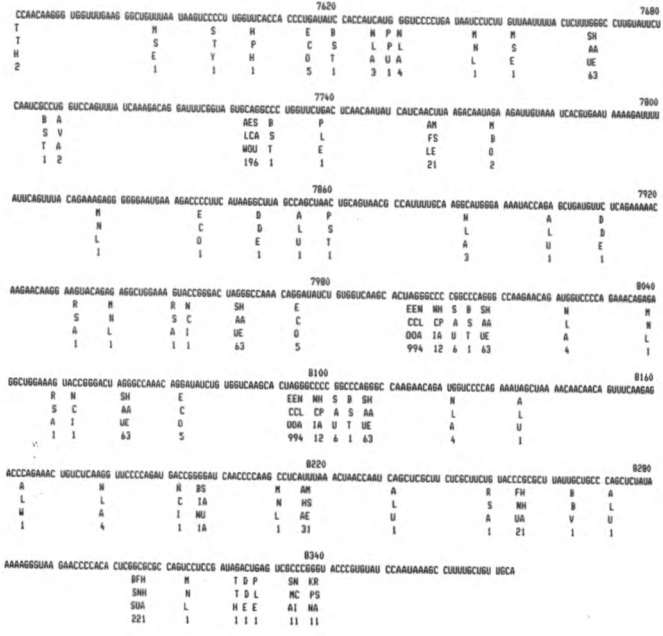

APPENDIX D.iii

Moloney murine leukemia virus (proviral), 5' LTR

```
                                                                                                                    60                                                                                                                  120
AACCUAUGAU CUCCUUUUCC UUAAUCUUGC UGUUCCCCUC CCCCAUAUGU UUACCUACUG AACAUCACUU GGGGUUGUAG AAACUAUUGG GAACUUGUCC UGGAGAAAAU UACUGAAAGA
      S            M            M       N                                                                                                  D
      A            S            N       D                                                                                                  S
      U            E            L       E                                                                                                  T
      A            1            1       1                                                                                                  1

                                                                                                                   180                                                                                                                  240
CCCCACCUGU AGGUUUGGCA AGCUAGCUUA AGUAACGCCA UUUUGCAAGG CAUGGAAAAA UACAUAACUG AGAAUAGAGA AGUUCAGAUC AAGGUCAGGA ACAGAUGGAA CAGCUGAAUA
                  AN  A AM                 M            D                S                PA
                  LN  L FS                 L            B                A                VL
                  UE  U LE                 A            E                U                UU
                  11  1 21                 3            1                A                21

                                                                                                                   300                                                                                                                  360
UGGGCCAAAC AGGAUAUCUG UGGUAAGCAG UUCCUGCCCC GGCUCAGGGC CAAGAACAGA UGGUCCCCAG AUGCGGUCCA GCCCUCAGCA GUAUCUAGAG AACCAUCAGA UGUUGCCAGG
 SH          E            A       NH   D  SN          N       S    A       MS          S                                    D  H
 AA          C            L       CP   R  AA          L       F    V       RD          G                                    S  G
 UE          O            W       1A   E  UE          A       A    A       LE          A                                    T  I
 63          5            1       12   1  63          4       1    2       11          1                                    1  1

                                                                                                                   420                                                                                                                  480
GAGCCCCAAG GACCUGAAAU GACCCUGUGC CUAUAUUGAA CUAACCAAUC AGUUCGCUUC UCGCGCCGCU CUGCUGUUUU GCGACGUUGC AGCUGCCUAC AGCCCCUCAC
D    S  PA                                                                                 FNFH            A  S A          H                M    A
S    I  PV                                                                                 NSNH            V  A L          G                N    V
P    Y  UA                                                                                 USUA            A  C U          I                L    A
6    1  12                                                                                 2221            1  1 1          2                1    1

                                                                                                                   540                                                                                                                  600
UCGGGGCGCC AGUCCUCCGA UUGACUGAGU CGCCCGGGUA CCCGUGUAUC CAAUAAACCC UCUUGCAGUU GCAUCCGACU UGUGGUCUCG CUGGUCCUUG GCAGGGUCUC CUCUGAGUGA
   MH          M       T D P    SH  KR              M            SF                      G    H    R  D
   AH          N       T D L    RC  PS              R            FQ                      T    N    N  D
   BA          L       H E E    A1  WA              L            AC                      Y    L    L  E
   f1          1       1 1 1    11  11              1            11                      1    1    1  1

                                                                                                                   660
UUGACUACCC GUCAGCGGGG GUCUUUCAUU UGGGGGCUCG UCCGGGAUCG GGAGACCCCU
           H                    R       N  35
           G                    G       C  1A
           F                    1       I  AB
           2                    2       1  1A
```

MHC D^b gene restriction map